

NUMERICAL SIMULATION OF FRACTURE OF A NANO-PAPER COATED
E-GLASS/POLYESTER COMPOSITE WITH THERMAL DAMAGE

BY

Zachary Bennett Graham

A thesis submitted in fulfillment of the requirements
for Honors in the Major
in the Department of Mechanical and Aerospace Engineering
in the College of Engineering and Computer Sciences
at the University of Central Florida
Orlando, Florida

Spring Term

2013

Thesis Chair: Ali P. Gordon

© 2013 Zachary Graham

Abstract

Aerospace research for next-generation travel increasingly focuses on the use of advanced composites to reduce weight and cost while retaining strength. One subset of materials with great potential is based on the combination of resin matrix and glass-fiber reinforcement. This research explores the application of a candidate nanopaper coating with a given composite. Prior research applied a set of given heat fluxes to the top surface of the composite for a set of given periods of time, and subsequently performed a 3-point flexural test to determine the elastic modulus for both the coated and uncoated composite for all of the combinations of heat flux and time. A finite element (FE) model is developed using the ANSYS general purpose finite element analysis (FEA) software that models the degradation in strength/stiffness properties based on heating condition and with the goal of predicting cracking using the element death feature in ANSYS. This thesis describes the prior research suggesting both the need for and novelty of this model, and the procedures used to form the model. The loading conditions of the 3-point flexural test are replicated, and four measures of accuracy are developed based on the force versus displacement curve of the test and the FE model. It is envisioned that continuum-level models developed as a part of these research be applied for design of next-generation space components. These measurements are used to verify the FE model, and this model is then employed to extrapolate beyond the context of experimental conditions.

Dedication

This thesis is dedicated to my little brother, Samuel Graham, whose unconditional love and understanding has served as an inspiration for me while conducting this research.

Acknowledgements

The materials here presented are based upon work supported by Office of Naval Research (ONR) under Grant No. N00014-09-1-0429 and Federal Aviation Administration Center of Excellence for Commercial Space Transportation (FAA COE-CST-AST) under grant number 10CCSTUCF002.

This thesis would not be possible without the prior work of Jaime Skovron and Jinfeng Zhuge, and special thanks to Thomas Bouchenot, for his technical assistance with ANSYS.

Table of Contents

List of Figures	x
List of Tables	xii
Chapter 1: Introduction	1
1.1 Motivation.....	1
1.2 Outline.....	2
Chapter 2: Literature Review	3
2.1 Bend Testing.....	3
2.2 Analytical Model	4
2.3 Numerical Simulation of Bend Fracture Composites.....	4
2.4 Prior Research	5
Chapter 3: Candidate Material and Data Review	8
3.1 Candidate Material	8
3.2 Data Review	14
Chapter 4: Numerical Modeling Approach	20
4.1 Constitutive Modeling Approach	20
4.2 Structural Model	25
4.3 Material Evolution.....	26
4.4 Simulation of Monotonic Response.....	31
4.5 Layer Model Construction.....	32
4.6 High-Order-Model Construction	33

4.7 Interpreting the Results	35
Chapter 5: Numerical Modeling Results	38
5.1 Monotonic Model Results	38
5.2 Layer Model Results	43
Chapter 6: Predictions	47
6.1 Elastic Modulus	47
6.2 Ultimate Strength	52
6.3 Glass Failure	54
Chapter 7: Conclusions and Future Work	55
7.1 Modeling	55
7.2 Verification	57
7.3 Cracking	58
7.4 Future Work	59
Appendix A: Command Sets Used	60
Appendix A.1: Monotonic Model Element Death Commands	61
Appendix A.2: Layer Model	62
Appendix A.3: Index of Commands Used (With Effects)	63
Appendix A.4: Command Logic Explanation	65
Appendix B: Full Data Set	66
Appendix B.1: Force Driven Monotonic Data	67
Appendix B.2: Force Driven Layer Data	68

Appendix B.3: Displacement Driven Monotonic Model	69
Appendix B.4: Displacement Layer Model Data	70
Appendix B.5: Uncoated Model Data	71
Appendix B.6: Coated Model Data.....	75
Appendix C: Specimens That Were Tested	79
Appendix C.1: Uncoated, $\phi=0$, $t_{exp}=0$	80
Appendix C.2: Uncoated, $\phi=25$, $t_{exp}=120$	81
Appendix C.3: Uncoated, $\phi=25$, $t_{exp}=180$	82
Appendix C.4: Uncoated, $\phi=25$, $t_{exp}=240$	83
Appendix C.5: Uncoated, $\phi=35$, $t_{exp}=60$	84
Appendix C.6: Uncoated, $\phi=35$, $t_{exp}=100$	85
Appendix C.7: Uncoated, $\phi=35$, $t_{exp}=140$	86
Appendix C.8: Uncoated, $\phi=35$, $t_{exp}=180$	87
Appendix C.9: Uncoated, $\phi=50$, $t_{exp}=40$	88
Appendix C.10: Uncoated, $\phi=50$, $t_{exp}=80$	89
Appendix C.11: Uncoated, $\phi=50$, $t_{exp}=120$	90
Appendix C.12: Uncoated, $\phi=75$, $t_{exp}=20$	91
Appendix C.13: Uncoated, $\phi=75$, $t_{exp}=50$	92
Appendix C.14: Uncoated, $\phi=75$, $t_{exp}=75$	93
Appendix C.15: Uncoated, $\phi=100$, $t_{exp}=15$	94
Appendix C.16: Uncoated, $\phi=100$, $t_{exp}=40$	95
Appendix C.17: Uncoated, $\phi=100$, $t_{exp}=70$	96

Appendix C.18: Coated, $\phi=0$, $t_{\text{exp}}=0$	97
Appendix C.19: Coated, $\phi=25$, $t_{\text{exp}}=120$	98
Appendix C.20: Coated, $\phi=25$, $t_{\text{exp}}=180$	99
Appendix C.21: Coated, $\phi=25$, $t_{\text{exp}}=240$	100
Appendix C.22: Coated, $\phi=35$, $t_{\text{exp}}=60$	101
Appendix C.23: Coated, $\phi=35$, $t_{\text{exp}}=100$	102
Appendix C.24: Coated, $\phi=35$, $t_{\text{exp}}=140$	103
Appendix C.25: Coated, $\phi=35$, $t_{\text{exp}}=180$	104
Appendix C.26: Coated, $\phi=50$, $t_{\text{exp}}=40$	105
Appendix C.27: Coated, $\phi=50$, $t_{\text{exp}}=80$	106
Appendix C.28: Coated, $\phi=50$, $t_{\text{exp}}=120$	107
Appendix C.29: Coated, $\phi=75$, $t_{\text{exp}}=20$	108
Appendix C.30: Coated, $\phi=75$, $t_{\text{exp}}=50$	109
Appendix C.31: Coated, $\phi=75$, $t_{\text{exp}}=75$	110
Appendix C.32: Coated, $\phi=100$, $t_{\text{exp}}=15$	111
Appendix C.33: Coated, $\phi=100$, $t_{\text{exp}}=40$	112
Appendix C.34: Coated, $\phi=100$, $t_{\text{exp}}=70$	113
References	114

List of Figures

Figure 1 Diagram of Physical Experiment [Skovron et al., 2012]	3
Figure 2: (a) Sketch (b)Scanning Electron Microscope Widthwise Image of Undamaged Coated Composite.	10
Figure 3: (a) Sketch (b)Optical Microscope Top-Down Lengthwise Image of Uncoated Composite.....	11
Figure 4: Optical Microscope Top-down Lengthwise Image of Nanopaper Coated Composite (Length scale overwritten for clarity).....	12
Figure 5: Weave Modeling Function [Shahkarami and Vaziri, 2007].....	13
Figure 6: (a) Calorimetry Machine used for fire testing (b) Calorimetry Process Used for Heat Damage [Skovron, 2013]	15
Figure 7: Three-Point Bend Response of Unheated Coated and Uncoated Composite	17
Figure 8: Three-Point Bend Response of Coated and Uncoated Composite under 25 Kilowatts of Heat Flux for 240 seconds.	18
Figure 9: Illustration of Pop-In Behavior based on Model Representation of Bend Testing.	19
Figure 10: Stress/Strain Chart of the Response of a Single Element to Element Death.....	21
Figure 11: Verification Diagram	22
Figure 12: Sketch of Model Side Views for Reference.....	25
Figure 13: Uncoated Model Fit	27
Figure 14: Exposure Time and Flux Dependency of Modulus.....	28
Figure 15: Coated Model Fit	29
Figure 16: Quarter Model, Reduced boundary conditions	32
Figure 17: Layer Model Mesh	32
Figure 18: External View of High Order Model	34

Figure 19: Internal view of High-Order Model.....	35
Figure 20: Resulting Displacement in Quarter-Model of 3 Point Bending Simulation	38
Figure 21: Monotonic Model, Force Driven Methods	39
Figure 22: Monotonic Model Methods Comparison	40
Figure 23: Unheated, Uncoated Model with a deflection of 6.8 millimeters	41
Figure 24: Unheated, Uncoated Model with a deflection of 7.2 millimeters	42
Figure 25: Unheated, Uncoated Model with a deflection of 7.6 millimeters	42
Figure 26: Layer Model Methods Comparison, Control-A experimental data	43
Figure 27: Cracked Elements.....	46
Figure 28: Uncoated and Unheated Layer Model Results	48
Figure 29: Uncoated $\phi = 25kwm^2, texp = 180 sec$ Model Results	49
Figure 30: Uncoated $\phi = 50kwm^2, texp = 40 sec$ Model Results	49
Figure 31: Uncoated $\phi = 100kwm^2, texp = 40 sec$ Model Results	50
Figure 32: Coated and Unheated Model Results	50
Figure 33: Coated $\phi = 25kwm^2, texp = 180 sec$ Model Results	51
Figure 34: Coated $\phi = 50kwm^2, texp = 40 sec$ Model Results	51
Figure 35: Coated $\phi = 100kwm^2, texp = 40 sec$ Model Results	52

List of Tables

Table 1: Glass-Mat Weave Modeling Constants	14
Table 2: Mean Value of Error for Heating Conditions Selected for Crack Testing	44
Table 3: R^2 value for Heating Conditions Selected for Testing	44
Table 4: Percent Difference in Riemann Sums for Points Selected for Testing	45
Table 5: Model Ultimate Strength Table.....	53
Table 6: Equation 6 Ultimate Strength Table.....	53
Table 7: Uncoated Composite Layer Model Material Properties Summary	56
Table 8: Coated Composite Layer Model Material Properties Summary	57

Chapter 1: Introduction

1.1 Motivation

In developing new materials for structural applications, one of the most important thresholds is characterizing material performance under conditions that go off the map of experiments. For example, a finite element model can predict the results of a wide variety of mechanical experiments. Results can then indicate which tests might emphasize a certain deformation mode to gain a better understanding of the material, and can give insight to the data acquired through experimental testing. Finite element models are also useful for understanding the stress distribution within composites and the resultant strain at critical locations within the composite. Polyester and E-glass composites have a history of being used in many industries. The aerospace industry uses similar composites as the largest component (by weight) in its most modern airplanes [Hale, 2006]. These composites are used in aerospace applications to create lightweight vehicles that can be rapidly reused (differentiating them from the space shuttle and prior space vehicles which require major repairs between uses) because of their high specific strength, and ability to withstand both high tensile loads and high impact loads.

Polyester resin reduces in strength when exposed to temperatures above 75°C, with pyrolysis occurring between 250°C and 400°C. Re-usable launch vehicles (RLVs) have encountered temperatures above 1500°C upon re-entry to the atmosphere of the earth, therefore to permit the use of glass-reinforced polyester composites in this context, the temperature experienced by the structural composites of RLVs must be reduced. One method to reduce the temperature of the polyester resin is to apply a coating to one or both sides of the composite. A coating acts as a thermal barrier, reducing the rate of heat transfer and protecting the subjacent material. This thesis focuses on simulating the macroscopic deformation behavior of a woven nanopaper coating applied to a polyester and E-glass composite.

1.2 Outline

The remainder of this thesis will be dedicated to the analysis and development of numerical methods used in creating finite element models for composites. In Chapter 2, prior methods of numerical analysis used with creating finite element models of composites will be enumerated and analyzed for parallel applications in this model. The prior methods analyzed are divided into the current state-of-the-art and the historical methods applied in analysis. Chapter 3 is devoted to an explanation of the composite being researched, and an explanation of the data obtained from.[Zhuge et al., 2012; Skovron et al., 2013] Chapter 4 is devoted to describing the methods used to formulate the finite element model, the assumptions made in its creation, and the theory and methods used in relating the results obtained to the experimental data. Chapter 5 explores the results obtained from each model. Chapter 6 takes the results from the finite element model and formulates predictions relating the elastic moduli of the resin and the glass fibers, the ultimate strength of the resin, and the ultimate strength of the adhesion to the proportion of weakening due to heat damage, the ultimate strain, and the total ratio of the unheated, uncoated elastic modulus to the elastic modulus of the finite element model. Chapter 7 draws conclusions using the finite element model and the predictions formed, and elaborates some of the possibilities for future research.

Chapter 2: Literature Review

2.1 Bend Testing

Three-point bend testing is one of two standard methods used for testing the flexural properties of a material. The other method is four-point bend testing, which supports the material at the same locations, but applies loads at 25% and 75% of the span. Figure 1 describes the conditions used in three-point bending.

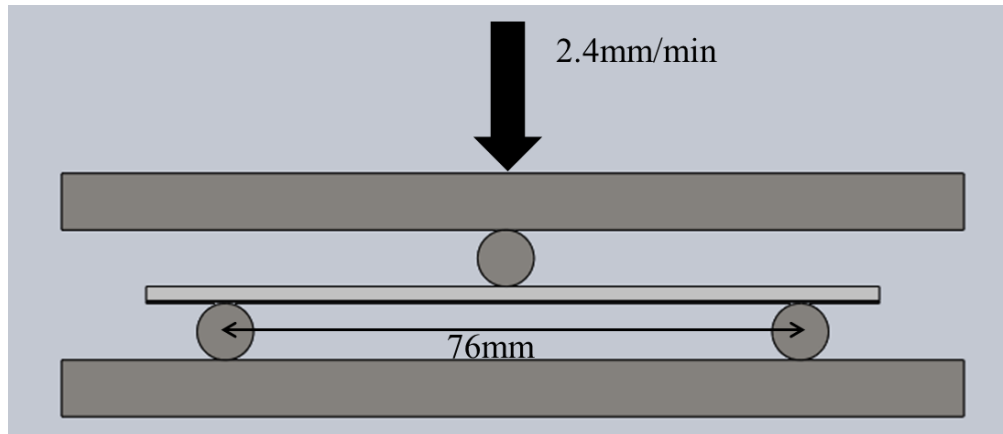


Figure 1 Diagram of Physical Experiment [Skovron et al., 2012]

The data generated from this test are force versus deflection curves. From this curve, several quantities can be found, including the tensile strain energy, flexural elastic modulus, and a theoretical value of the ultimate stress, and an understanding of the plastic behavior of the material. The most important of these properties is the elastic modulus. All other material properties are generally related in a simple fashion to the elastic modulus, typically in a linear fashion. The equation used to obtain the elastic modulus from these tests is as follows:

$$E = \frac{L^3 m}{4bd^3} \quad (1)$$

Typically, some of these parameters are standardized to minimize variability resulting from deviations. The parameter L is the span, standardized at 76 mm for plastics [ASTM, 2010], the width b is not standardized but is measured in millimeters, as is the thickness d . The variable m is the initial slope of the force versus displacement curve in newtons per millimeter.

2.2 Analytical Model

An important part of finite element modeling is comparison and verification. The primary way this is done in theory is by the use of analytical treatments to make predictions based on the properties of the material. The analytical treatment used is as follows, the basic formula for a simply supported beam, loaded in the middle:

$$w(x) = -Px \frac{4x^2 - 3L^2}{48EI} \text{ for } 0 \leq x \leq \frac{L}{2} \quad (2)$$

$$w(x) = P \frac{(x-L)(L^2 - 8Lx + 4x^2)}{48EI} \text{ for } \frac{L}{2} \leq x \leq L$$

The force P , elastic modulus E , moment of inertia I , length L and deflection w at a given location x are related by this equation. The experimental data provides all three quantities and given two of the three quantities a finite element model should be able to return the value of the third within a reasonable error. Other woven composites deviate from simple elastic behavior in both shear and tension [Cavallaro et al., 2007]. The error on the results from the finite element analysis and any patterns in error on this result will indicate how this material deviates from simple models of behavior.

2.3 Numerical Simulation of Bend Fracture Composites

For the purpose of understanding the behavior of composites, analytical treatments have proven to be inadequate, or too complicated to apply reliably and quickly. Finite element methods have a long history of use with woven composites [Tarfaoui et al., 2001], and recent developments have provided new possibilities to make the modeling process easier and more accurate. The most important

of these developments for this application is the development in ANSYS of the Element Death feature [Liu et al., 2010]. Element death involves setting a criterion for setting the elastic modulus of an element to a very small value, effectively removing it from calculations. The default value is 1×10^{-6} . This tool is useful for models where local failure can change the stress distribution drastically, such as in a woven composite [Masmoudi, 2008]. Previous studies have used discrete two or three layer models to replicate the thermal damage. Several issues present themselves with this approach. The primary issue becomes the classification of the varying layers. Classifying the layers and their rate of progression becomes difficult from a modeling standpoint and a practical standpoint. Second, these models tend to have difficulty capturing small changes or differences because they typically assign a static value to the material properties of the layer across the entire span and depth of the layer. The data that these models are based on are also to a certain extent suspect, because glass-fiber polyester composites recover a portion of their strength after cooling down, and their behavior post-fire may not represent their behavior during the fire. [Kandare et al., 2010]

2.4 Prior Research

The research notes of Jinfeng Zhuge indicate that the primary limitation of glass-reinforced polyester composites is their poor resistance to fire damage. Various thermal barriers have been sought to address this weakness. A thermal barrier can either reflect the heat flux away from the composite, or can slow the rate at which heat disperses through the composite. The nanopaper coating used in this thesis is the latter. Prior research indicates that the nanopaper coating is effective in this capacity. In this thesis, correlations will be formulated to permit the explicit expression of the effect of the coating based on past and present models formulated with regards to the thermal damage suffered by the composite for a given value of heat flux and exposure time. Skovron created a model to relate the effect of varying

levels of heat flux and exposure time (in the form of total energy exposure) to the effect on the monotonic elastic modulus:

$$\frac{E}{E_0} = e^{-.294H} \quad (3)$$

$$\frac{E}{E_0} = e^{-.376H}$$

In this model, H is the energy that the composite is exposed to in kilojoules. The modulus is E_0 at zero energy exposure, and E is the modulus at the current level of exposure. The moduli at current and zero exposure, E_0 and E , must use the same units. These models have a correlation of 75.8% and 86.4% [Skovron et al., 2012] for the coated and uncoated experimental data respectively. This model possesses the potential for improvement, but functions as a reasonable approximation for finite element modeling and understanding the trends introduced by heat flux and exposure time.

For conditions outside of the experimental data, (2) allows the approximation of the values of elastic moduli for use with the finite element model formulated. This is especially important because thermal damage in glass-reinforced plastics is nonlinear [Kollegal and Sridharan, 2000], so a linear interpolation or extrapolation from the discrete points tested is insufficiently accurate for engineering purposes. For the purposes of modeling, it can be assumed that all of the thermal damage occurs to the resin [Looyeh et al., 1996]. If the resin becomes entirely unable to bear load, the stiffness and other mechanical properties of the composite are minimal.

The most recent research, by Skovron, indicates, that four unloading methods are possible: Deforming the full 12mm of the ATSM standard for 3-point bend testing [ATSM, 2010], force dropping gradually to 50% of the maximum, the force can unload too quickly (asymptotically or nearly asymptotically), or the force value can decrease and hold at a constant value. The use of discrete layers

may not be able to capture the transitions between these behaviors. It will also be instructive to evaluate the ability of the model to capture these forms of unloading, once the model is formulated.

Chapter 3: Candidate Material and Data Review

3.1 Candidate Material

The E-glass fiber was woven with a plain weave pattern into mats. The individual fibers used are shown in Figure 1. Bundles of these fibers were woven to form the mats, and were elliptical in shape. The mats had a density of approximately 800g/m^2 and an average thickness of 0.85mm . These mats were obtained from Composites One, Incorporated. Four of these mats were interspersed approximately evenly into the resin for an overall fiber volume fraction of 30% [Tang et al., 2011]. The edges of the E-glass mats are exposed in the samples used because the sections used were cut from larger circular panels. The properties of the composite can be assumed to be independent of the number of layers of glass fiber, and is instead dependent only on the orientation and volume fraction of the glass fiber. [Page et al., 2004; Takeda et al., 2002].

The resin matrix used was a pre-promoted, thixotropic, orthophalic, unsaturated polyester resin hardened with methyl ethyl ketone peroxide. The weight ratio of resin to hardener was 100:1. The resin had a density of 1.1 g/cm^3 , at a heat deflection temperature of 75°C , product code GP100P, supplied by PolyGard. [Ferreira et al., 2006] The nanopaper coating used was manufactured by Zhuge, with details of its manufacturing process available [Zhuge et al., 2012].

The images from a scanning electron microscope and an optical microscope describe the mesoscale geometry more fully, as shown in Figures 2 through 4. In Figure 2, the size of these individual fibers can be seen to be approximately $8.7\mu\text{m}$ in diameter. Each bundle of these fibers is approximately $3000\mu\text{m}$ wide, and $250\mu\text{m}$ tall, for approximately 6308 fibers per bundle (approximating the cross-sectional area as a set of four triangles). As previously stated, the geometry is important to an accurate modeling and understanding of the composite. Figures 2 and 3 show a broad picture of the interwoven layers of composite. Figure 4 illustrates the geometry of the nanopaper coating on the coated

composites and its similarity to the geometry of the glass-fiber mat in Figure 3. Figures 2 and 3 show that the lengthwise cross-section of the glass-fiber reinforcement of the composite is a very flat elliptical and the widthwise cross-section is a broad rectangle whose centerline follows a sinusoidal function that can be seen in Figure 5.

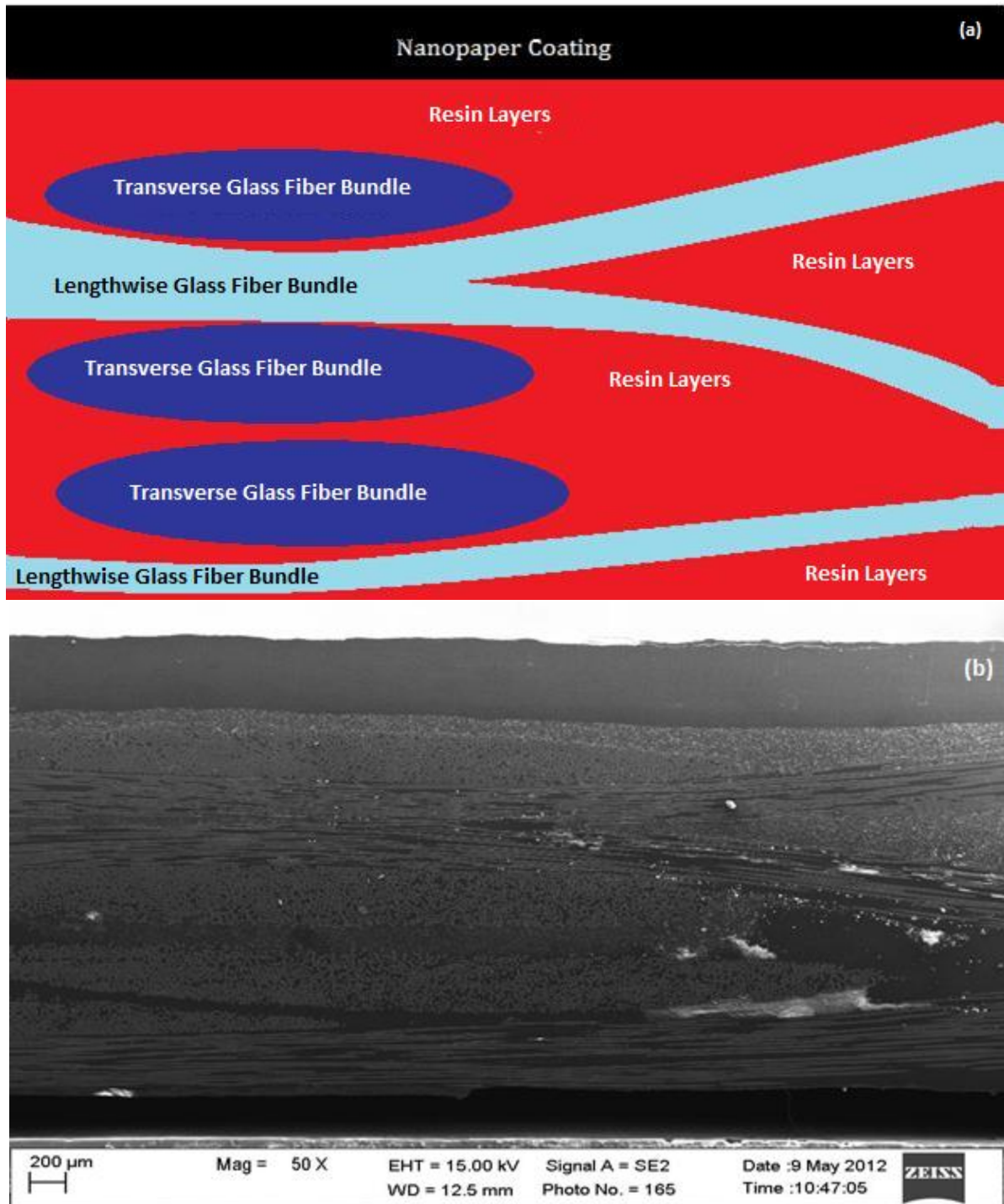


Figure 2: (a) Sketch (b) Scanning Electron Microscope Widthwise Image of Undamaged Coated Composite.

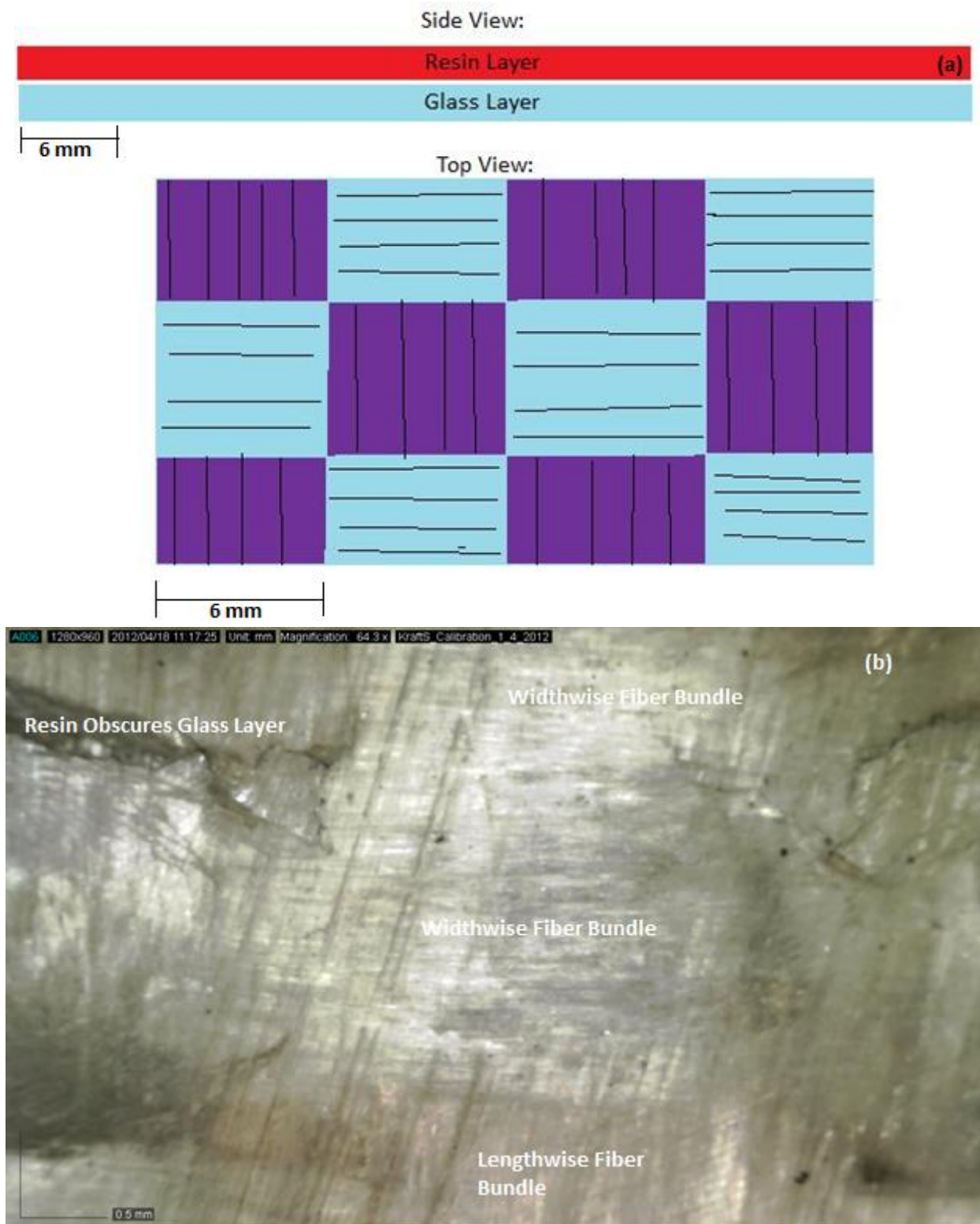


Figure 3: (a) Sketch (b)Optical Microscope Top-Down Lengthwise Image of Uncoated Composite

Figure 4 is the same as figure 3, except that this is an image of the weave of the nanopaper coating applied to the top side of the composite. This sample is nearly identical to the sample shown in Figure 2. The lengthwise and widthwise paper fibers are visible in the photograph below. The film in the upper-right corner of the image is the result of lighting issues rather than an actual change in the composite.

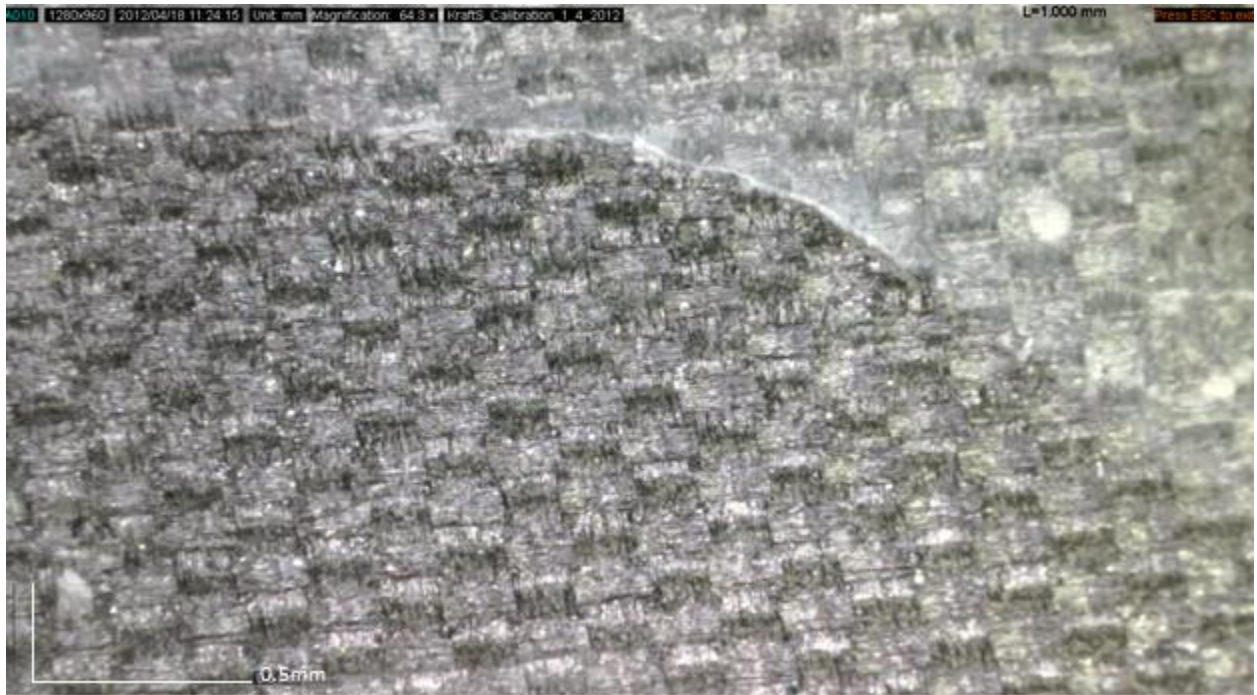


Figure 4: Optical Microscope Top-down Lengthwise Image of Nanopaper Coated Composite (Length scale overwritten for clarity)

The sinusoidal structure of the composite can be seen explained in Figure 5. The composite, as seen in Figure 1, is of the first type of cross-section because the ends taper off sharply, rather than being round. The quantity w_1-g_1 represents the width of the cross section.

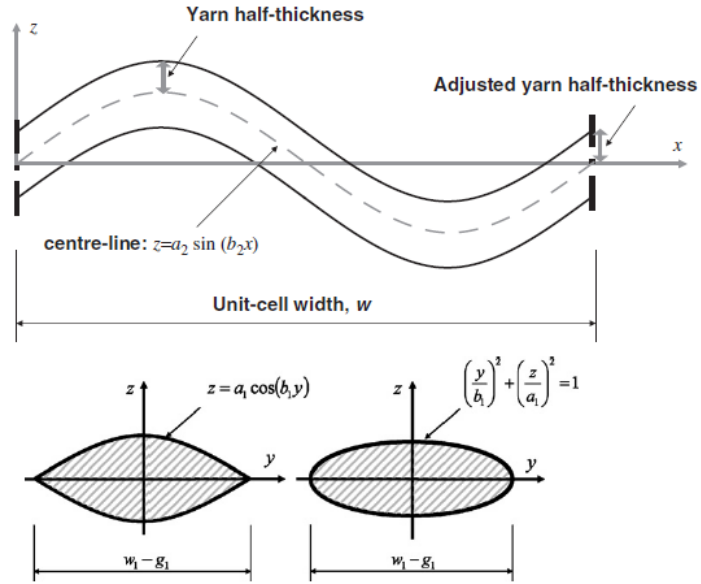


Figure 5: Weave Modeling Function [Shahkarami and Vaziri, 2007]

Based on Figures 2-5, the geometry can be replicated in the ANSYS environment. The constants obtained from the figures are listed in Table 1. The weave for the glass-fiber mat is assumed to be identical for the lengthwise and transverse fibers. This is a common assumption for composites, and sufficient for engineering purposes [Guan and Gibson, 1997]. The nanopaper coating is assumed to be weak mechanically, and does not contribute to the mechanical properties of the composite. Because the finite element analysis being performed is a mechanical analysis, the effect of the coating on the composite can be incorporated mathematically, and does not need to be modeled.

Table 1: Glass-Mat Weave Modeling Constants

Quantity	Value
$a_1 (\mu\text{m})$	210
$a_2 (\mu\text{m})$	330
$b_1 (\text{nm}^{-1})$	1.047
$b_2 (\text{nm}^{-1})$	0.7306

The material properties of the constituents must be considered in producing the model. The material properties of the resin varies depending on the processing, but has a generally accepted flexural modulus of 4 GPa and a flexural failure stress of 78 MPa [Davallo et al., 2010]. The glass fiber has an accepted flexural modulus of approximately 80 GPa [Masmoudi, 2008]. This difference in the elastic modulus is essential to how the composite bears load. The resin transfers the force to the glass fiber, increasing the ultimate strength of the composite. The woven nature of the glass fiber mats used in the construction of the composite increases the ultimate strength and failure stress of the fiber mats largely by changing the reinforcement from uniaxial to planar. The resin prevents environmental factors (such as wear, stress concentrations, corrosion, and heat) from directly impacting the glass fibers, and increases its flexibility from pure glass fiber.

3.2 Data Review

In prior research, half of these panels were given a nanopaper coating on the top side, or the side exposed to the majority of the heat flux, and half were left uncoated. The heating was performed using a calorimeter as shown in Figure 6.

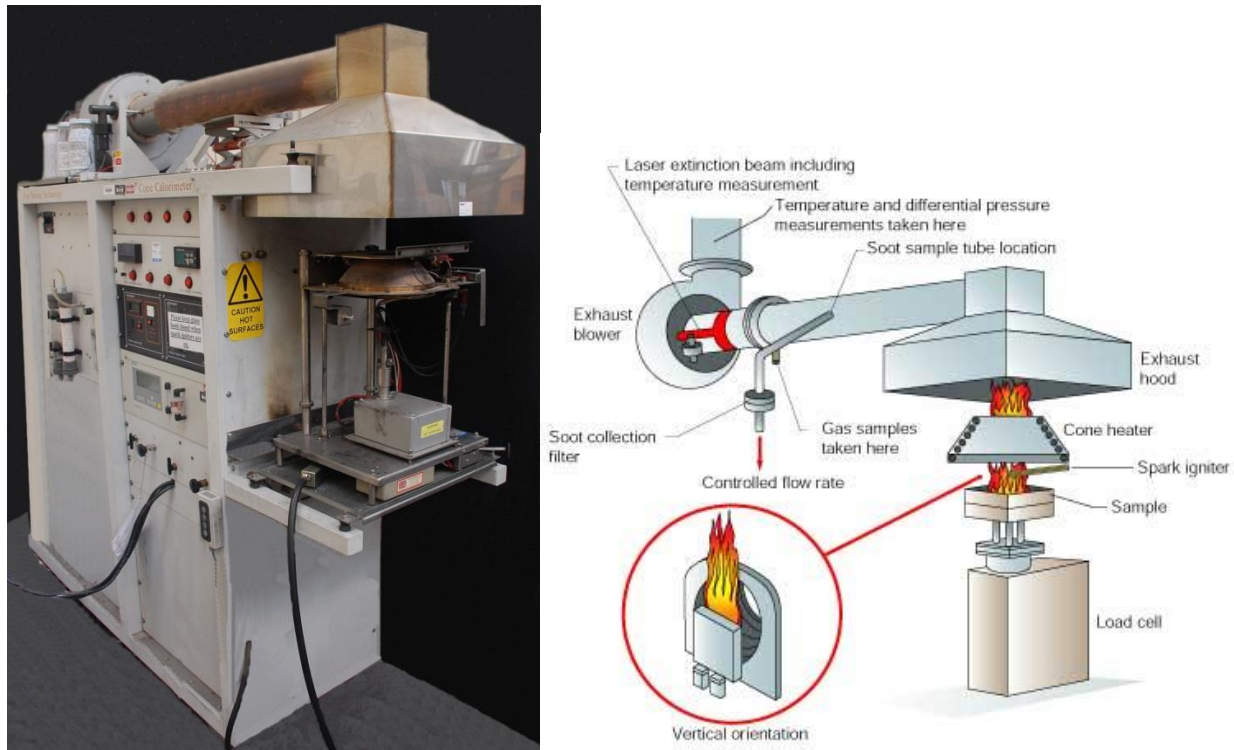


Figure 6: (a) Calorimetry Machine used for fire testing (b) Calorimetry Process Used for Heat Damage [Skovron, 2013]

The resulting damaged samples were put under a 3-point bend test to obtain their flexural modulus. The flexure tests were administered according to ASTM standard D790-10. A representative set of undamaged samples were also tested with and without the nanopaper coating. Flexural testing for composites replicates the service conditions of full-scale components. This prior research is the basis for this model, which aims to replicate the thermal damage behavior of the composite with and without the coating, as well as use the predicted stress distribution within the composite to predict the location, direction, and size of cracks that will lead to failure. Despite advances in technology decreasing the cost of producing components with smaller tolerances, glass-reinforced polyester composites remain extremely anisotropic and heterogeneous in nature. The difficulty in adjusting the geometry of a finite element model to match the measurements of each composite tested would be prohibitive. The elastic

modulus and other parameters must be changed, instead, while holding the geometry of the model constant.

Because the glass reinforcement has a Young's modulus several times larger than the modulus of the resin, the stress distribution within the resin will vary enough to cause pop-in failure. Pop-in failure occurs when a crack penetrates a layer of material and encounters another layer of material which requires additional energy to crack. The difference between the elastic modulus of the resin and fiber, and the occurrence of pop-in failure lends further credence to the idea that the mesoscale geometry and the stress distribution within the weave of the mats within the composite is crucial to analyzing flexural failures in these composites. Figures 7 and 8 help to illustrate the causes of pop-in failure, and demonstrate what predictions can be made about its occurrence and behavior.

The data describes the behavior reasonably well, as can be seen in Figures 7 and 8 [Skovron et al., 2012]. Figure 7 shows how the composite behaves under no thermal load. Pop-in failure occurs in the uncoated composite, and Figure 7 shows that pop-in failure occurs to a much lesser extent in the coated composite. The coating decreases the effective elastic modulus of the composite, and is placed on the top of the composite, implying that the pop-in failure occurred at the top of the composite. Given this, Figure 8 indicates that pop-in behavior is greatly lessened in the coated or uncoated composites with thermal damage. Equation 4 supports the theory that pop-in failure begins at the top layer of the resin by stating that the state of maximum compressive stress occurs at the top of the composite if the force P is applied in the negative Z direction. Equation 4 describes the stress distribution in the resin over the range of distances, y , from the neutral axis.

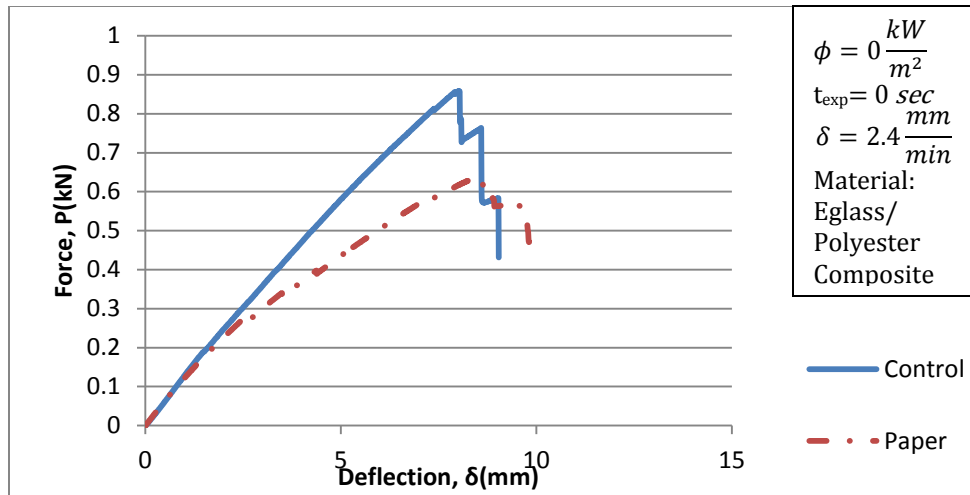


Figure 7: Three-Point Bend Response of Unheated Coated and Uncoated Composite

Figures 7 and 8 are not plotted on the same vertical axes because the illustrations of figure 8 appear as simple straight lines that appear to be approximately equal to zero if plotted on the same scale. This obscures the point being made by Figure 8: that the heated data displays less pop-in behavior (fewer and smaller drops in force as a percentage of the maximum force) than the unheated data. The control specimens in each case are the same thickness as the paper specimens, and this is the cause of the lesser values of force for the paper-coated samples.

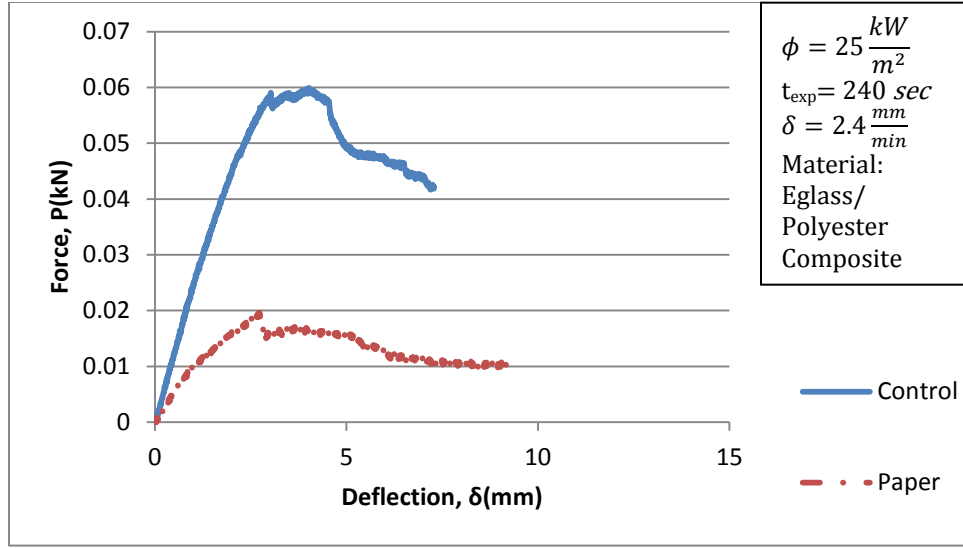


Figure 8: Three-Point Bend Response of Coated and Uncoated Composite under 25 Kilowatts of Heat Flux for 240 seconds.

Equation 4 relates the stress σ in megapascals at the centerline of the composite where the stress is maximized to the applied force P in newtons and the vertical distance from the neutral axis y in meters for the resin sections in the uncoated composite. The equation is valid only inside the resin layers, which are indicated by the values of y given in Equation 4.

$$\sigma = 59.2Py \text{ for } \begin{cases} 1.56 \times 10^{-4} > |y| > 0 \\ 1.03 \times 10^{-3} > |y| > 7.16 \times 10^{-4} \\ 1.9 \times 10^{-3} > |y| > 1.59 \times 10^{-3} \end{cases} \quad (4)$$

The only prediction that can be made is that as the damage increases, the stress should decrease on the upper portion of the composite (as it becomes less able to bear load) and should increase on the lower portion of the composite (as its ability to bear load increases). This idea can be validated by looking at Figure 2. The bend in the widthwise cross-section creates a stress-concentration that supports the belief that a pop-in failure of the layers occurs, causing a re-strengthening after the initial failure. Being a microstructural effect, an accurate modeling of the microstructure should replicate the behavior exactly, as long as the elastic modulus, E , is captured.

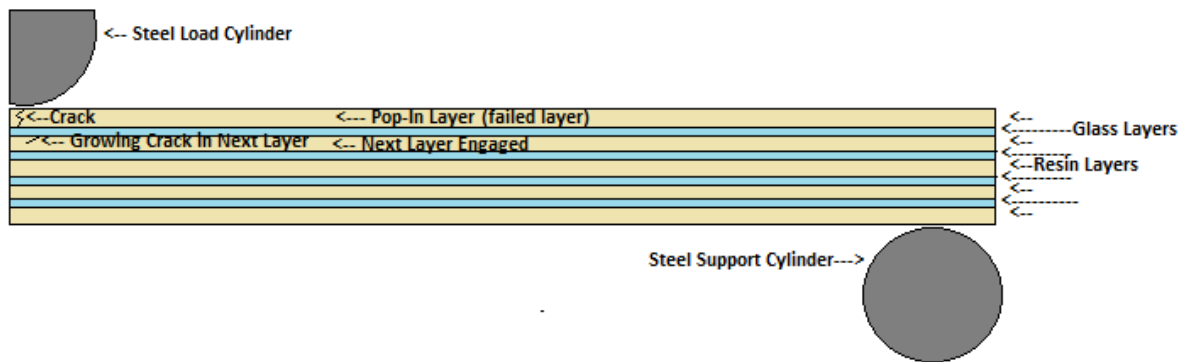


Figure 9: Illustration of Pop-In Behavior based on Model Representation of Bend Testing.

Chapter 4: Numerical Modeling Approach

4.1 Constitutive Modeling Approach

Before formulating a finite element model, it is important to understand what results are desired, and what forms of error can be calculated for the model. Cracking is the primary area this study seeks to explore. Some numerical simulations of cracking requires a prior knowledge of the location of a pre-existing crack and the direction of crack propagation. Crack growth modeling requires a large amount of knowledge about the material and involves a large number of calculations. The issue becomes how to find a pre-existing crack, and how to intuit the direction of the crack growth. Under a certain set of assumptions, element death allows this to occur. Element death imitates the behavior of cracking by reducing or eliminating the ability of an element to carry load. The sequence in which elements are killed indicates the probable location for initiation of a crack, direction of the growth of the crack, and length of the crack. Figure 10 explains element death behavior. After failure, all of the stress values and the strain values of that single, individual element are permanently set to exactly, identically zero. Element death can only be set to kill all selected elements, meaning the ability to assign a critical criteria to cause element death is limited only by the ability to select the appropriate elements. Notably, this means that directional stress, directional strain, equivalent stress, equivalent strain, and even predefined failure models can be used as element death criteria, and that failure can be limited to a single material, or that different criteria can be assigned to different materials.

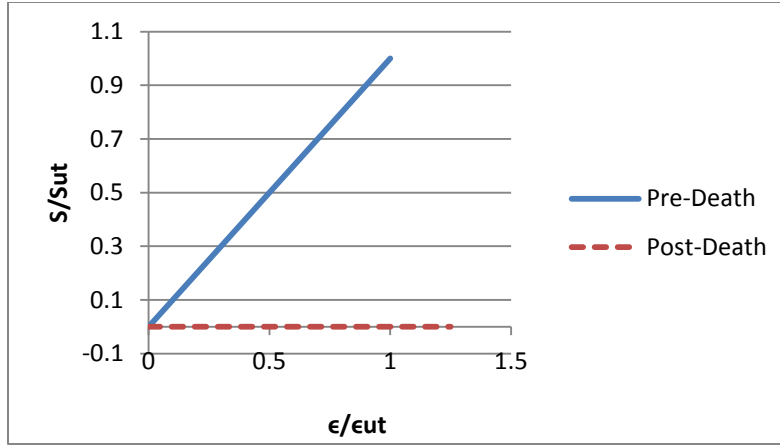


Figure 10: Stress/Strain Chart of the Response of a Single Element to Element Death

With all of the experimental data discussed in Chapter 3 (summarized in Appendix D), the challenge becomes developing methods of verification for the model. It will only be valid and of use if it can demonstrate that it accurately reflects the physical situation. For this purpose, four measurements suggest themselves: (1) matching the elastic response, (2) matching the elastic-plastic behavior, (3) matching (2) and the pop-in response, and (4) matching the area under the force versus displacement curve.

Initial focus on these constitutive models were geared to experiments on the unheated and uncoated composite. The properties of the heated coated and uncoated composites were related to the properties of the unheated and uncoated case, so effort was placed in ensuring that the fit for this case was as accurate as possible. Figure 11 shows an actual set of experimental data (Control-A) and the theoretical response of the model. The data was obtained at a constant rate of $\delta = 2.4 \frac{mm}{min}$. If a force is applied, the model should be able to return the corresponding displacement. If a displacement is applied, the model should be able to return the corresponding force.

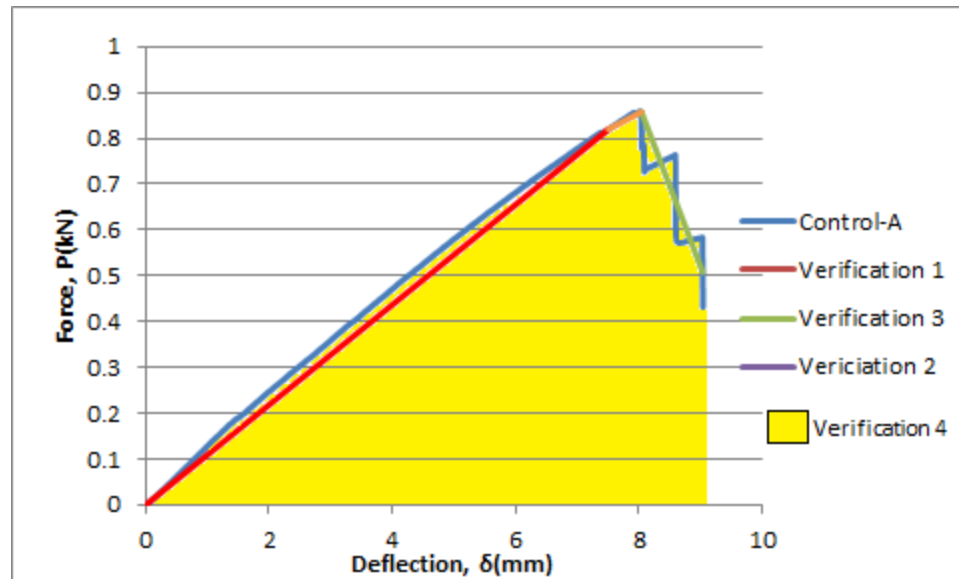


Figure 11: Verification Diagram

The first modeling step is matching the elastic behavior as indicated by the slope of the initial line on the force versus deflection curve. Finite element models tend to under-predict the elastic modulus of composites [Xu et al., 2005]. This form of verification is the most important for most applications and everyday use of the composite, because the design will need to be kept in the elastic range to avert fatigue failure under bending. For that reason, this is the most important form of verification and is the minimal verification that must be achieved for the model to be considered functional.

The second form of verification is matching the behavior of the curve in the (relatively brief) plastic region. Matching the behavior in this region proves that the basic engineering stress versus strain behavior of the composite is being modeled correctly, and provides some indication that the stress distribution can be trusted for design purposes. Most likely this can be accomplished within the uniform model by a bilinear strain hardening model of the elastic modulus, using one value for the non-elastic

section, and a second value for the plastic section of Figure 11. Equation 5 details the behavior of this model.

$$\epsilon = \begin{cases} \frac{\sigma}{E} & \text{if } \sigma \leq S_y \\ \frac{\sigma - S_y}{E_T} + \frac{S_y}{E} & \text{if } \sigma \geq S_y \end{cases} \quad (5)$$

The parameters of equation 5 involve material properties and the stress/strain response of the material. The strain ϵ is related to the stress σ , the elastic modulus E , the tangent modulus E_T , and the yield stress S_y . For all applications in this thesis, the value of the tangent modulus E_T is 1.0×10^{-6} Pa. A large issue with the use of this behavior is the nonlinear and iterative solution it requires. The algorithm must check the calculated stress against the yield stress, and every time an element yields, new calculations must be performed to ensure surrounding elements have not yielded as well. This form of verification is the least important form of verification, due to the brevity of the plastic section. This form of verification will not be actively sought, but will be looked for in each analysis.

The third form of verification is matching the average behavior, or matching an approximate best fit line through the pop-in portion of the load-deflection curve denoted as the region of data after the initial sharp decrease in force carried. Matching this behavior implies that the model captures the unique qualities of this material, and can be relied on as essentially a highly accurate replica of the material. This model will likely be unable to be replicated with the uniform model; however, an accurate model of the mesoscale geometry utilizing element death to remove cracked elements replicates this effect faithfully as long as the ultimate stress of the resin is replicated accurately. According to the theoretical analysis in Equation 4, this maximum stress should be 96 MPa. In the finite element analysis, any resin element that meets or exceeds this stress will be considered to have failed, and will be reduced to a stiffness of 0 using Element Death.

The final form of verification is matching the area under the curve. The area under the curve is defined as the tensile strain energy of the material, which is a critical quantity for most failure models. Area under the force versus deflection curve is a good overall measure of fit, across all applications and concerns. If this quantity matches well, then it is an indicator which failure model this material will match, and indicates the applicability of the model to the material in these purposes. In theory, if the previous three forms of verification are achieved, then this form of verification should be achieved within acceptable limits. The critical form of verification for this purpose will be Verification 3 from Figure 11 because pop-in is the form of behavior of interest and the most difficult behavior to replicate for this composite.

This same verification can be applied to all of the composites with varying levels of energy exposure and damage. The modeling of the effects of the damage caused by the energy exposure will depend on the capabilities and accuracy of the thermal finite element modeling package. The ideal case will be if the decrease in the ultimate strength can be determined as a function of the normalized modulus such that $\frac{S_u}{S_{u0}}$ is a function of $\frac{E}{E_0}$ where S_{u0} is the unheated ultimate strength, S_u is the heated ultimate strength, E_0 is the unheated elastic modulus, and E is the heated elastic modulus. The element death feature in ANSYS lacks the capability to model the ultimate strength as a function, and can only model it as a discrete value. Modeling the change in ultimate strength of the resin as a function of the decrease in elastic modulus allows the generalization of these results to any circumstance of thermal degradation. For each model, the unheated uncoated data will serve as a reference state. The experimental stiffness in the elastic region for each state will be compared to this reference state and this ratio of stiffness will be used to compute the equivalent elastic modulus for that state. The stated elastic modulus for each sample cannot be used because all of the samples are of varying thicknesses.

However, because the geometry of the model is constant, the elastic modulus is directly related to the stiffness, so the change in stiffness can be directly correlated to the change in elastic modulus.

4.2 Structural Model

The solid model was created in three types: (1) A monotonic stage where the composite was modeled as a homogenous prism, (2) a complete reproduction of the composite microstructure where the glass fibers were modeled in yarns, and (3) a model based on using thin layers of contacting material.

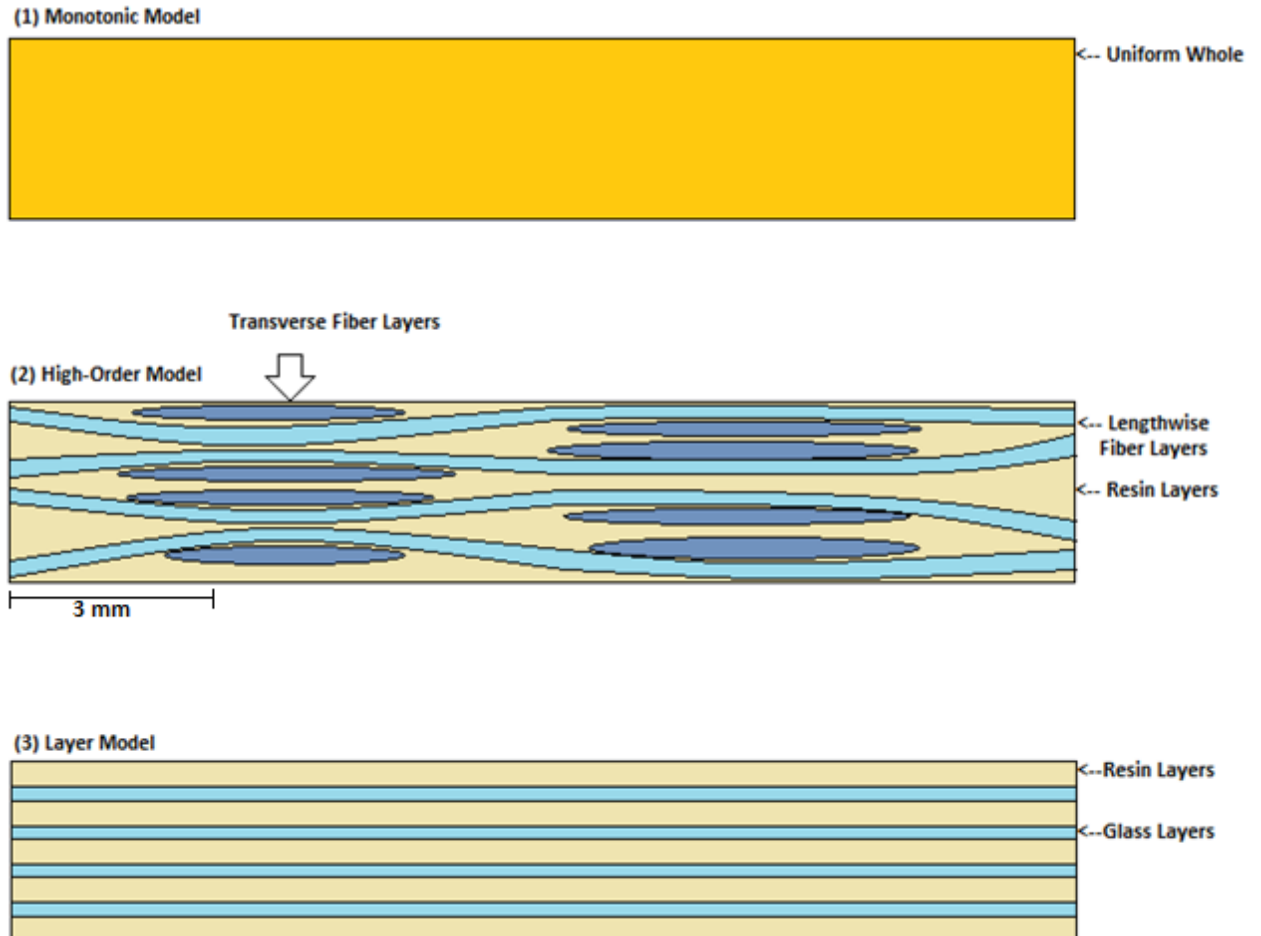


Figure 12: Sketch of Model Side Views for Reference.

The first type was used to replicate the elastic behavior of the model, and understand what mechanical properties of the composite deviate the most from ideal elastic behavior. If the layer and monotonic approaches fail to replicate the behavior of the composite accurately, it is an indication that more is going on than can be accounted for without further experimentation. Even if the model fails verification, the modeling will proceed with caution regarding the veracity of the results obtained.

The complex stage was created to represent the composite geometry exactly and attempt to capture the behavior of the composite exactly, including the pop-in behavior and the strain energy. A number of factors precluded obtaining results from the complex model. The first was the difficulty the software had with storing and reproducing the complex geometry inside the resin layers of the composite. The resin is interspersed into and bonds with the glass-fiber layers in a geometrically complex fashion. This meant that ANSYS was unable to process the IGES file of the geometry that had been generated in another program. Many of the features used to produce the geometry in a separate program were unavailable in ANSYS. The complex geometry of the resin and the complex geometry of the glass fibers produced a second problem. The computers used for the simulation were unable to generate a mesh to cover the geometry of the complex model.

The layer stage was created to address issues that arose in attempts to use the complex model that precluded it from producing any results.

4.3 Material Evolution

Beyond the behavior of the unfired material and the microstructural model was the inclusion of thermal damage and cracking. Element death was used in this circumstance. For element death, the criterion used was one of maximum stress. The commands used can be found in Appendix A. The damage was assumed to occur exclusively in the resin. Using the Skovron model as a baseline, and using graphical analysis with the data, an improved model for the thermal damage was found. This model

improves or maintains the error for every experimental result. (The magnitude of the improvement is discussed after Figure 14)

$$\frac{E_D}{E_0} = e^{\left(-0.376H\left(1-\frac{6.3}{H}\left(0.937\frac{25}{\phi}\right)^{\frac{\phi t}{240}}\right)\right)} \quad (6)$$

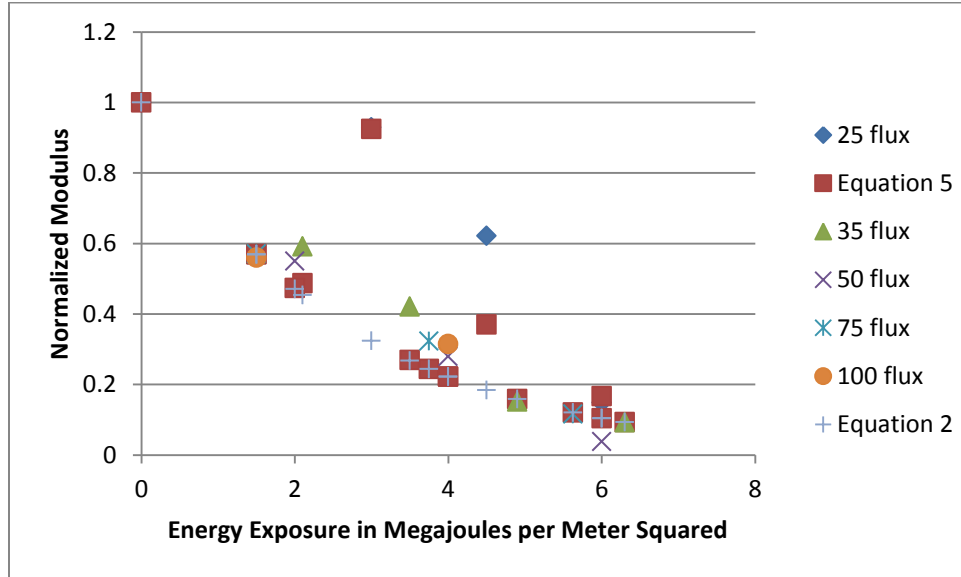


Figure 13: Uncoated Model Fit

The uncoated data was the data initially used to analyze the Skovron model and determine where it was deficient. Figure 13 made it apparent that the areas that displayed the greatest deviation from the modeled behavior were the intermediate energy exposures. The large energy exposures and the very small energy exposures behaved appropriately, but the modulus at intermediate energy exposures were overestimated for high fluxes, and underestimated for low fluxes. This implied that the basic functional relationship was accurate, and the power of the exponent was what needed alteration. The power of the exponent needed to be one at zero energy exposure, zero at infinite energy exposure, and vary according to heat flux at intermediate levels of energy exposure. No correlation was observed between modulus and time. There are four constants used in the equation. The 0.937 was a constant with no

physical meaning. Two hundred and forty is the product of two factors: 60 (to convert seconds into minutes) and 4 (to normalize by the maximum exposure time of four minutes). Six point three was normalizing by the maximum value of the energy exposure in megajoules per square meter, and 25 was the minimum heat flux in kilowatts per meter squared.

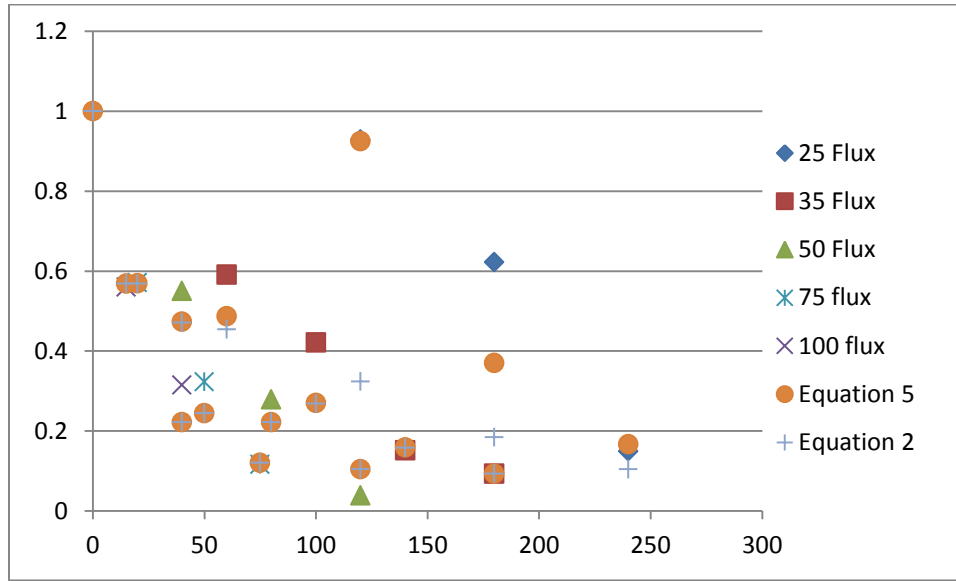


Figure 14: Exposure Time and Flux Dependency of Modulus

The model was then applied to the coated data as seen in Figure 15, to ensure that the model fit for the coated composite data. The equation used was:

$$\frac{E}{E_0} = e^{\left(-0.294 * H * \left(1 - \frac{6.3}{H} * \left(0.937 * \frac{25}{\phi}\right)^{\phi * \frac{t}{240}}\right)\right)} \quad (7)$$

The only difference between Equation 6 and Equation 7 are the initial constants of 0.376 and 0.294, respectively. This difference was the only difference between the uncoated and coated Skovron models and remains unchanged. The new model behaves identically for the coated and the uncoated data. The new model maintains or improves on the fit of the old model in each case. The R^2 values of the Skovron model given earlier of 75.8% and 86.4% were without the inclusion of the two outliers of

$\phi = 25$, where $t_{exp} = 120, 180$. With the outliers included, the R^2 value is reduced to 43.9% for the coated model of Equation 2, and 49.6% for the uncoated model. The new model in Equation 5 and Equation 6 possesses an R^2 value of 77.6% for the coated model and 89.96% for the uncoated model. If the outliers are excluded, Equation 5 and Equation 6 has an R^2 value of 77% for the coated model, and 93% for the uncoated model. The model given in Equation 4 and Equation 5 can be used to generalize the results of this model to any heating conditions if the heat flux and exposure time are known.

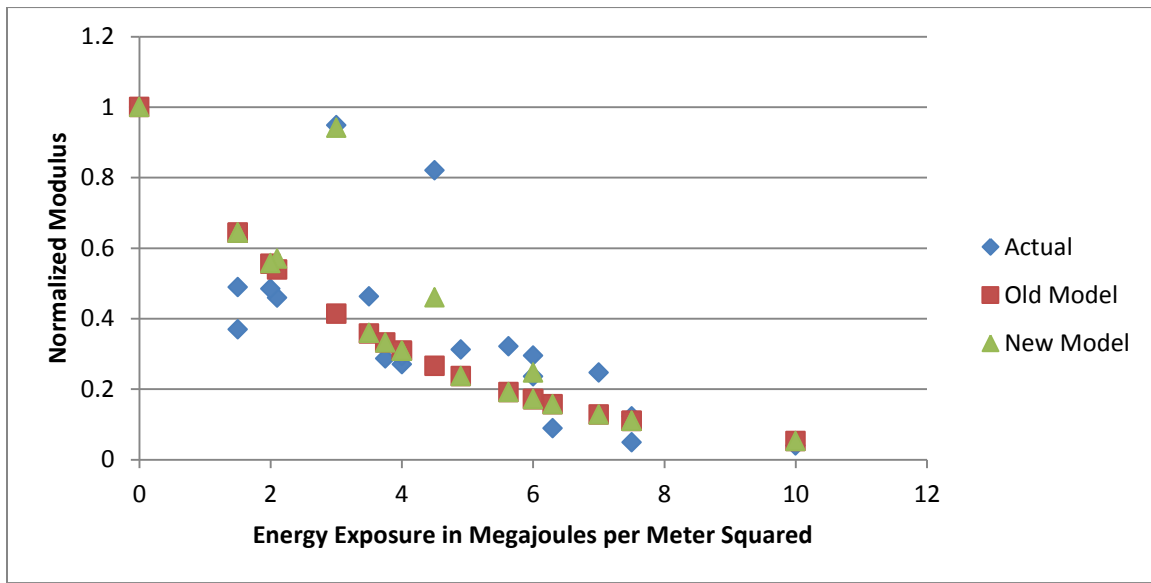


Figure 15: Coated Model Fit

Element Death was used to simulate cracking. Cracking is a physically complex occurrence that requires a lot of information and prior knowledge beforehand to model accurately. However, the net effect of cracking is that the material has nearly zero strength in the area of the crack. This is modeled numerically by using Element Death to reduce the elastic modulus of an element to 1.0×10^{-6} whenever the stress in a given element exceeds the failure stress. Prior to element death occurring, the stiffness of

the element is determined by the material the element is composed of. Element death is supported by virtually any element (with a full list available with the ANSYS help files) and can be made a component of any user-created elements as well. Element death reduces the strain, stress, and all other quantities related to the element to zero, and reduces the stiffness of the element to 1.0×10^{-6} . Element death can only be applied in solution processing, and can only be applied to all elements selected. The challenge of using element death then becomes to select the appropriate elements. Element death persists for only a single load step, so the elements to be killed must be stored and recalled each load step. However, the stress values for each element can only be stored in postprocessing, and the table used to store the stress values for each element is not saved when exiting postprocessing. The command code (“code snippet”) in Appendix A, therefore, selects exclusively the resin elements that have failed, stores these elements as a component, and then saves that component to an external file. This external file is then read when the solution restarts and is overwritten at each load step. This code snippet is a heavily-modified version of a general example copied into Appendix A for reference from the help files of ANSYS finite element analysis software.

Three sources were used for the failure stress S_{ut} used in the code input for the finite element model. First, the theoretical maximum stress in the resin was found using equation 3. The load and deflection used was the load and deflection immediately before pop-in occurred. Second, the monotonic model was used and the maximum stress at the load where pop-in failure occurred was recorded and used as the failure stress. Third, the layer model was used and the maximum stress in the resin was found at the load where pop-in failure occurred was recorded and used as the failure stress. None of these values produced the appropriate behavior. Element death on its own failed to replicate the curve accurately after further exploration. The inclusion of a bilinear elastic modulus (as seen in Equation 5) allows the prevention of an overrun of stress between executions of element death. If a

bilinear elastic modulus is not included, too much of the material becomes overstressed before element death can be applied and the reaction force drops to zero when element death occurs. The values producing the response that matched the control force versus deflection curve the most closely were 550 MPa for the Element Death criterion, and 600 MPa for the bilinear yield strength (S_y in Equation 5) for the monotonic model. For the layer model, the values that matched the undamaged uncoated composite data the best were 63 MPa for the resin element death criterion, 64.26 MPa for the bilinear criterion for the resin, and 900 MPa for the bilinear criterion for the glass fibers.

4.4 Simulation of Monotonic Response

Preliminary research focuses on accurate modeling of the elastic modulus. The model focuses on assuming the composite is uniform and replicating the elastic response of the actual composite. Figure 12 shows the configuration for 3-point bending in experiments. Contact is strongly nonlinear, and using boundary conditions relying on contact with three sets of curved surfaces increases the complexity of the finite element model to the point where it is nearly impossible to find errors or obtain accurate results from it. The force was represented as a pressure over the lower specimen surface. This avoids issues with the deformation of the cylinder and applies the force evenly as in the actual experiment.

Because the model was producing erroneous results when the full size of the model was included, the model was reduced using symmetry to one-quarter of the size of the mechanical experiment. Figure 16 shows the quarter-model after all loading and boundary conditions were imposed. Reducing the size of the model also exposes the center surface of the cylinder where the load is imposed, allowing the pressure to be imposed on the center surface, increasing the accuracy of the model. This reduces the contact to two pairs of surfaces as seen in Figure 16, allowing the model to be accurate and solve within a shorter period of time.

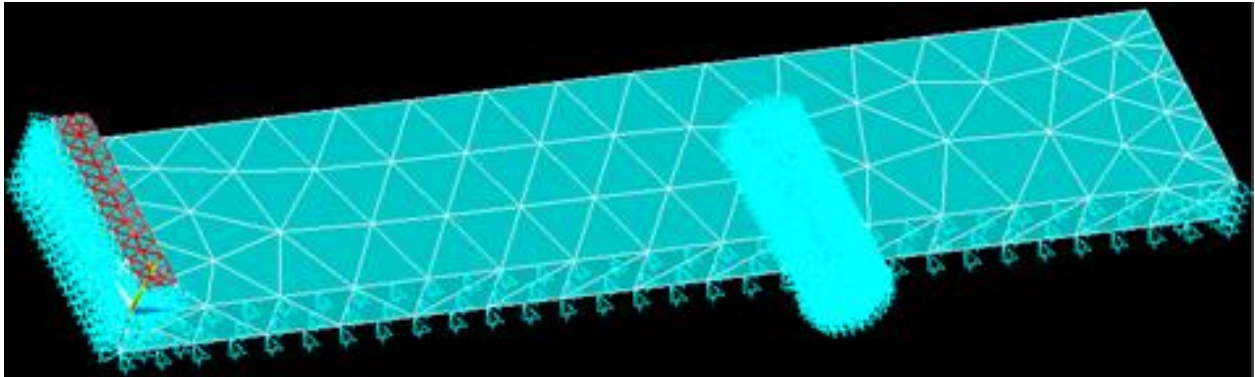


Figure 16: Quarter Model, Reduced boundary conditions

4.5 Layer Model Construction

The layer model was devised to be less complex than the full model, and more complex than the monotonic model. This enabled the model to replicate the experimental behavior of the composite with the processing power available. The layer model provides an accurate representation of the behavior of the model, as shows in Figure 17.

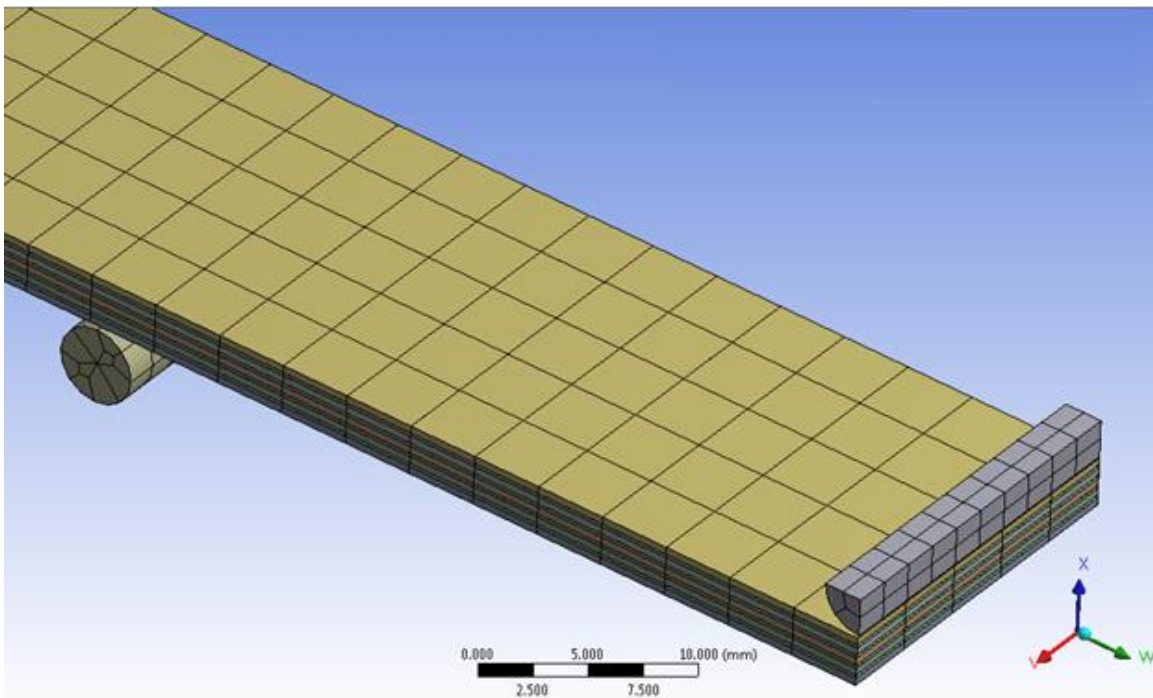


Figure 17: Layer Model Mesh

The glass fiber layers here are far smaller than in the complex model, because it is a consistent layer, rather than weaving in and out and possessing varying thicknesses, and with zero resin interspersed into the mat. The volume in a given layer is the same as the volume per layer in the complex model. The volume fraction was the most important property that needed to be identical for the sake of similarity in the finite element model. Essentially, the thickness of a layer can be found by:

$$\delta_{layer} = (vf)_{mat} \frac{\delta_{total}}{N_{mat}} \quad (8)$$

Here, δ_{layer} is the thickness of a single layer, $(vf)_{mat}$ is the volume fraction of the material in decimal form (e.g. 30%=0.3), δ_{total} is the total thickness of the composite, and N_{mat} refers to the number of layers of the material in the composite. For this model, the total thickness used was 2.8 mm, with 4 glass layers and 5 resin layers, and a glass volume fraction of 30%, for a glass layer thickness of 0.21mm per layer, and a resin thickness of 0.392mm per layer. A more detailed side view can be seen in figure 12.

4.6 High-Order-Model Construction

The complex model was an attempt to directly solve the issues of the monotonic model by replicating the geometry as exactly as possible. The model can be seen in Figures 18 and 19. Figure 18 shows the external view of the model, and Figure 19 shows a wireframe view of the model. Figure 19 shows the most difficult problem to overcome with this model: the multiple instances of contact and the curves of the resin produced by molding itself to fill gaps left by the non-uniform nature of the glass-fiber mat of the high-order model renders finite element analysis virtually impossible. Because of this, no results were obtained from this model. The computer power available was insufficient to permit the meshing, modeling of contact, and the solving necessary to obtain results from this model. The number of nodes and elements used did not come close to the limit of the software. The model was merely

unable to solve in a reasonable time frame (The model was given a day to solve and the run had not finished in this time frame). This model possesses great potential for future study under circumstances with more power and time available for processing and solving. The construction of the model, however, was instructive for principles used in the construction of the layer model. The repetitive nature of the complex internal structure suggests that the internal structure can be replicated with a large amount of fidelity using a geometrically simplified model. Although no results were obtained from this model, the construction of the model was an important step in the modeling process. If results with a higher fidelity could have been obtained, then the use of this model would have proven the simplest solution and the most general solution for use with the nanopaper coated glass-reinforced polyester composite being used.

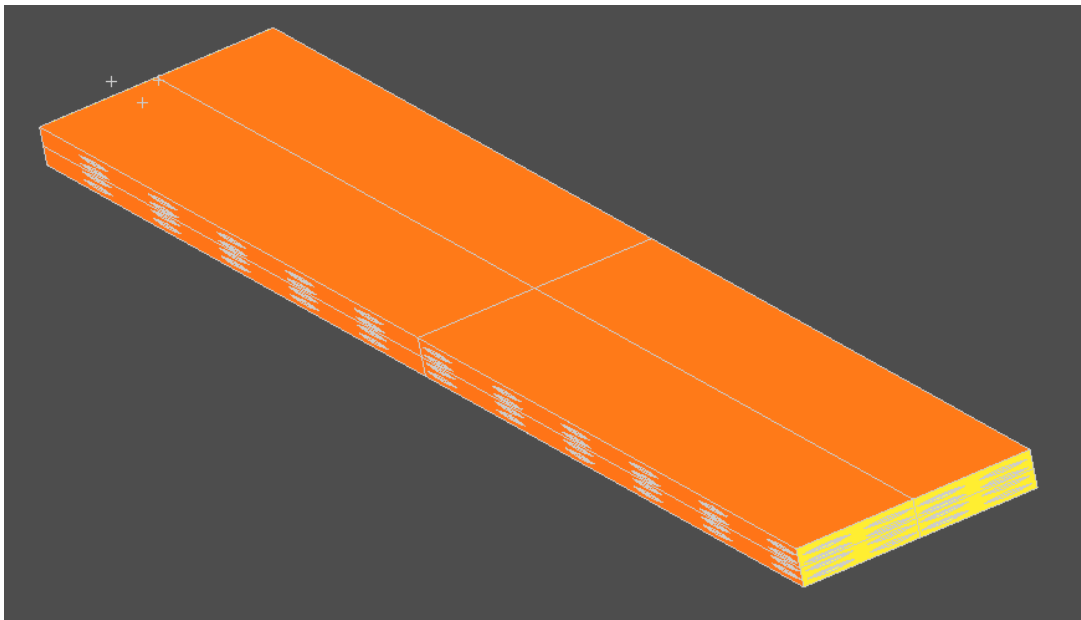


Figure 18: External View of High Order Model

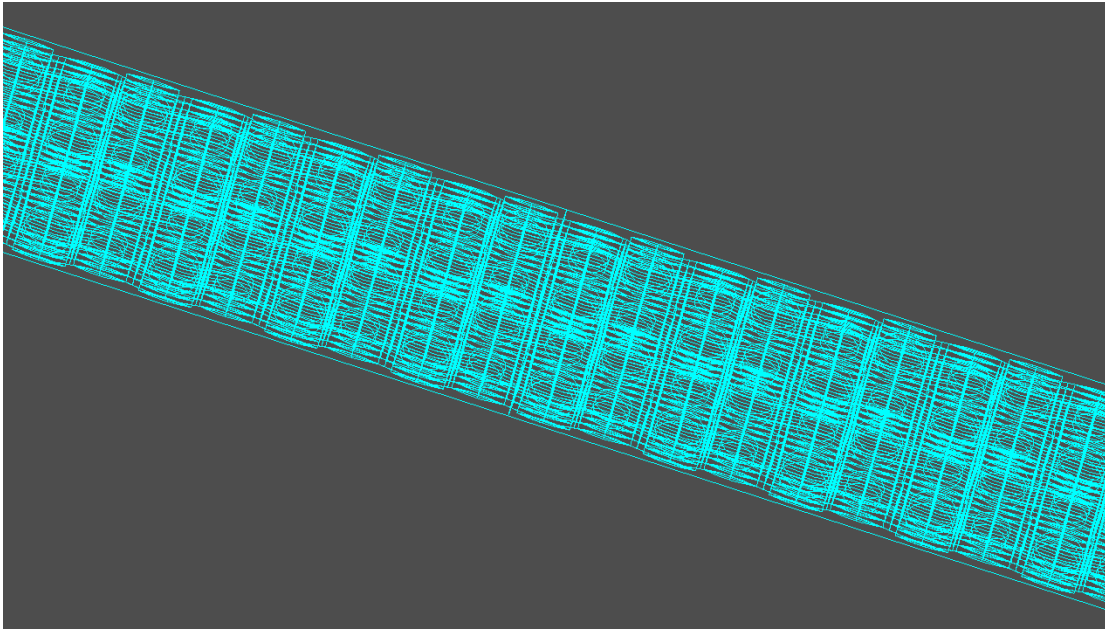


Figure 19: Internal view of High-Order Model

4.7 Interpreting the Results

The results can be divided into two categories: the verification results and the cracking results. Interpreting the verification results can be done graphically by checking against the four verification standards previously established. The most important issue for the verification of results is verifying that the overall shape of the graph is the same. If the shape can be matched, then matching the actual values becomes a matter of tuning, and can largely be attributed to discrepancies inherent to the modeling process. The cracking results are more difficult to process. The interpretation of the cracking results will depend on the format of the output of the results. There are three elements that need to be established in the model: the point of origin for cracking, the order and direction of elements that crack, and the overall final pattern of cracks after failure has occurred.

The exact point of origin for cracking will be the most questionable of the results. It is heavily dependent on many factors including the imperfections on the surface, and the porosity of the resin. It

will vary from sample to sample, and will be distributed stochastically, but is generally related to the absolute maximum stress in the composite. However, the model should allow the most common failure points to be identified. The one or two points that are most likely to fail can be identified, and further failures will be distributed around that point, becoming less common as the stress in those surfaces decreases, and increasing when the stress increases again near the edges or contact points. The origin for cracking is possible to find from numerical modeling in a few ways, depending on the processing. The first is by looking at the stress and displacement. The cracked elements should be unable to bear load, and will therefore be outliers in stress and strain. The points of origin for cracking can therefore be found by inspection from a graphical representation of the stress and displacement in each element. This method does not exclude points where the composite is bearing no load. The other method that is more rigorous is to create an element table of the material property used as a criterion for element death, and select all elements above the critical value in that table. This method relies on the element death command functioning as intended, but will include only elements that are intended to be killed.

The direction of cracking should be more consistent; the direction of cracking generally is determined by the relative levels of stress and the geometry within the composite, rather than the absolute stress. The direction of cracking can be found in a method similar to the method used to find the point of origin. The graphical representations of stress and displacement are analyzed at varying load steps to determine the direction of crack growth. The areas where an element fails while not adjacent to an existing crack represents an area where a new crack has emerged, and the areas where an element fails adjacent to an existing crack represents that the crack will grow in that direction.

The overall pattern of cracks can be found by looking at the final load step. This load step will be at a lower value of force than the maximum value as indicated by Figure 11 (the verification diagram), but will be after the failure of a number of elements. There are two ways in which the cracking can

replicate the behavior of the material: it can either crack such that (1) the strength decreases linearly, roughly tracking the average displacement value, or (2) it can track the behavior of the material exactly, precisely replicating the pop-in failure that occurs. If the model fails to replicate this at a rate sufficient to match the behavior of the material, adjustments may be needed to the ultimate stress used or refinement of the mesh may be required.

The order and nature of the development of the cracks will be crucial to understanding the cracking behavior of the composite. It will also be important to look for the effect of the heat damage on the pattern of the cracks. Theoretically, the heat damage should reduce the effect of the lack of reinforcement at the centroids of the unit cells, by reducing the strength of the elements around these stress concentrations. However, there are seventeen experimental data points for the coated composite, and seventeen for the uncoated composite. It is not feasible to obtain the cracking data at all data points. Therefore a representative sample of the data points will be taken for the coated and uncoated composite. The data points selected are (1) the control, (2) $\phi = 25, t_{exp} = 180$, (3) $\phi = 50, t_{exp} = 40$, and (4) $\phi = 100, t_{exp} = 40$. These points correspond to the undamaged composite, and points of approximately seventy-five, fifty, and twenty-five percent of the undamaged modulus, respectively.

Chapter 5: Numerical Modeling Results

5.1 Monotonic Model Results

The first method applied, of using a force and analyzing the displacement, produced mixed results. The simulation in Figure 20 was done at 240N, and the experimental data [Skovron et al., 2012] indicates the deflection at this point should be 2mm. The deflection indicated by Figure 20 is 1.99mm, for an error of -0.5% compared to the experiment Control-A shown in Figure 11 (the verification diagram).

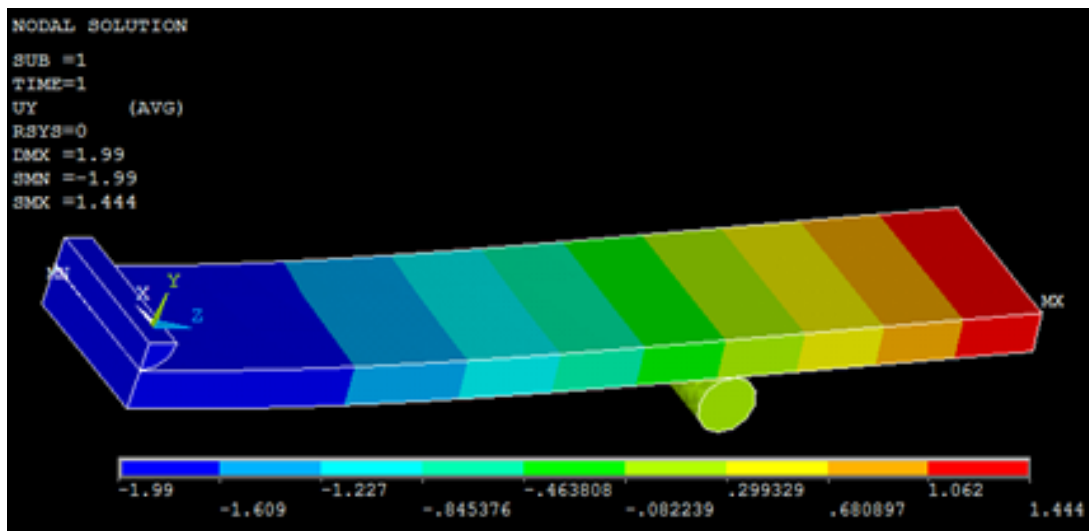


Figure 20: Resulting Displacement in Quarter-Model of 3 Point Bending Simulation

However, while applying a force and analyzing the resultant displacement works for individual points from the force versus displacement curve, this effort fails even with the application of Element Death and a bilinear model for the elastic modulus (as seen in Equation 5) for the elastic modulus. The failure of these behaviors to replicate the behavior of the material can be seen in figure 21, which illustrates the use of various forms of material behavior to attempt to replicate the reference experimental data (Control-A, also shown in Figure 11)

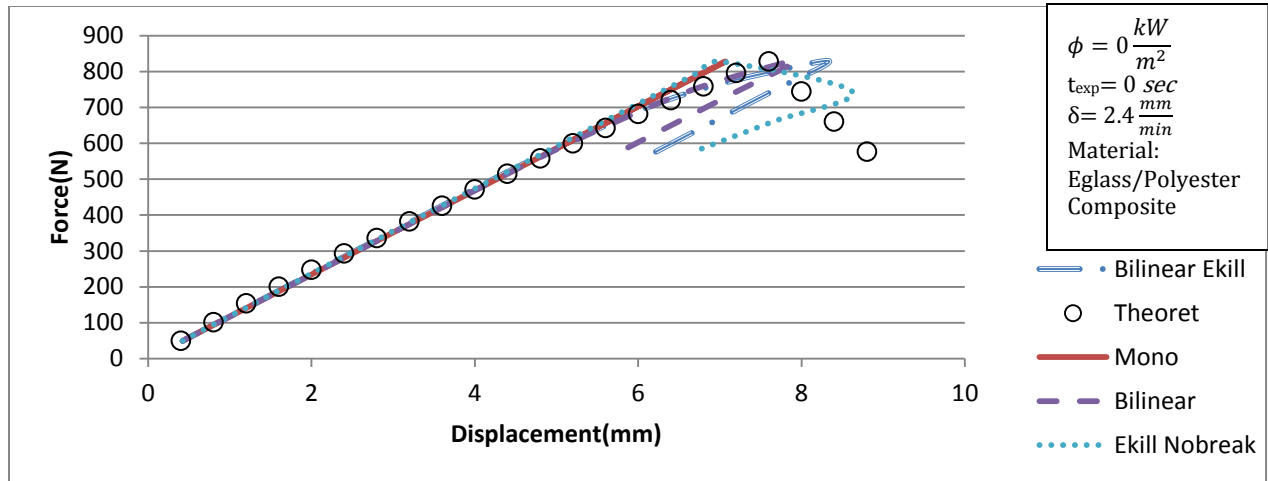


Figure 21: Monotonic Model, Force Driven Methods

The other testing done on the monotonic model was the testing of Element Death and the bilinear modulus. The monotonic model incorporated the weakening due to heating and the progressive failure of elements, for the purpose of proving that the concept was sound. Figure 21 shows the uncoated and unheated experimental data and shows the model under various permutations of those two features . Figure 21 shows that the bilinear criterion from Equation 5 reduces the strength of the composite before and after failure, but fails to weaken the composite enough to match the experimental force versus deflection curve. Element death alone produced an appropriate amount of weakening, but failed to match the elastic portion of the curve. A combination of bilinear and element death features produce the correct amount of weakening for the monotonic model, and should therefore function correctly in the more complex models. However, the crack propagation pattern is potentially inaccurate because of the simplicity of the geometry involved, and its differences from the composite. In addition, the difference between the failures in the resin and the failures in the glass fibers cannot be obtained from the monotonic model, limiting its usefulness.

For the purpose of testing, deflection increments of 0.4mm, corresponding to 10 seconds in the actual experiment, were sampled from the experimental data. The monotonic model was successful in what it was intended to do. It replicated the elastic behavior of the model and served as a proof of concept for the features used to model the non-elastic regions of the composite. The inconsistencies of the model with the experimental data were anticipated and understood. The model was sufficient to allow the construction of the complex-model and the layer model. Figure 22 introduces the displacement-driven results. Element death alone was not performed because the prior force-driven model indicated it was less effective than any other method.

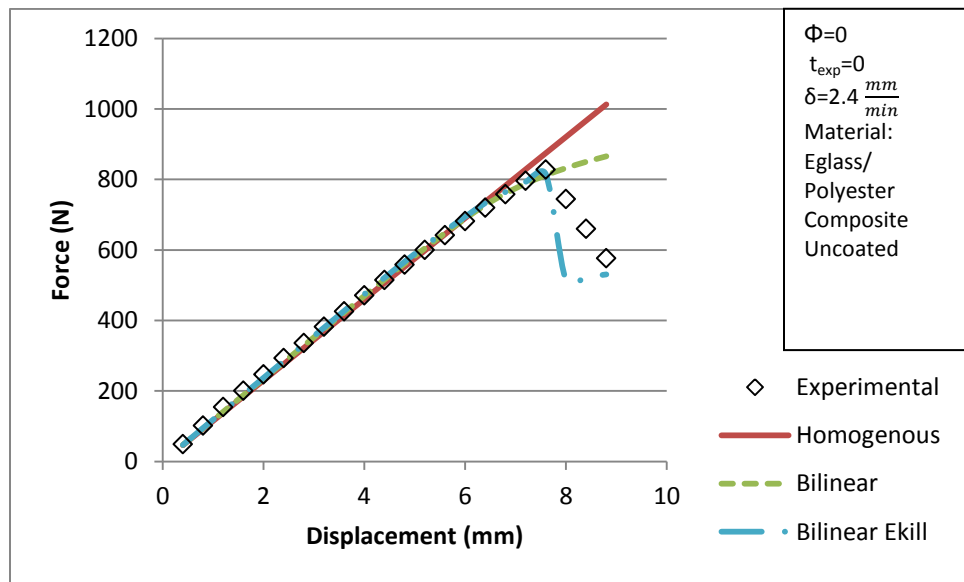


Figure 22: Monotonic Model Methods Comparison

One interesting set of results that was obtained from the monotonic model were results regarding crack progression. The results for the monotonic model regarding crack progression were superior to the results obtained for the Layer model. There are several reasons this could be the case, which are discussed in depth along with the cracking results for the layer model at the end of section 5.2. Figures 23-25 show the progression of cracking under a displacement of 6.8, 7.2, and 7.6 millimeters

for the conditions from the Control-A data (“Experimental” in Figure 22). “Support Cylinders” are the cylinders that were static and defined the span, and the “Load Cylinder” is the dynamic cylinder that defined the displacement rate. “Killed Elements” are elements that were deactivated by the EKILL command and have effectively zero stiffness. The composite is the main body of the composite, represented as a homogenous whole.

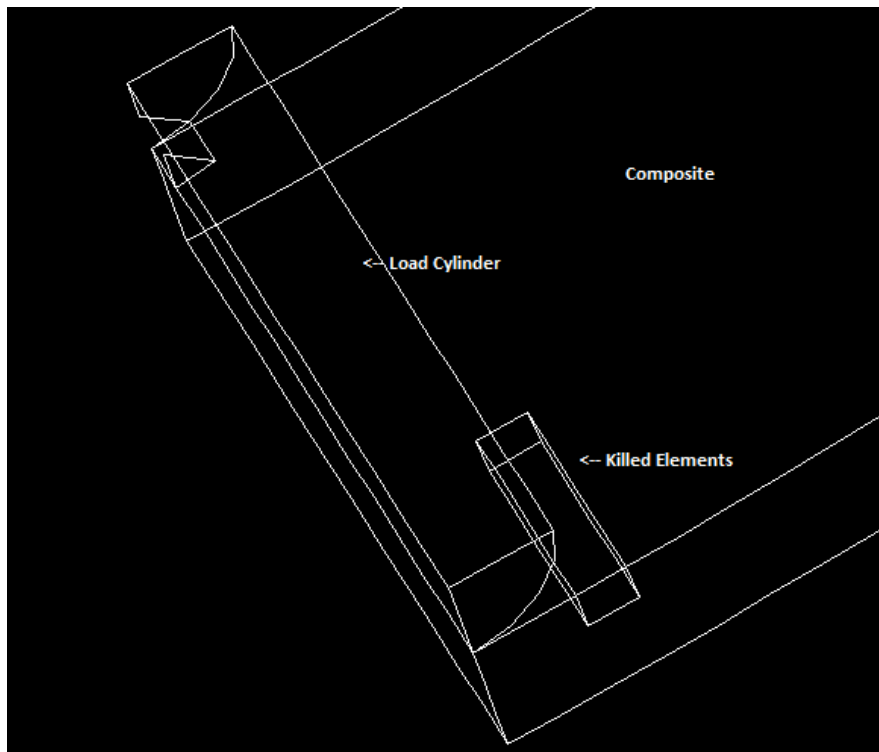


Figure 23: Unheated, Uncoated Model with a deflection of 6.8 millimeters

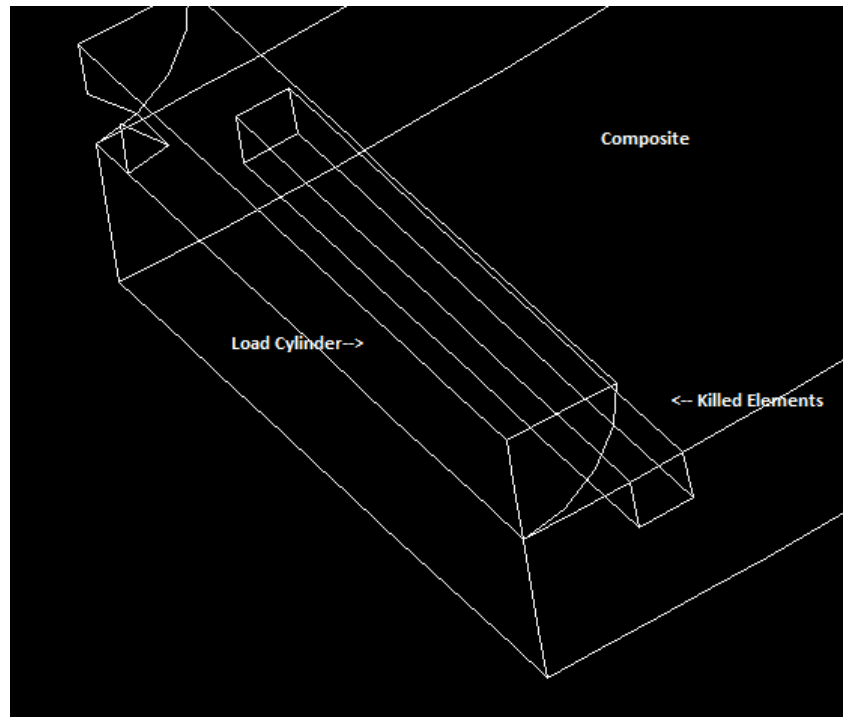


Figure 24: Unheated, Uncoated Model with a deflection of 7.2 millimeters

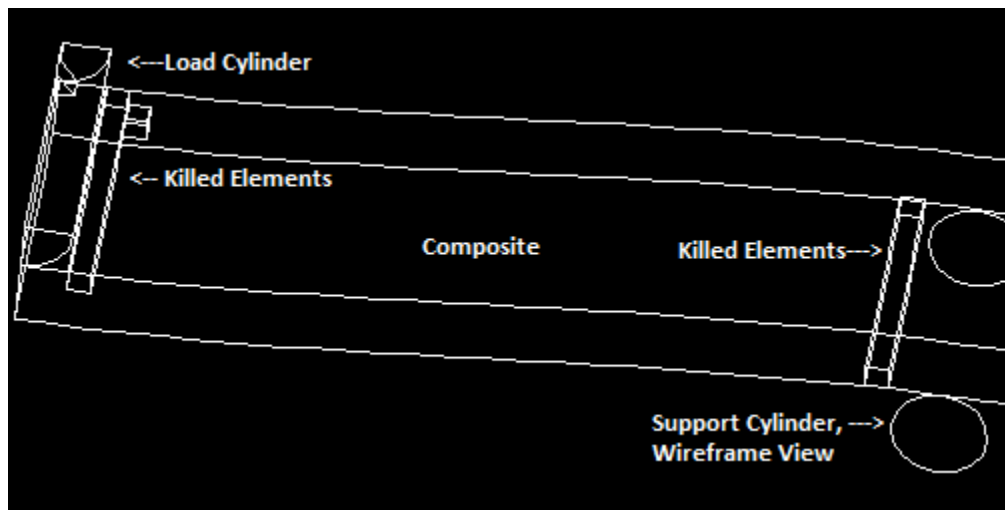


Figure 25: Unheated, Uncoated Model with a deflection of 7.6 millimeters

5.2 Layer Model Results

The model captured the appropriate shape of the stress distribution in the resin. The stress distribution in the resin and the glass fiber layers controls the cracking behavior of the composite. The control force versus deflection curve can be seen in Figure 26 for the uncoated composite for the bilinear and bilinear with element death models. Pure element death behavior was not performed because indications from the monotonic model implied it was less accurate than any other method. The experimental data is displayed for reference.

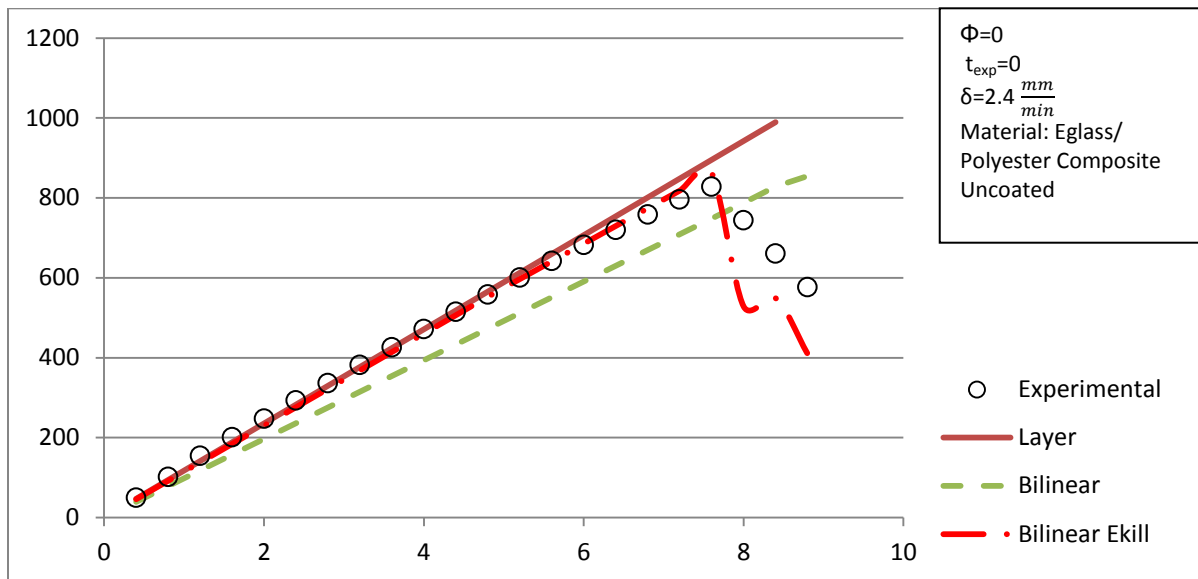


Figure 26: Layer Model Methods Comparison, Control-A experimental data

Table 2 shows the mean for the absolute value of the error for each heating condition selected for crack analysis, for the coated and uncoated models. This characterizes the accuracy of the model with respect to its replication of the average behavior of the model, particularly the behavior in the elastic region because most of the data points averaged are in this region.

Table 2: Mean Value of Error for Heating Conditions Selected for Crack Testing

Arithmetic Mean of Absolute Value of Error	$\phi = 0 \frac{kW}{m^2}$ $t_{exp} = 0 \text{ sec}$	$\phi = 25 \frac{kW}{m^2}$ $t_{exp} = 180 \text{ sec}$	$\phi = 50 \frac{kW}{m^2}$ $t_{exp} = 40 \text{ sec}$	$\phi = 100 \frac{kW}{m^2}$ $t_{exp} = 40 \text{ sec}$
Coated Model	12.35%	11.43%	20.49%	14.80%
Uncoated Model	6.75%	13.10%	10.17%	18.76%

Table 3 shows the R^2 with respect to each of the heating condition points selected for testing. Table 3 provides the value of R^2 across the entire force versus displacement curve. This represents how well the model was able to replicate the exact value of the experimental data. The correlation is the weakest for the uncoated model because of the difficulty of replicating the unique behavior of each force versus deflection curve. The correlation is the strongest for the unheated control models in each case. The uncoated 100, 40 model is an outlier because of the difficulty of replicating the constant-force behavior that its force versus deflection curve displays. The 50, 40 model possesses the second lowest value because of the difficulty of limiting the magnitude of weakening induced by element death.

Table 3: R^2 value for Heating Conditions Selected for Testing

R^2 Value	$\phi = 0 \frac{kW}{m^2}$ $t_{exp} = 0 \text{ sec}$	$\phi = 25 \frac{kW}{m^2}$ $t_{exp} = 180 \text{ sec}$	$\phi = 50 \frac{kW}{m^2}$ $t_{exp} = 40 \text{ sec}$	$\phi = 100 \frac{kW}{m^2}$ $t_{exp} = 40 \text{ sec}$
Coated Model	89.26%	87.5%	79.65%	86.57%
Uncoated Model	92.42%	70.17%	79.6%	32.46%

Table 4 shows an error for each model based on the percent difference between the left-sided Riemann sum of the experimental data and the model data. This provides an approximation of the error of each model in reproducing the area under the force versus deflection curve. Generally speaking, this form of verification had the lowest percentage of error. The 50,40 data has the highest value of error because the composite was atypically strong under this condition, as was seen in Figure 10.

Table 4: Percent Difference in Riemann Sums for Points Selected for Testing

Percent Difference in Riemann Sum	$\phi = 0 \frac{kW}{m^2}$ $t_{exp} = 0 \text{ sec}$	$\phi = 25 \frac{kW}{m^2}$ $t_{exp} = 180 \text{ sec}$	$\phi = 50 \frac{kW}{m^2}$ $t_{exp} = 40 \text{ sec}$	$\phi = 100 \frac{kW}{m^2}$ $t_{exp} = 40 \text{ sec}$
Coated Model	7.43%	-0.32%	-12.50%	-7.05%
Uncoated Model	-5.16%	7.99%	-13.30%	8.05%

Overall, the model matches with a respectable amount of fidelity. Improvements are obviously possible to the accuracy of the model, particularly its ability to exactly replicate the behavior of the composite as seen in Table 3, but for the purpose of estimating the stress distribution and cracking, all of the forms of error remain within acceptable parameters.

With the verification accomplished according to the prior knowledge regarding the force versus deflection curve, the cracking results can be analyzed. Figure 27 shows the only result obtained for cracking for all situations in the model. From one load step to the next, the horizontal crack developed instantaneously across the entire material, in all cases. The notation is the same as Figures 23-25, except “Area of Change in Contact” refers to a behavior unique to this model that may indicate additional cracking, as discussed later.

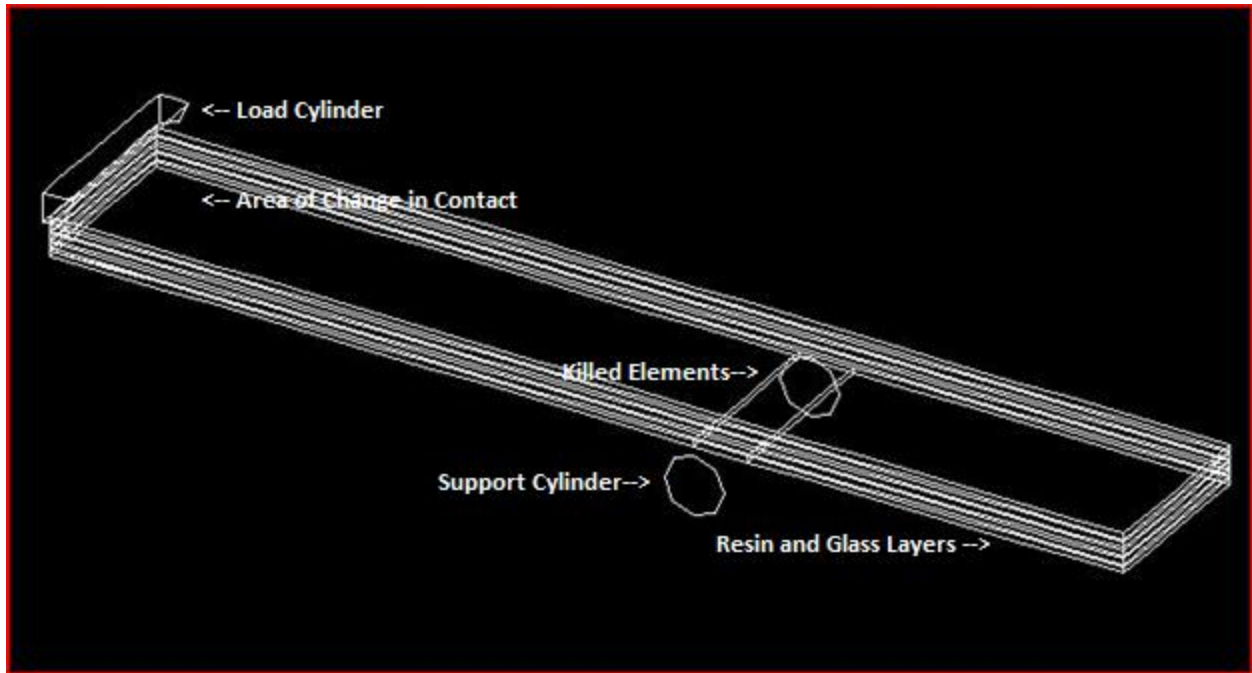


Figure 27: Cracked Elements

The reason poor results were obtained regarding cracking was due to element size. The default mesh that was automatically generated by the program contained 846 elements. A convergence study done with 1816 elements produced results dramatically different than Figure 27. However, the time this model took to solve, combined with the processor power used, made the use of this number of elements prohibitive when combined with the trial-and-error approach required to control the element death behavior. However, more information can be gleaned from a notification given by the finite element model. The finite element model indicated in cases where a secondary failure occurs on the force versus displacement graph, a change in contact status had occurred. All contacts except the contact between the cylinder applying the displacement and the upper resin layers were essentially rigid. The change in contact status implies that at that point, a second crack opens on the top layer of resin. This failure in theory should then cascade downward, as the ability of each layer of resin to bear additional load goes to zero, and the reaction force remains at a constant value.

Chapter 6: Predictions

6.1 Elastic Modulus

The first predictive model to be formed was the model involving the elastic modulus. The elastic modulus is affected by the geometry of the sample and the damage caused by heating. The only difference between the coated and the uncoated models involves a constant factor introduced to the uncoated model of 1.1. The elastic modulus of all the uncoated models was increased by 10% to compensate for the inherent tendency of the finite-element model to under-predict the force response. The coated model did not need this increase possibly because the nanopaper coating has a low stiffness implying that its proportion of the thickness does not contribute to the elastic modulus. The formula (9) used assumes that the effect of thermal damage alters the initial slope of the force versus displacement curve term of the equation for the elastic modulus of a beam. This allows that term to cancel out and the model modulus to become independent of the force or displacement applied. The span cancels out as well because that was held constant across all tests. The equation directly produces the single elastic modulus used for the monotonic model. For the layer model, the only value to change is the initial elastic modulus, with the change being applied uniformly to the glass and the resin. The ratios obtained from these equations are used along with the energy exposure value for each case and a set of constants

$$\frac{E_m}{E_0} = \omega \left(\frac{d_0}{d_m} \right)^3 \frac{b_0}{b_m} \quad (9)$$

Above can be seen the thickness d , and the width b for both the model and the undamaged composite, the thermal damage parameter ω , the model elastic modulus E_m , and the undamaged elastic modulus E_0 . This equation provides for the modeling of the modulus of the composite in virtually any service condition.

The modeled force response of the composites can be used to analyze the validity of this prediction over a broader range of heating conditions. Figures 28-35 show the full force response curves for each heating condition tested. Figures 28-31 show the data for the uncoated heating conditions, and figures 32-35 show the data for the coated heating conditions. The only case where a significant deviation from elastic behavior can be observed was in the $\phi = 50 \frac{kw}{m^2}, t_{exp} = 40 \text{ sec}$ case, where the model under-predicted the strength for the coated and uncoated composite. Otherwise, as previously shown in Table 2, this prediction matches well with the data. The vertical axes used to plot the data are heterogeneous because the relative magnitudes (magnitude of the force relative to the maximum force for a given heating condition) of the forces are the most important feature of the charts for understanding the behavior of the experimental data and the model, implicitly verified by Skovron in his consistent references to proportions of the maximum force rather than the absolute force.

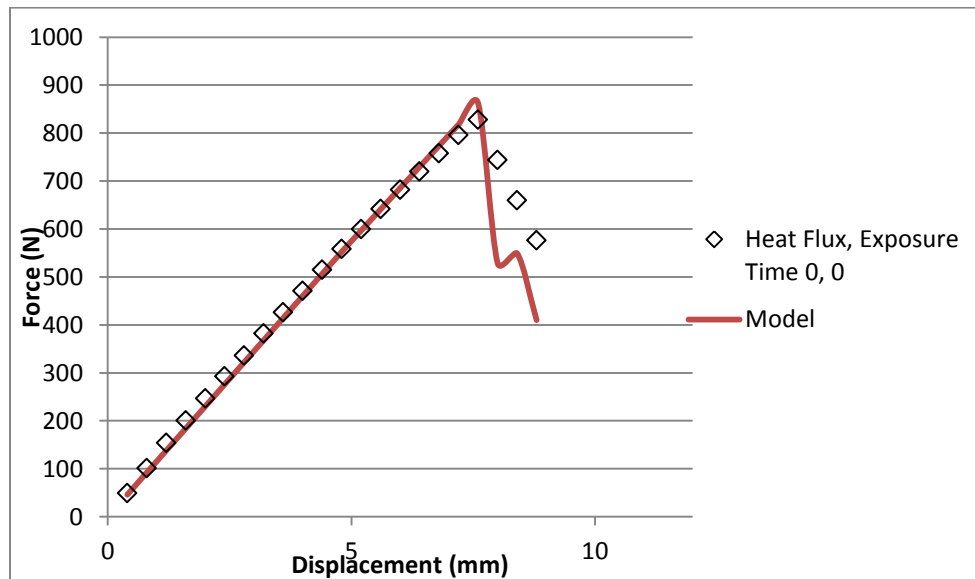


Figure 28: Uncoated and Unheated Layer Model Results

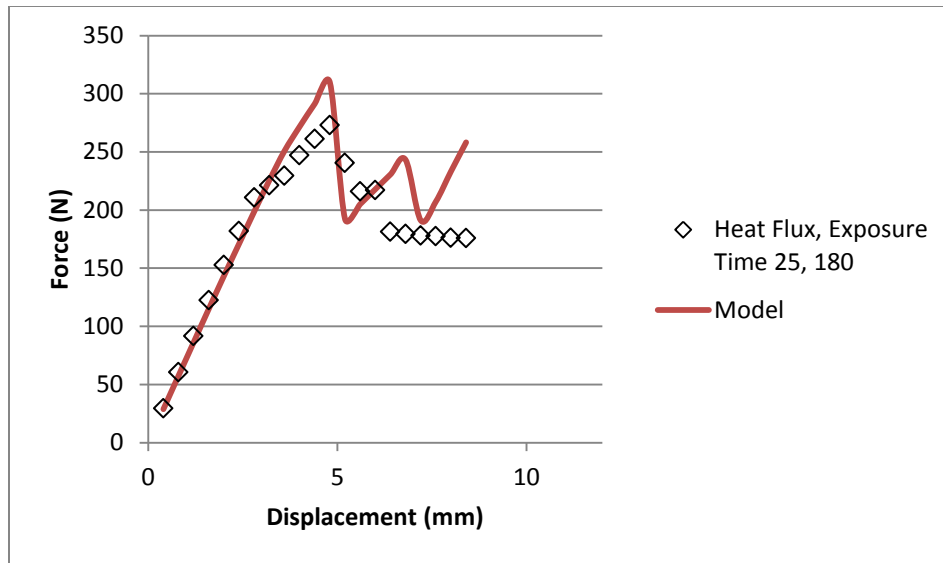


Figure 29: Uncoated $\phi = 25 \frac{kw}{m^2}$, $t_{exp} = 180 \text{ sec}$ Model Results

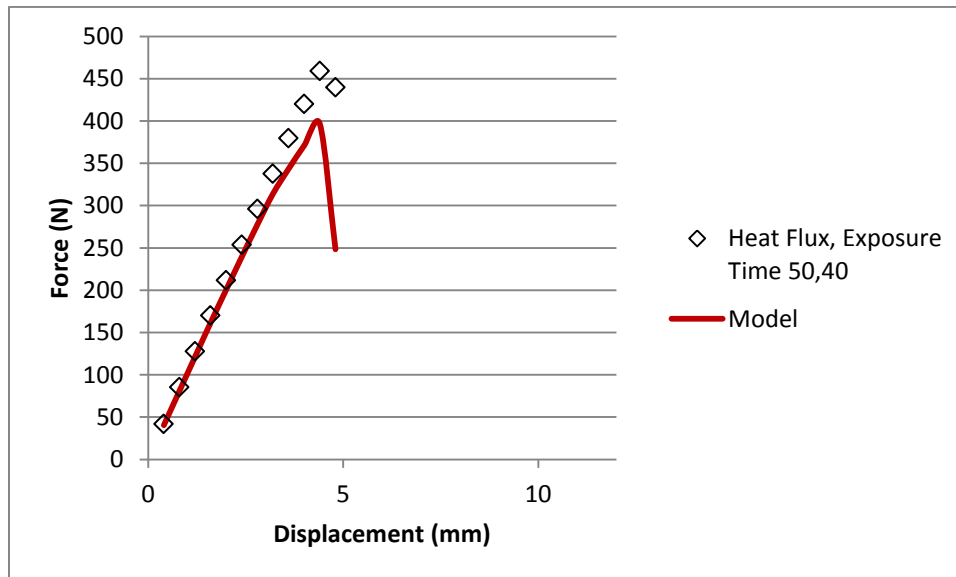


Figure 30: Uncoated $\phi = 50 \frac{kw}{m^2}$, $t_{exp} = 40 \text{ sec}$ Model Results

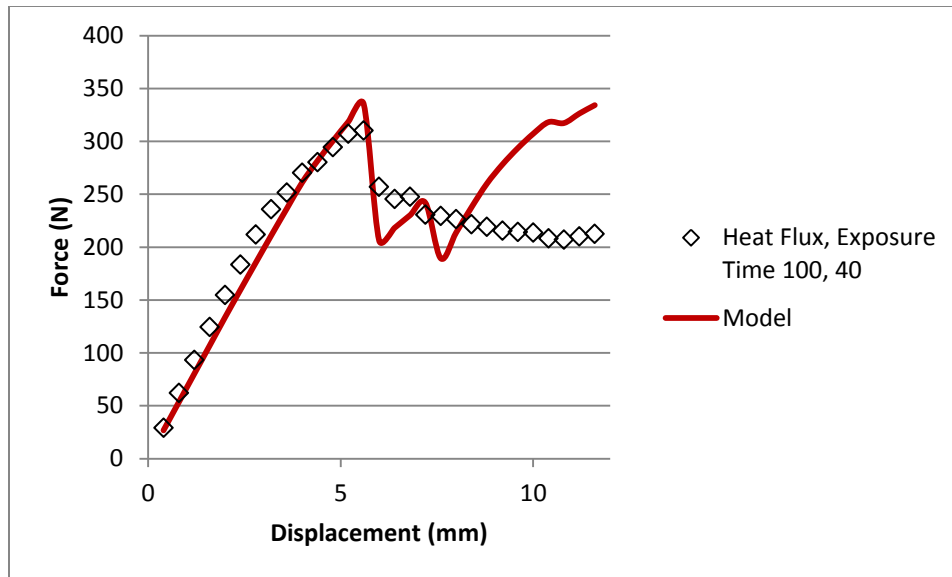


Figure 31: Uncoated $\phi = 100 \frac{kw}{m^2}$, $t_{exp} = 40 \text{ sec}$ Model Results

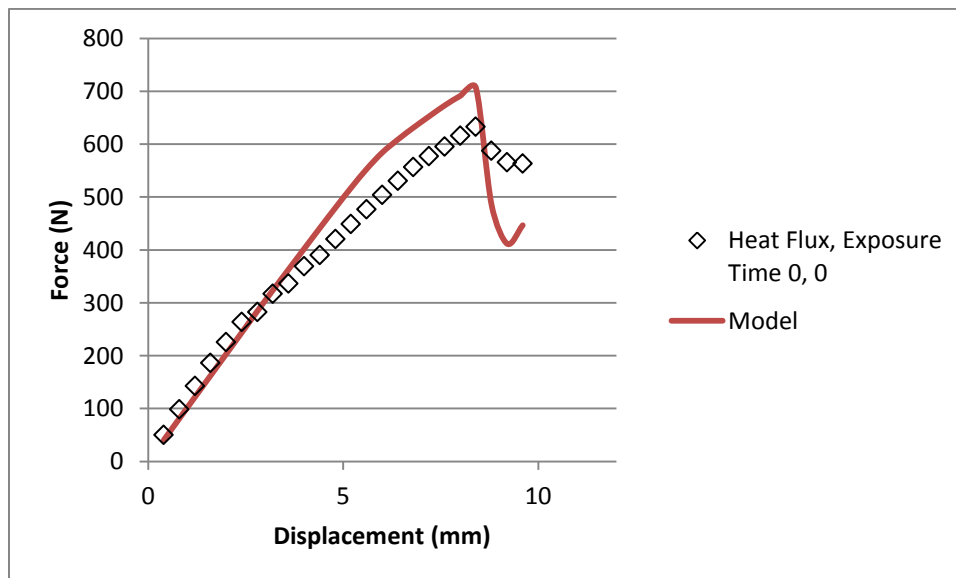


Figure 32: Coated and Unheated Model Results

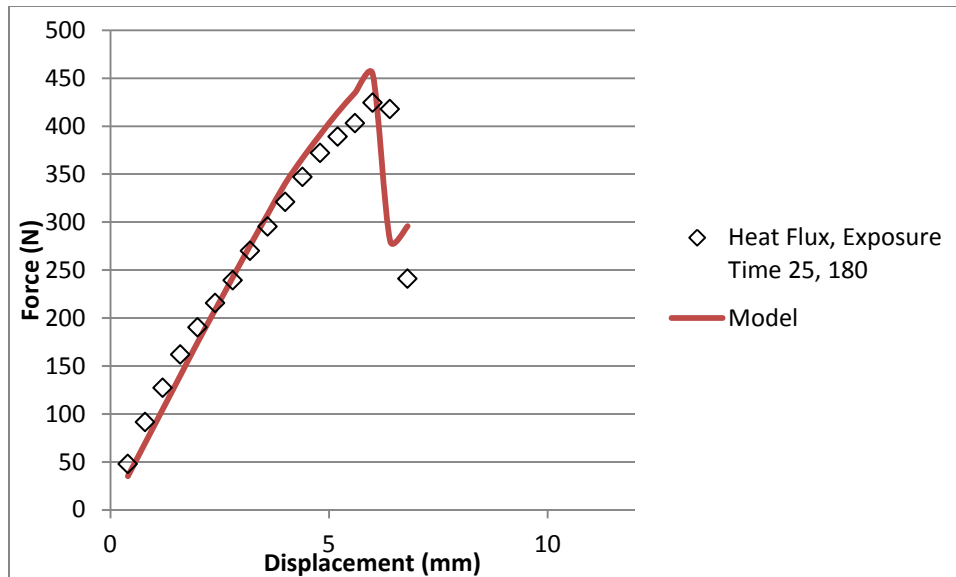


Figure 33: Coated $\phi = 25 \frac{kw}{m^2}$, $t_{exp} = 180 \text{ sec}$ Model Results

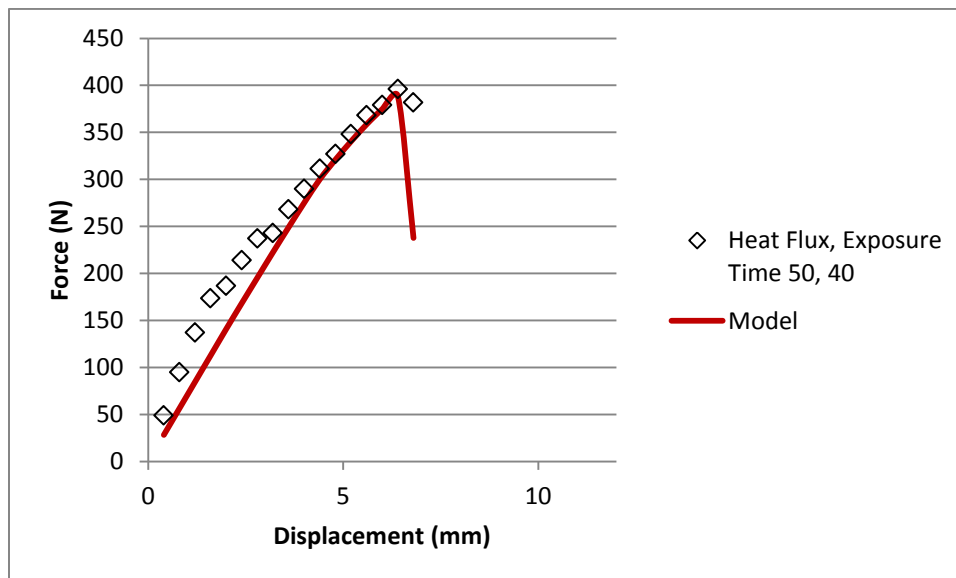


Figure 34: Coated $\phi = 50 \frac{kw}{m^2}$, $t_{exp} = 40 \text{ sec}$ Model Results

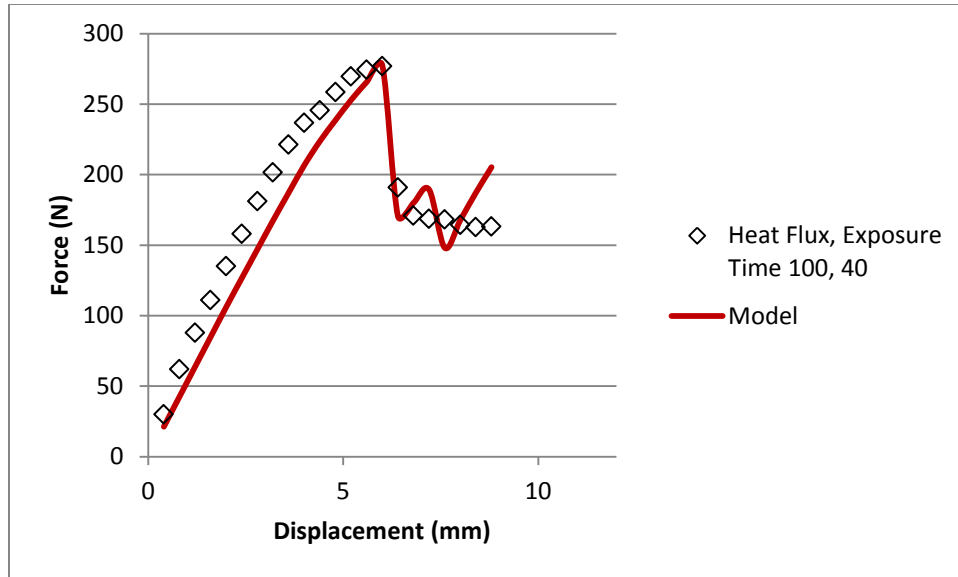


Figure 35: Coated $\phi = 100 \frac{kw}{m^2}$, $t_{exp} = 40 \text{ sec}$ Model Results

6.2 Ultimate Strength

The equation and model for the ultimate strength was based on the ratio formulated for the modeling of the elastic modulus, the damage parameter ω formulated earlier, and the energy exposure for each case. The correlation is solid conceptually and fits well but not exactly for the values tested. The methods used to find the ultimate stress, however, are general. The correlation can be used for an initial value. From this value, the load step of first failure can be observed. If it is greater than the actual load step of first failure, then the maximum value of the ultimate stress for that set of conditions becomes that value. The practice used was to use a value 5% smaller than the ultimate stress at that load step because the bilinear constraint and the large element size causes a slight decrease in the effective elastic modulus as the composite is loaded. If the load step of first failure is smaller than the actual load step of first failure, then the stress is linearly extrapolated from the rate of stress increase for the initial elastic portion of the curve.

$$S_{ut_{UC}} = 0.0257 * \omega * E_D$$

$$S_{ut_C} = 0.0222 * \omega * E_D \quad (10)$$

$$S_{ut_{model}} = S_{ut} * \frac{\frac{E_m}{E_0}}{\omega}$$

Table 5: Model Ultimate Strength Table

Ultimate Strength (MPa)	$\Phi=0 \text{ W/m}^2$ $t_{\text{exp}}=0 \text{ sec}$	$\Phi=25 \text{ W/m}^2$ $t_{\text{exp}}=180 \text{ sec}$	$\Phi=50 \text{ W/m}^2$ $t_{\text{exp}}=40 \text{ sec}$	$\Phi=100 \text{ W/m}^2$ $t_{\text{exp}}=40 \text{ sec}$
Uncoated	63	20	29	24
Coated	51.36	30	26	18.6

Table 6: Equation 6 Ultimate Strength Table

Ultimate Strength (MPa)	$\Phi=0 \text{ W/m}^2$ $t_{\text{exp}}=0 \text{ sec}$	$\Phi=25 \text{ W/m}^2$ $t_{\text{exp}}=180 \text{ sec}$	$\Phi=50 \text{ W/m}^2$ $t_{\text{exp}}=40 \text{ sec}$	$\Phi=100 \text{ W/m}^2$ $t_{\text{exp}}=40 \text{ sec}$
Uncoated	63	24.38	30.43	11.53
Coated	51.36	37.50	17.91	8.21

Along with this equation is the value used for the bilinear yield strength. The bilinear yield strength used was simply 2% greater than the ultimate strength. Equation (10) produces a general fit for both the actual ultimate stress and the ultimate stress used in the model. Table 5 gives the actual values for the model ultimate strength, for the coated and uncoated composite. Using the correlation of equation 6, the R-squared value for this correlation is 93% for the uncoated data and 92% for the coated

data. Figures 28-35 show that the model had difficulties controlling the exact amount of weakening that occurs when pop-in begins. The default failure mode appears to be a drop to approximately 50% of the former maximum force. Samples that unload in modes other than a sharp drop to 50% of the maximum force have higher error percentages in the pop-in region, as can be seen from Table 3.

6.3 Glass Failure

The final element of modeling was the inclusion of a bilinear elastic modulus for the glass material. The modulus used was 1.0×10^{-6} Pa. This modulus was included to limit the excessive recovery in the cases where the composite unloaded with the force converging to a constant value. As seen in Appendix B, the model dealt especially poorly with these cases. The value used for calibration in this case was the 100kW/m², 40 second exposure sample because of its extensive post-failure constant-force segment. The correlation for this case and similar cases remain poor but is increased by the inclusion of this bilinear modulus. The formula used for the yield stress is simple. The strain is assumed to be a constant value, and unchanged by heating conditions, and is the same for the coated and uncoated composites. The elastic modulus is multiplied by this strain value, and the result is the yield stress. The value of the ultimate strain used was 0.01135. Figures 32-35 illustrate that this method of including glass failure limits the recovery in cases where recovery does not occur to a significant extent, but does not fully replicate the force convergence because of the failure of the glass layers that occurs in those cases.

Chapter 7: Conclusions and Future Work

7.1 Modeling

This research involving the use of numerical simulation focused on attempting to simulate the P- δ (force versus deflection) response of the composite using finite element analysis. For this purpose, the modeling process was the most critical part of the process. The accuracy of the respective models was anticipated, and this implies that the various models correspond to the physical situation with varying degrees of fidelity. Element death and a bilinear constitutive model for the elastic modulus were used to model the damage that occurred in the composite for all models. The combination of the two methods produced a series of curves that matched the material behaviors of the composite seen in the experimental data.

The models used were preplanned. It was anticipated that the monotonic model and complex model would fail to replicate the behavior of the composite entirely. The simplicity of the monotonic model made it impossible to accurately represent the behavior of the composite using that model. The complex model was unusable because of the complexity of the geometry and the large number of points of contact involved in the interior. The layer model sufficiently replicated the geometric complexity of the model to match the cracking behavior observed in the experiments with the composites. Neglecting the weave immensely reduces the complexity of the finite element analysis without reducing the accuracy of the model. Table 7 summarizes the material property data used in modeling the uncoated composite, and table 8 summarizes the material property data used in modeling the coated composite. The coated composite had a marginally lower modulus and maximum strain for the glass and the resin, but retained a larger percentage of its elastic modulus and ultimate strength with increasing energy exposure across the heating conditions modeled. The maximum glass strain is assumed to be constant

because the glass is assumed to be largely immune to thermal damage, except for the decrease in elastic modulus required to appropriately capture the elastic behavior of the material.

Table 7: Uncoated Composite Layer Model Material Properties Summary

Uncoated (MPa)	Control	25-180	50-40	100-40
Modulus of resin	2450.8	1530.964729	2152.125019	1423.753
Modulus of glass	79640	49749.48221	69934.40366	46265.57
S _{ut} of resin	63.00000011	21.75580503	27.80449308	23.81533
BISO S _y of resin	64.26000012	22.19092113	28.36058294	24.29164
Maximum Adhesive Stress	903.7173116	564.5337558	793.5827632	525
Maximum Resin Strain ($\frac{mm}{mm}$)	0.025705892	0.025705892	0.025705892	0.025705892
Maximum Glass Strain ($\frac{mm}{mm}$)	0.01134753	0.01134753	0.01134753	0.01134753

Table 8: Coated Composite Layer Model Material Properties Summary

Coated (MPa)	Control	25-180	50-40	100-40
Modulus of resin	2313.433172	1993.129677	1604.315182	1208.565
Modulus of glass	68341.99512	58879.78972	47393.67519	35702.66
S _{ut} of resin	51.36316182	29.54668817	26.40096366	18.6004
BISO S _y of resin	52.39042506	30.13762193	26.92898293	18.97241
Maximum Adhesive Stress	775.5128591	668.1401967	537.8011644	405.137
Maximum Resin Strain ($\frac{mm}{mm}$)	0.022202138	0.022202138	0.022202138	0.022202138
Maximum Glass Strain ($\frac{mm}{mm}$)	0.022202138	0.022202138	0.022202138	0.022202138

7.2 Verification

The verification process was continuous throughout the process of modeling. The four forms of verification were matching the elastic, elastic-plastic, and pop-in behavior and strain energy. The first form was achieved with both of the functional models. The second form was essentially ignored as unimportant for the purposes of this model. The plastic behavior of this composite is extremely brief, and nearly irrelevant to forming an accurate model of the composite outside of fatigue applications. The pop-in behavior is the primary behavior of interest, and the most difficult behavior to replicate. The monotonic model only replicated the average value of the pop-in failure. The layer model captured both the shape of the pop-in failure and the magnitude accurately. The complex model failed to produce any

results whatsoever. The monotonic model and the layer model both reproduced the correct strain energy.

Taken together, these results imply that the layer model will be the most accurate for use in the cracking results, and in any application that can assume the deviation of the model from the actual plastic behavior of the composite is insignificant. The complex model can be made the most accurate if more processing power is available, and the geometry is transcribed accurately. Due to the internal complexity of the model, portions of its internal structure did not translate into the IGES model of the composite, and correspondingly did not translate into the finite element model of the composite. If a completely accurate model is to be made, this would be an essential barrier to overcome in the production of that model.

7.3 Cracking

The cracking results are the least verifiable, but offer the most insight into future experimentation with the composite and the model. The only composite that displays signs of cracking is the unheated composite. The experimental sample does not display the origin point of the cracks or the order in which the cracks appear and grow. The monotonic model illustrated crack progression the most clearly, but the results from the layer model are usable and largely verify the results of the monotonic model. Based on the model, it can be seen that the top of the centerline, where the load is applied, is the first origin point for cracks. . The other crack origin point is on bottom-center of the area immediately above the supports. The mild amplification of stress caused by the support force from these cylinders causes new cracks to form at these locations. These cracks later join with the first crack. According to Figures 23-25, the cracks in the model propagate in a plane stress configuration in line with the horizontal and vertical orientation of the composite. It can be seen that the layered structure of the composite introduces stress concentrations on the upper layers under a flexural load. This stress

concentration of the layered design can in combination with other conditions of use, such as contact or moisture, induce local failure. This local failure would then cause a catastrophic failure of the whole composite, which must be avoided. This model is a crucial first step in anticipating those other loads using finite element analysis.

7.4 Future Work

There are three areas of future work that can be explored. The most apparent is the use of a more refined mesh, ideally with more load steps. A more refined mesh would eliminate the need for the bilinear elastic model. A model using more load steps would further reduce the risk of inappropriate overstressing and would provide higher quality cracking results. The more appropriate results for cracking and overstressing would increase the correlation for the ultimate stress equation. The second area for exploration would be exploring the use of element death with the glass fiber elements. The iterative nature of obtaining the exact values of the ultimate stress would make this a time consuming process, but would improve the fit of the model for the cases where the unloading converges to a constant force value. The increased cracking information available would allow submodeling to be conducted within the glass layers to explore the mesoscale interactions that may affect composite behavior. Similarly, the final major area for future exploration would be the use and refinement of the complex model from Chapter 4 that was unusable due to limitations on processor power available. In theory, if this model could be made functional, it should provide exactly correct results in virtually all circumstances.

Appendix A: Command Sets Used

Appendix A.1: Monotonic Model Element Death Commands

See A.3 and A.4 for an explanation.

```
/solution

/INPUT,tokill,CM

ESEL,NONE

ESEL,A,ELEM,,dead

EKILL,ALL

ESEL,ALL

SOLVE

FINISH


/post1

SET, LAST

ETABLE,SEQV,S,EQV

ESEL,S,ETAB,SEQV,18.6

/INPUT,tokill,CM

ESEL,A,ELEM,,dead

ESEL,U,MAT,,2,3

CM,dead,ELEM

CMWRITE,tokill,CM

FINISH


/solu

ANTYPE,,REST

/INPUT,tokill,CM

ESEL,NONE

ESEL,A,ELEM,,dead

EKILL,ALL

ESEL,ALL
```

Appendix A.2: Layer Model

See A.3 and A.4 for an explanation

```
/solution
/INPUT,tokill,CM
CUTCONTROL,PLSLIMIT,1
ESEL,NONE
ESEL,A,ELEM,,dead
EKILL,ALL
ESEL,ALL
SOLVE
FINISH
/post1
SET, LAST
ETABLE,SEQV,S,EQV
ESEL,S,ETAB,SEQV,Sut
/INPUT,tokill,CM
ESEL,A,ELEM,,dead
ESEL,U,MAT,,1,4
ESEL,U,MAT,,10,13
CM,dead,ELEM
CMWRITE,tokill,CM
FINISH
/solu
ANTYPE,,REST
/INPUT,tokill,CM
CUTCONTROL,PLSLIMIT,1
ESEL,NONE
ESEL,A,ELEM,,dead
EKILL,ALL
ESEL,ALL
```

Appendix A.3: Index of Commands Used (With Effects)

ANTYPE: Starts an analysis. Extensions can be used to specify type of analysis and if it is a new analysis or if it is restarting a past analysis.

CM: Defines a component, given a name, and type of component (component of elements, component of nodes, component of volumes, etc.)

CMWRITE: Writes defined components to a file with a chosen name and extension, the default extension being “.CM”.

CUTCONTROL: Defines conditions and properties for automatic bisecting of the time step. Used here with ‘PLSLIMIT’ to increase the maximum strain step from 0.15 (the default) to 1.

EKILL: Can either be used with “,all” or “,P”. “,all” kills all selected elements. “,P” enables the user to choose elements to kill graphically.

ESEL: Used to select elements. Can be used with different selection modes, including “all” and “none”, as well as “S” (clears selection and selects a new set), “A” (selects elements in addition to current set), “U” (unselects elements meeting the criteria that follows), and “INVE” (Inverts current selection). With “S”, “A”, and “U” additional criteria can be used relating to the material, element table results (see ETABLE), among other criteria.

ETABLE: Creates a table of values at the current time step for the element data chosen. Commands can also be used to empty, update, display, or refresh the contents of a given element table. Element table data can be directional stress, equivalent stress, directional strain, equivalent strain, failure criteria, and many others.

FINISH: Exits the current environment and ends processing without completing the solution run.

/INPUT: Reads input from a given compatible ANSYS input file, in the working directory or along a given filepath, with the given name and extension. Can be nested within input files (meaning, the file being

read can contain an /input command as well, referring to a third, distinct file) up to ten layers at a time in the default ANSYS environment.

/POST1: Enters the postprocessing environment, enabling postprocessing commands and logic, allowing for the analysis and calculation of requested results.

/SOLUTION: Enters solution environment, allowing the ANSYS solver engine to receive commands and solve the current time step for a given set of results.

SET: Loads a given set of results. Can load a specific time value, load step, or substep. Used here with “,LAST” to load the most recent set of data.

SOLVE: Instructs ANSYS to solve the model at the current time step, producing a new set of results.

Appendix A.4: Command Logic Explanation

The logic used is the same in both cases. The first act is to import the component ("dead") from the component file written in previous steps ("tokill.cm"). The maximum strain step is then changed from 0.15 to 1, to eliminate issues that can arise from inappropriate bisection controls. Just these elements are then selected (by clearing the selection and selecting the elements comprising the component. If the component file is empty, ANSYS ignores the selection command by default and there are no elements selected when the EKILL command is executed. The full set of elements is then reselected and the solution is executed. The solution environment is then exited and the solution run enters into postprocessing. The solution run loads the most recent set of data, and then forms an element table based on the equivalent Von-Mises stress, and any element with a stress value above S_{ut} is selected. The file "tokill.cm" is loaded, and the component "dead" is also selected. The non-resin elements are then unselected. This provides additional insurance against accidental inclusion of non-resin elements in the component "dead". The component "dead" is then redefined to include all selected elements (all previously killed elements plus any new elements killed in this load step), and the file "tokill.cm" is overwritten with the new definition of the component. The postprocessing is finished, and the solution environment is reentered, where the component "dead" is input from the new "tokill.cm", and just the component "dead" is selected. The elements of component "dead" are killed, and then the full set of elements is reselected.

Appendix B: Full Data Set

Appendix B.1: Force Driven Monotonic Data

Force (N)	Theoretical (mm)	Monotonic Model (mm)	Ekill Tuned (mm)	Bilinear Monotonic (mm)	Bilinear Ekill (mm)
0	0	0	0	0	0
49.4	-0.4	-0.42201	-0.42126	-0.42173	-0.42173
101.5	-0.8	-0.86539	-0.85584	-0.8665	-0.85728
154	-1.2	-1.3139	-1.2999	-1.3147	-1.3007
200.5	-1.6	-1.7114	-1.6927	-1.7117	-1.6934
247	-2	-2.1083	-2.0851	-2.1086	-2.0862
293	-2.4	-2.5012	-2.4739	-2.5013	-2.4747
336	-2.8	-2.868	-2.8371	-2.8684	-2.8379
382	-3.2	-3.2603	-3.2256	-3.2611	-3.2264
426	-3.6	-3.6363	-3.5973	-3.6368	-3.5981
471	-4	-4.02	-3.9772	-4.0209	-3.9781
515	-4.4	-4.3959	-4.3491	-4.3978	-4.3542
558	-4.8	-4.7631	-4.7128	-4.7745	-4.7354
600	-5.2	-5.1216	-5.0673	-5.1574	-5.1239
642	-5.6	-5.4803	-5.4224	-5.5545	-5.5249
682	-6	-5.8219	-5.7602	-5.9456	-5.9253
720	-6.4	-6.1459	-6.0814	-6.3343	-6.3484
758	-6.8	-6.4708	-6.4027	-6.7784	-6.8796
796	-7.2	-6.7955	-6.7237	-7.337	-7.5686
828	-7.6	-7.0682	-6.994	-7.9223	-8.3398
744	-8	-6.3524	-8.6216	-7.2053	-7.6304
660	-8.4	-5.6345	-7.6464	-6.4882	-6.9209
576	-8.8	-4.9182	-6.6731	-5.7711	-6.2115

Appendix B.2: Force Driven Layer Data

Force (N)	Theoretical (mm)	Layer Model (mm)	Bilinear Layer Model (mm)	Ekill Layer Model (mm)
0	0	0	0	0
49.4	-0.4	-0.45249	-0.45244	-0.4228
101.5	-0.8	-0.94886	-0.94881	-0.99155
154	-1.2	-1.4359	-1.4358	-1.5005
200.5	-1.6	-1.8643	-1.8642	-1.9481
247	-2	-2.3136	-2.3135	-2.4176
293	-2.4	-2.7286	-2.7286	-2.8512
336	-2.8	-3.1427	-3.1426	-3.2838
382	-3.2	-3.5699	-3.5698	-3.7301
426	-3.6	-3.9839	-3.9839	-4.1627
471	-4	-4.4017	-4.4017	-4.5991
515	-4.4	-4.8139	-4.8139	-5.0296
558	-4.8	-5.2168	-5.2167	-5.4504
600	-5.2	-5.6102	-5.6102	-5.8614
642	-5.6	-6.0009	-6.0139	-6.2694
682	-6	-6.3747	-6.4368	-6.6598
720	-6.4	-6.7299	-6.852	-7.0307
758	-6.8	-7.085	-7.2682	-7.4015
796	-7.2	-7.4402	-7.7038	-7.7724
828	-7.6	-7.7392	-8.082	-8.0846
744	-8	-6.9539	-7.297	-7.2644
660	-8.4	-6.1689	-6.5119	-6.4446
576	-8.8	-5.3838	-5.7268	-5.6247

Appendix B.3: Displacement Driven Monotonic Model

Appendix B.4: Displacement Layer Model Data

Appendix B.5: Uncoated Model Data

Heat Flux, Exposure Time $(\frac{kW}{m^2}, \text{sec})$	Normalized Modulus	Total Factor
0, 0	1	1
Deflection (mm)	Experimental (N)	Model (N)
0	0	0
0.4	49.4	46.036
0.8	101.5	92.072
1.2	154	138.104
1.6	200.5	184.14
2	247	230.18
2.4	293	276.216
2.8	336	322.252
3.2	382	368.288
3.6	426	414.32
4	471	460.36
4.4	515	506.4
4.8	558	552.4
5.2	600	596.76
5.6	642	641.08
6	682	685.4
6.4	720	729.64
6.8	758	773.84
7.2	796	818.04
7.6	828	862.04
8	744	528.56
8.4	660	549.24
8.8	576	410.04

Heat Flux, Exposure Time $(\frac{kW}{m^2}, \text{sec})$	Normalized Modulus	Total Factor
25,180	0.622108888	0.624679586
Deflection (mm)	Experimental (N)	Model (N)
0	0	0
0.4	29.547	28.7572
0.8	60.476	57.516
1.2	91.696	86.272
1.6	122.385	115.028
2	152.652	143.32
2.4	181.755	170.984
2.8	210.823	198.596
3.2	221.19	225.468
3.6	229.54	250.824
4	247.133	271.668
4.4	261.148	291.364
4.8	273.066	309.708
5.2	240.405	192.268
5.6	216.024	205.068
6	217.162	217.84
6.4	181.328	230.588
6.8	179.441	243.224
7.2	177.94	191.176
7.6	177.546	207.216
8	175.996	233.236
8.4	175.712	258.204

Heat Flux, Exposure Time $(\frac{kW}{m^2}, \text{sec})$	Normalized Modulus	Total Factor
50,40	0.550176515	0.878131638
Deflection (mm)	Experimental (N)	Model (N)
0	0	0
0.4	42.005	40.424
0.8	85.592	80.848
1.2	127.72	121.276
1.6	170.395	161.7
2	211.74	200.76
2.4	253.882	239.6
2.8	296.324	277.72
3.2	337.866	314.148
3.6	379.783	343.516
4	420.019	371.144
4.4	459.316	396.348
4.8	440.047	248.34

Heat Flux, Exposure Time $(\frac{kW}{m^2}, \text{sec})$	Normalized Modulus	Total Factor
100,40	0.315087644	0.580934
Deflection (mm)	Experimental (N)	Model (N)
0	0	0
0.4	29.201	26.7432
0.8	61.999	53.488
1.2	93.341	80.232
1.6	124.233	106.976
2	154.729	133.72
2.4	183.475	159.752
2.8	211.916	185.472
3.2	235.849	211.152
3.6	251.46	236.268
4	270.325	261.056
4.4	280.227	281.596
4.8	294.392	300.404
5.2	307.197	318.524
5.6	310.273	335.1
6	256.875	206.256
6.4	245.474	218.176
6.8	247.601	230.064
7.2	230.421	241.932
7.6	229.322	189.376
8	226.45	213.76
8.4	221.422	237.716
8.8	219.027	260.096
9.2	215.51	278.064
9.6	214.086	293.548
10	213.672	307.14
10.4	208.291	318.2
10.8	207.025	317.312
11.2	210.016	326.312

11.6	212.275	334.228
------	---------	---------

Appendix B.6: Coated Model Data

Heat Flux, Exposure Time	Normalized Modulus	Total Ratio
0, 0	0.909090909	0.943950209
Deflection (mm)	Experimental Reaction Force (N)	Model Reaction Force (N)
0	0	0
0.4	50.54	40.64
0.8	98.877	81.28
1.2	143.112	121.924
1.6	186.241	162.564
2	225.717	203.208
2.4	263.728	243.848
2.8	282.401	284.492
3.2	317.121	324.176
3.6	336.297	363.284
4	369.39	402.36
4.4	390.067	441.36
4.8	420.742	479.76
5.2	449.189	517.4
5.6	477.094	552.96
6	504.364	584.08
6.4	530.791	608.68
6.8	556.726	631.2
7.2	577.223	652.44
7.6	595.289	673.12
8	616.337	691.24
8.4	632.97	706.68
8.8	587.842	485.56
9.2	565.893	411.56
9.6	563.207	446.56

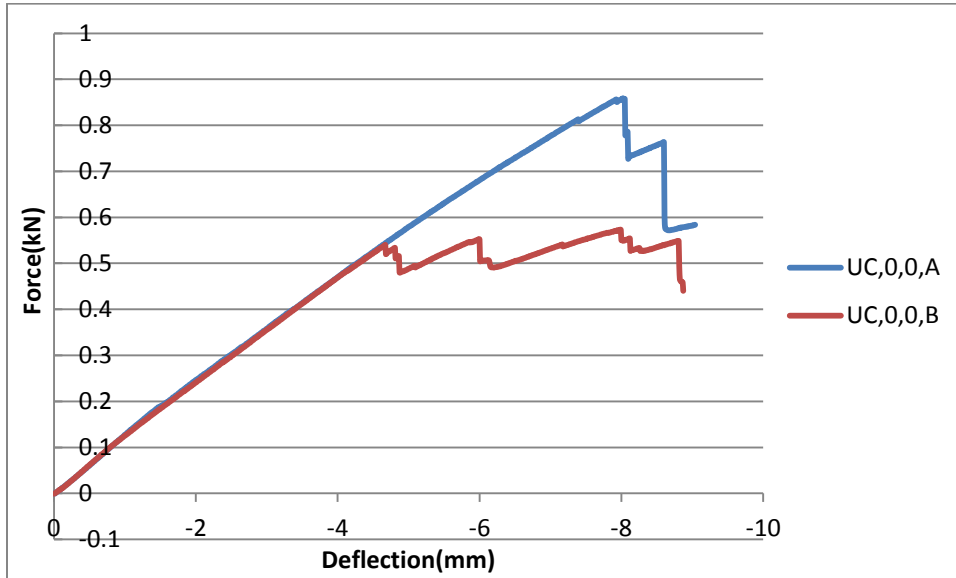
Heat Flux, Exposure Time	Normalized Modulus	Total Factor
25,180	0.745944853	0.813256764
Deflection (mm)	Experimental (N)	Model (N)
0	0	0
0.4	47.697	35.014
0.8	91.528	70.028
1.2	127.171	105.044
1.6	161.817	140.056
2	190.352	175.06
2.4	215.438	208.772
2.8	239.085	242.42
3.2	269.82	275.852
3.6	295.381	308.276
4	321.082	340.348
4.4	346.874	366.904
4.8	371.977	391.18
5.2	389.117	414.32
5.6	403.127	435
6	424.23	454.28
6.4	417.726	280.268
6.8	240.743	295.792

Heat Flux, Exposure Time	Normalized Modulus	Total Factor
50,40	0.440295103	0.654608773
Deflection (mm)	Experimental (N)	Model (N)
0	0	0
0.4	48.931	28.1836
0.8	94.917	56.368
1.2	137.032	84.552
1.6	173.507	112.736
2	186.847	140.92
2.4	214.007	168.452
2.8	237.096	195.556
3.2	243.112	222.62
3.6	268.251	249.14
4	290.169	275.216
4.4	311.35	300.124
4.8	327.009	321.02
5.2	348.151	340.464
5.6	368.233	358.608
6	379.332	374.788
6.4	396.077	388.356
6.8	381.784	237.676

Heat Flux, Exposure Time	Normalized Modulus	Total Factor
100,40	0.26769775	0.493131
Deflection (mm)	Experimental (N)	Model (N)
0	0	0
0.4	29.9	21.2312
0.8	62.015	42.464
1.2	87.812	63.696
1.6	110.963	84.928
2	134.926	106.16
2.4	157.982	126.68
2.8	180.992	147.088
3.2	201.568	167.46
3.6	221.361	187.144
4	236.651	206.648
4.4	245.454	223.656
4.8	258.527	238.588
5.2	269.646	252.912
5.6	274.309	265.668
6	276.749	277.496
6.4	190.867	170.572
6.8	170.926	179.98
7.2	168.561	189.336
7.6	168.2	148.14
8	164.294	167.66
8.4	162.681	187.176
8.8	163.204	205.268

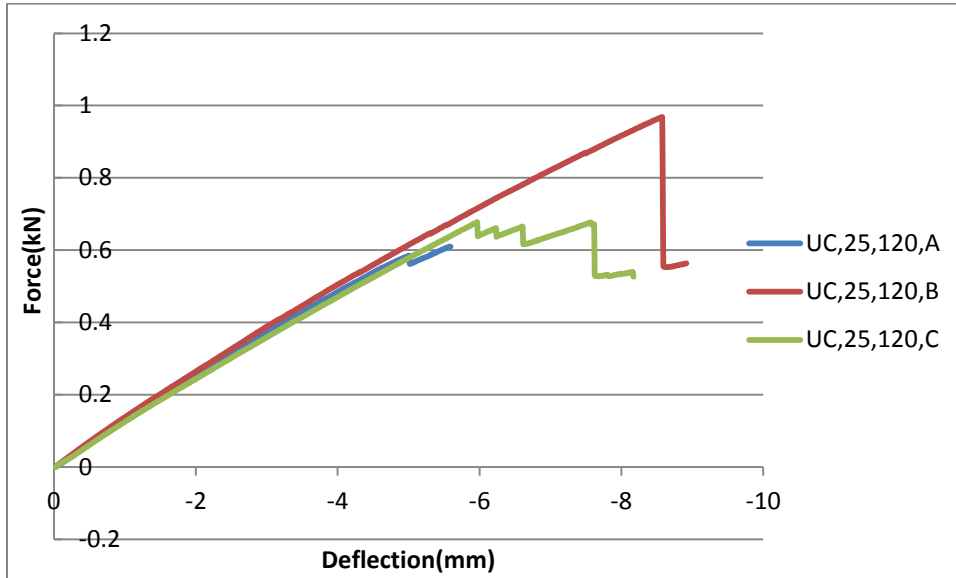
Appendix C: Specimens That Were Tested

Appendix C.1: Uncoated, $\phi=0$, $t_{\text{exp}}=0$



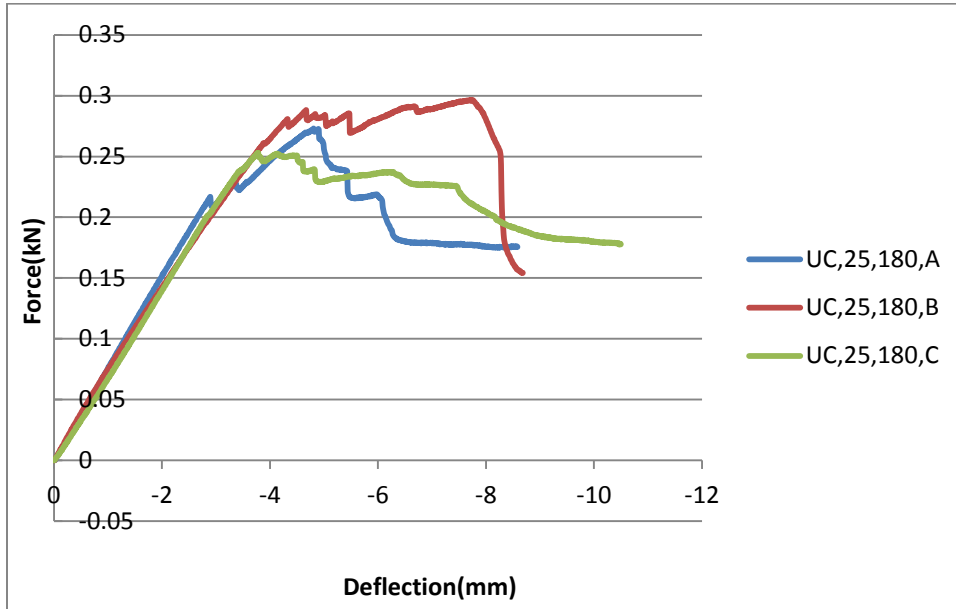
Uncoated	0, 0
Normalized Modulus ($\frac{E}{E_0}$)	1
Model Modulus Ratio ($\frac{E_m}{E_0}$)	1
Overall Stiffness (MPa) (E_m)	23280
Resin Stiffness (MPa) (E_{resin})	2228
Glass Stiffness (MPa) (E_{glass})	72400
Resin Ultimate Strength (MPa) (S_{ut})	63
Glass Yield Strength (MPa) ($S_{y,\text{glass}}$)	821.5612
Rupture Strain (ϵ_{ut})	0.028276

Appendix C.2: Uncoated, $\phi=25$, $t_{exp}=120$



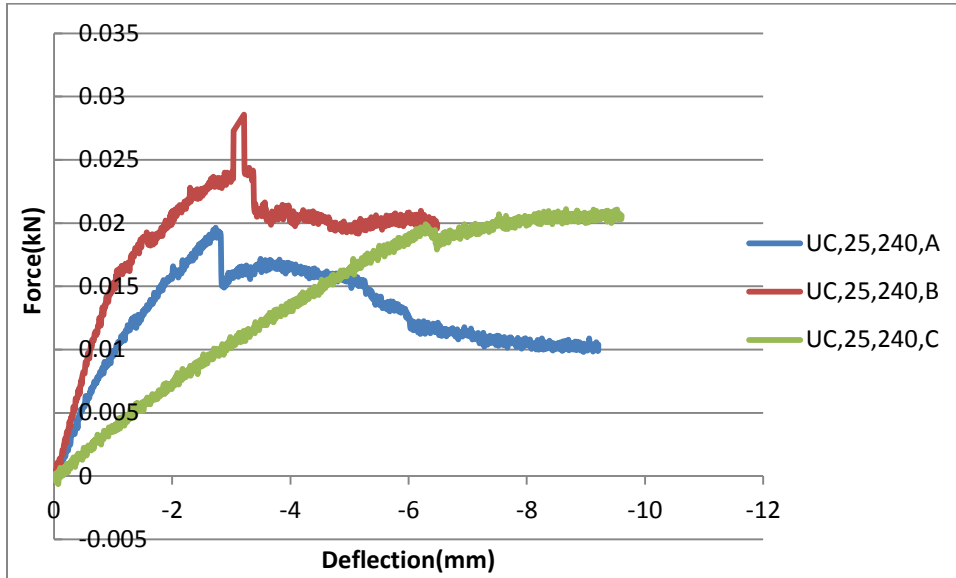
Uncoated	25, 120
Normalized Modulus ($\frac{E}{E_0}$)	0.929193
Model Modulus Ratio ($\frac{E_m}{E_0}$)	1.004774
Overall Stiffness (MPa) (E_m)	21631.62
Resin Stiffness (MPa) (E_{resin})	2070.242
Glass Stiffness (MPa) (E_{glass})	67273.58
Resin Ultimate Strength (MPa) (S_{ut})	54.39419
Glass Yield Strength (MPa) ($S_{y,glass}$)	763.389
Rupture Strain (ϵ_{ut})	0.026274

Appendix C.3: Uncoated, $\phi=25$, $t_{exp}=180$



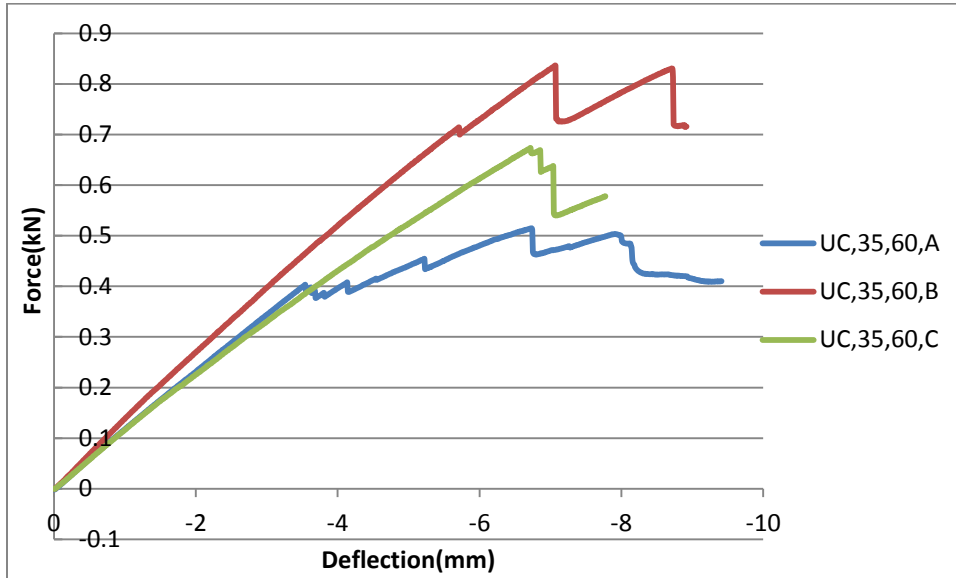
Uncoated	25, 180
Normalized Modulus ($\frac{E}{E_0}$)	0.622109
Model Modulus Ratio ($\frac{E_m}{E_0}$)	0.62468
Overall Stiffness (MPa) (E_m)	14482.69
Resin Stiffness (MPa) (E_{resin})	1386.059
Glass Stiffness (MPa) (E_{glass})	45040.68
Resin Ultimate Strength (MPa) (S_{ut})	24.38223
Glass Yield Strength (MPa) ($S_{y,glass}$)	511.1005
Rupture Strain (ϵ_{ut})	0.017591

Appendix C.4: Uncoated, $\phi=25$, $t_{exp}=240$



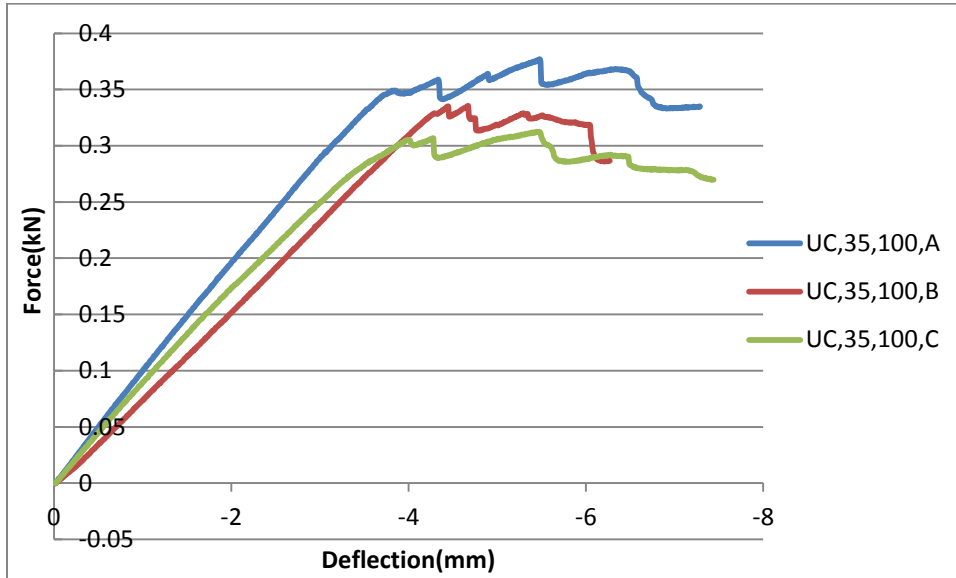
Uncoated	25, 240
Normalized Modulus ($\frac{E}{E_0}$)	0.149039
Model Modulus Ratio ($\frac{E_m}{E_0}$)	0.13253
Overall Stiffness (MPa) (E_m)	3469.632
Resin Stiffness (MPa) (E_{resin})	332.0592
Glass Stiffness (MPa) (E_{glass})	10790.44
Resin Ultimate Strength (MPa) (S_{ut})	1.399398
Glass Yield Strength (MPa) ($S_{y,glass}$)	122.4448
Rupture Strain (ϵ_{ut})	0.004214

Appendix C.5: Uncoated, $\phi=35$, $t_{exp}=60$



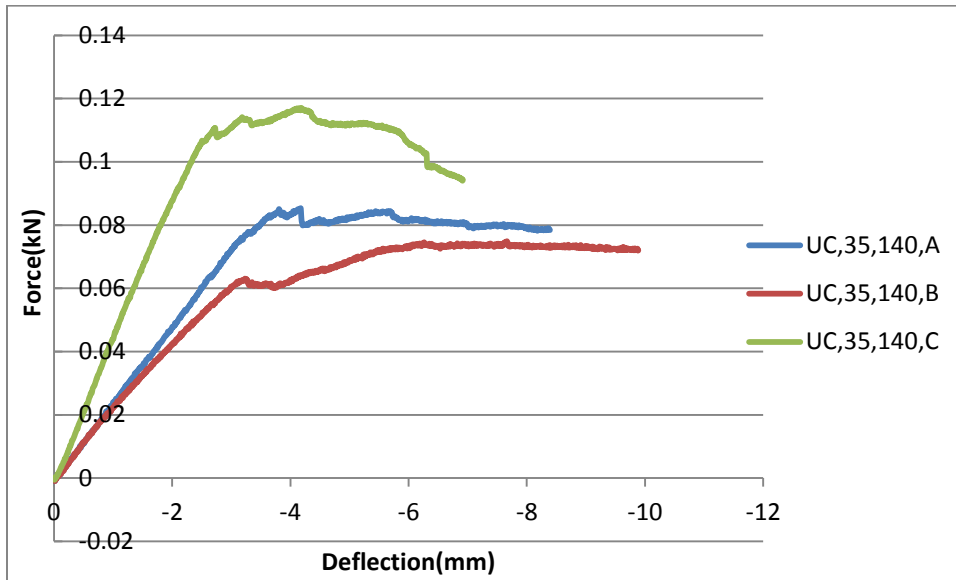
Uncoated	35, 60
Normalized Modulus ($\frac{E}{E_0}$)	0.591462
Model Modulus Ratio ($\frac{E_m}{E_0}$)	1.038063
Overall Stiffness (MPa) (E_m)	13769.24
Resin Stiffness (MPa) (E_{resin})	1317.778
Glass Stiffness (MPa) (E_{glass})	42821.86
Resin Ultimate Strength (MPa) (S_{ut})	22.03913
Glass Yield Strength (MPa) ($S_{y,glass}$)	485.9224
Rupture Strain (ϵ_{ut})	0.016724

Appendix C.6: Uncoated, $\phi=35$, $t_{exp}=100$



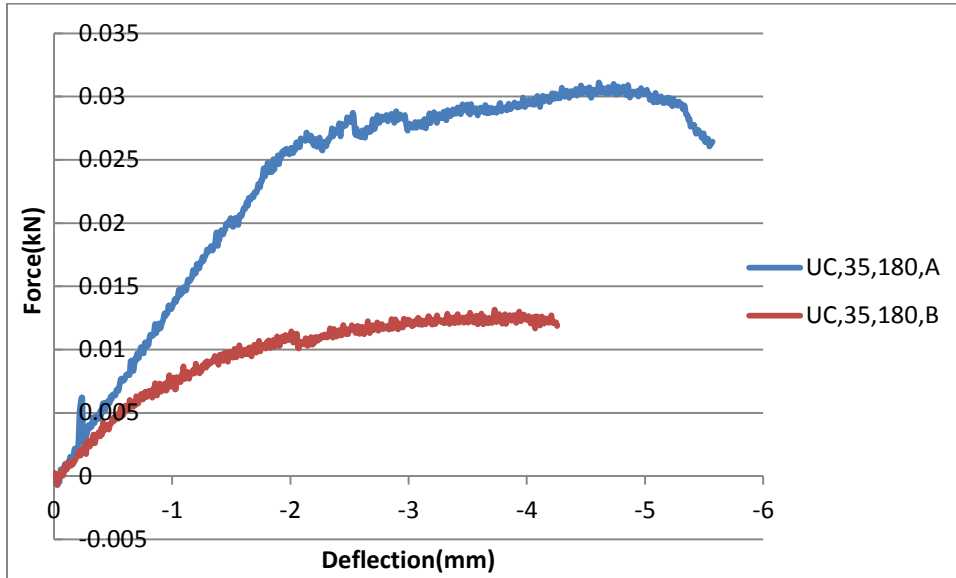
Uncoated	35, 100
Normalized Modulus ($\frac{E}{E_0}$)	0.421463
Model Modulus Ratio ($\frac{E_m}{E_0}$)	0.739701
Overall Stiffness (MPa) (E_m)	9811.661
Resin Stiffness (MPa) (E_{resin})	939.0198
Glass Stiffness (MPa) (E_{glass})	30513.93
Resin Ultimate Strength (MPa) (S_{ut})	11.19076
Glass Yield Strength (MPa) ($S_{y,glass}$)	346.2577
Rupture Strain (ϵ_{ut})	0.011917

Appendix C.7: Uncoated, $\phi=35$, $t_{exp}=140$



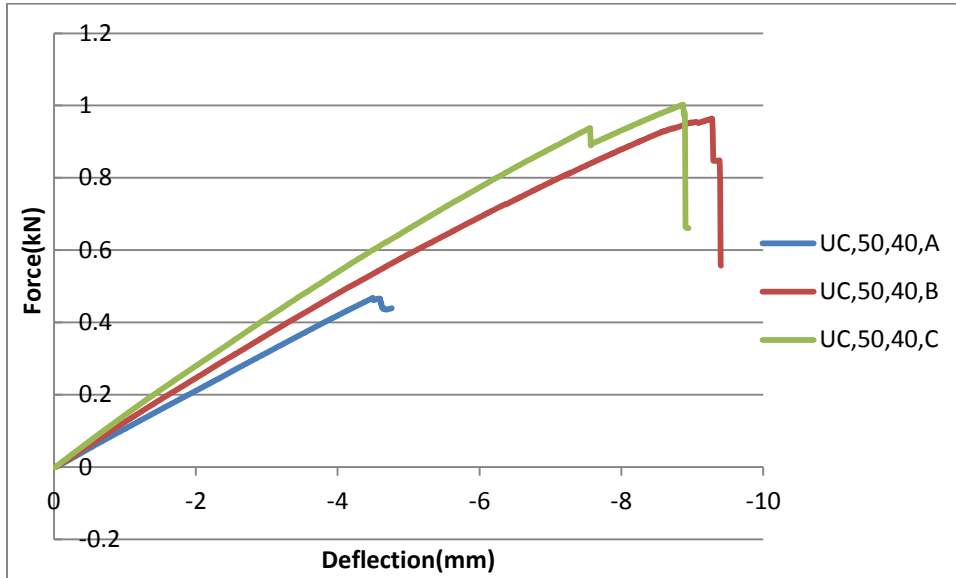
Uncoated	35, 140
Normalized Modulus ($\frac{E}{E_0}$)	0.152013
Model Modulus Ratio ($\frac{E_m}{E_0}$)	0.255027
Overall Stiffness (MPa) (E_m)	3538.867
Resin Stiffness (MPa) (E_{resin})	338.6854
Glass Stiffness (MPa) (E_{glass})	11005.76
Resin Ultimate Strength (MPa) (S_{ut})	1.455805
Glass Yield Strength (MPa) ($S_{y,glass}$)	124.8881
Rupture Strain (ϵ_{ut})	0.004298

Appendix C.8: Uncoated, $\phi=35$, $t_{exp}=180$



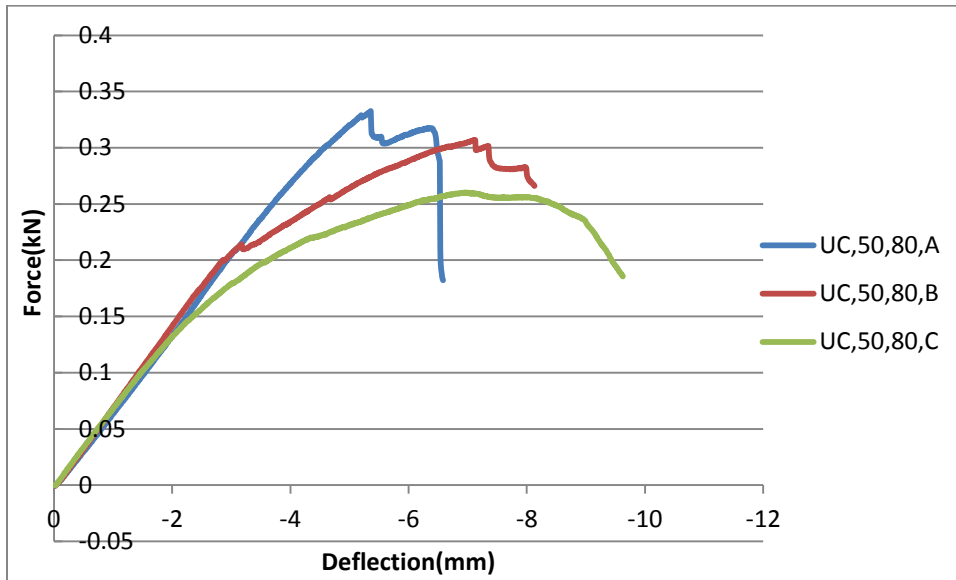
Uncoated	35, 180
Normalized Modulus ($\frac{E}{E_0}$)	0.092944
Model Modulus Ratio ($\frac{E_m}{E_0}$)	0.149668
Overall Stiffness (MPa) (E_m)	2163.728
Resin Stiffness (MPa) (E_{resin})	207.0784
Glass Stiffness (MPa) (E_{glass})	6729.12
Resin Ultimate Strength (MPa) (S_{ut})	0.544227
Glass Yield Strength (MPa) ($S_{y,glass}$)	76.35889
Rupture Strain (ϵ_{ut})	0.002628

Appendix C.9: Uncoated, $\phi=50$, $t_{exp}=40$



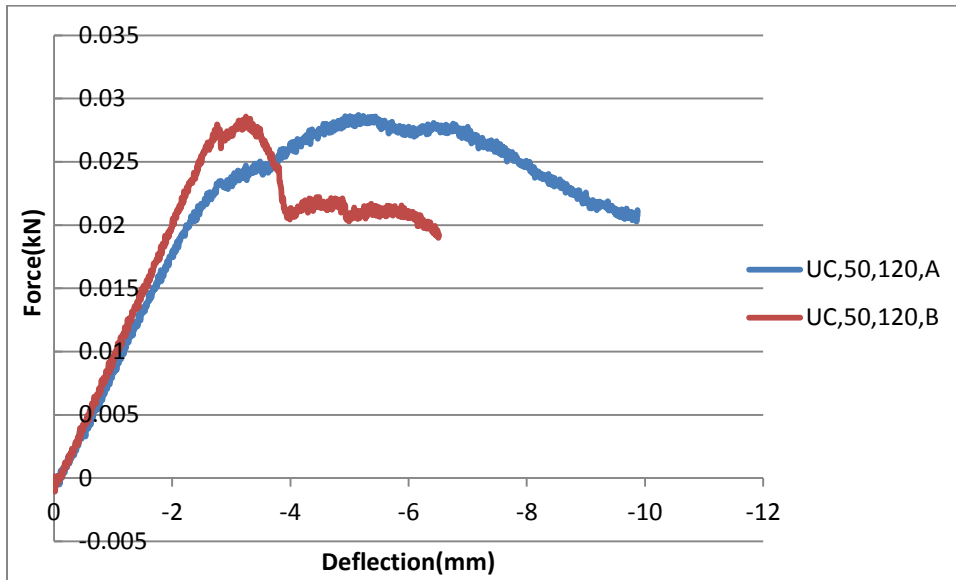
Uncoated	50, 40
Normalized Modulus ($\frac{E}{E_0}$)	0.550177
Model Modulus Ratio ($\frac{E_m}{E_0}$)	0.878132
Overall Stiffness (MPa) (E_m)	12808.11
Resin Stiffness (MPa) (E_{resin})	1225.793
Glass Stiffness (MPa) (E_{glass})	39832.78
Resin Ultimate Strength (MPa) (S_{ut})	19.06973
Glass Yield Strength (MPa) ($S_{y,glass}$)	452.0037
Rupture Strain (ϵ_{ut})	0.015557

Appendix C.10: Uncoated, $\phi=50$, $t_{exp}=80$



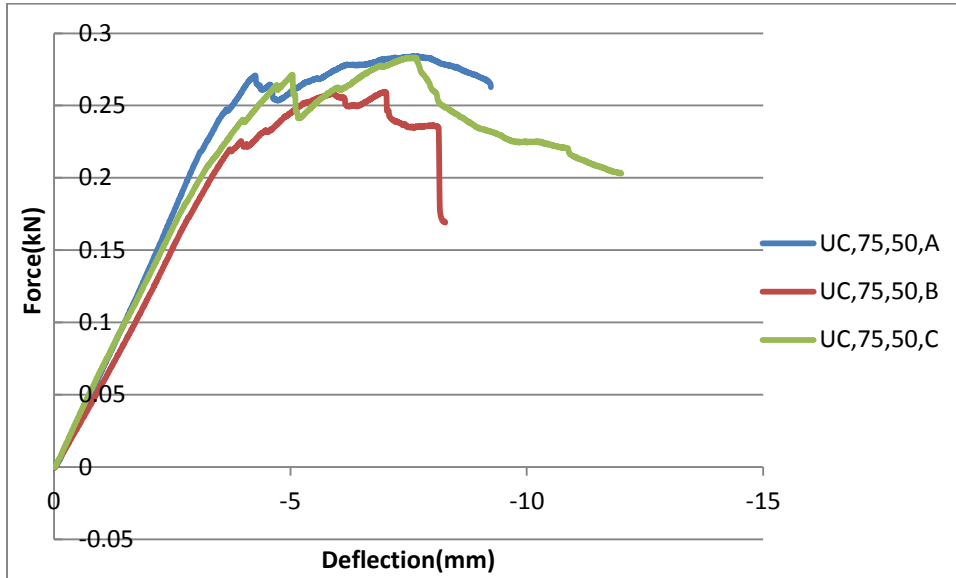
Uncoated	50, 80
Normalized Modulus ($\frac{E}{E_0}$)	0.279197
Model Modulus Ratio ($\frac{E_m}{E_0}$)	0.514349
Overall Stiffness (MPa) (E_m)	6499.717
Resin Stiffness (MPa) (E_{resin})	622.0519
Glass Stiffness (MPa) (E_{glass})	20213.9
Resin Ultimate Strength (MPa) (S_{ut})	4.910927
Glass Yield Strength (MPa) ($S_{y,glass}$)	229.3778
Rupture Strain (ϵ_{ut})	0.007895

Appendix C.11: Uncoated, $\phi=50$, $t_{exp}=120$



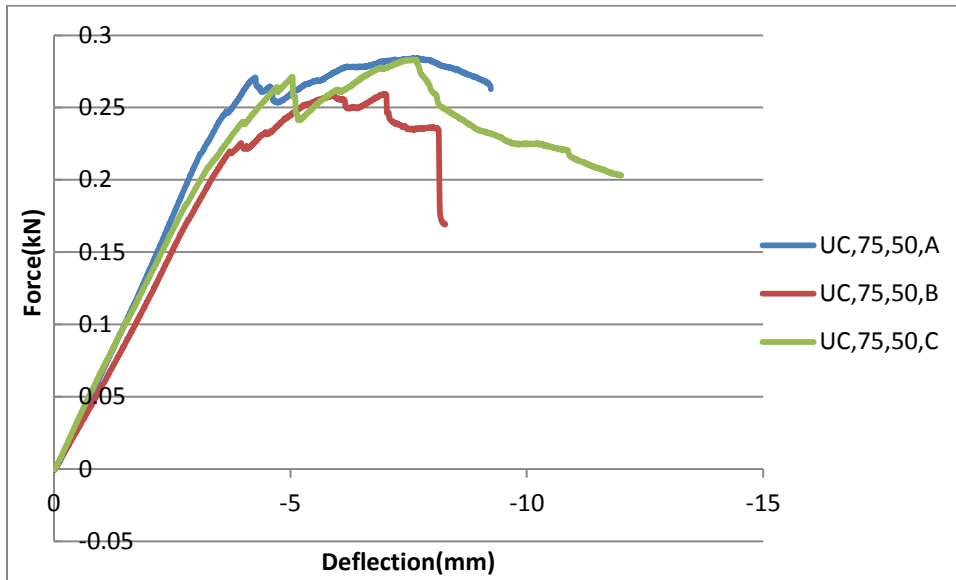
Uncoated	50, 120
Normalized Modulus ($\frac{E}{E_0}$)	0.038443
Model Modulus Ratio ($\frac{E_m}{E_0}$)	0.05598
Overall Stiffness (MPa) (E_m)	894.957
Resin Stiffness (MPa) (E_{resin})	85.65139
Glass Stiffness (MPa) (E_{glass})	2783.286
Resin Ultimate Strength (MPa) (S_{ut})	0.093106
Glass Yield Strength (MPa) ($S_{y,glass}$)	31.58342
Rupture Strain (ϵ_{ut})	0.001087

Appendix C.12: Uncoated, $\phi=75$, $t_{exp}=20$



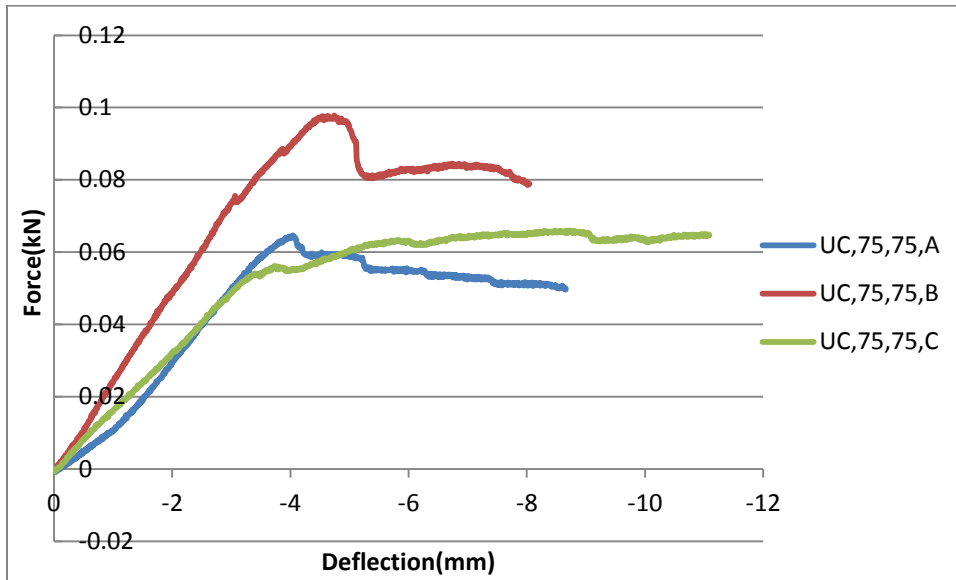
Uncoated	75, 20
Normalized Modulus ($\frac{E}{E_0}$)	0.571331
Model Modulus Ratio ($\frac{E_m}{E_0}$)	0.959272
Overall Stiffness (MPa) (E_m)	13300.58
Resin Stiffness (MPa) (E_{resin})	1272.925
Glass Stiffness (MPa) (E_{glass})	41364.34
Resin Ultimate Strength (MPa) (S_{ut})	20.56438
Glass Yield Strength (MPa) ($S_{y,glass}$)	469.3831
Rupture Strain (ϵ_{ut})	0.016155

Appendix C.13: Uncoated, $\phi=75$, $t_{exp}=50$



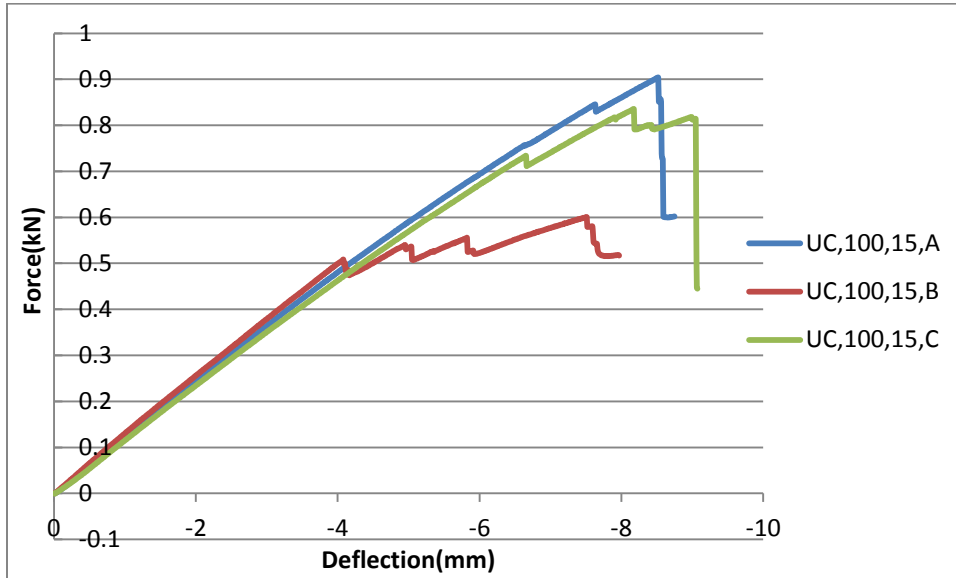
Uncoated	75, 50
Normalized Modulus ($\frac{E}{E_0}$)	0.323397
Model Modulus Ratio ($\frac{E_m}{E_0}$)	0.61488
Overall Stiffness (MPa) (E_m)	7528.693
Resin Stiffness (MPa) (E_{resin})	720.5296
Glass Stiffness (MPa) (E_{glass})	23413.98
Resin Ultimate Strength (MPa) (S_{ut})	6.588913
Glass Yield Strength (MPa) ($S_{y,glass}$)	265.6908
Rupture Strain (ϵ_{ut})	0.009145

Appendix C.14: Uncoated, $\phi=75$, $t_{exp}=75$



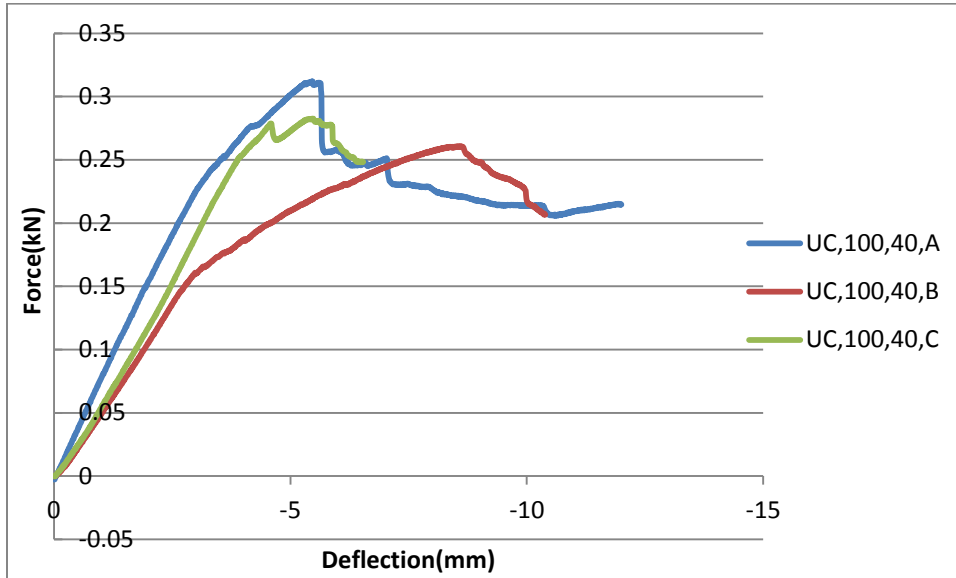
Uncoated	75, 75
Normalized Modulus ($\frac{E}{E_0}$)	0.116169
Model Modulus Ratio ($\frac{E_m}{E_0}$)	0.185791
Overall Stiffness (MPa) (E_m)	2704.41
Resin Stiffness (MPa) (E_{resin})	258.8241
Glass Stiffness (MPa) (E_{glass})	8410.622
Resin Ultimate Strength (MPa) (S_{ut})	0.850197
Glass Yield Strength (MPa) ($S_{y,glass}$)	95.43979
Rupture Strain (ϵ_{ut})	0.003285

Appendix C.15: Uncoated, $\phi=100$, $t_{exp}=15$



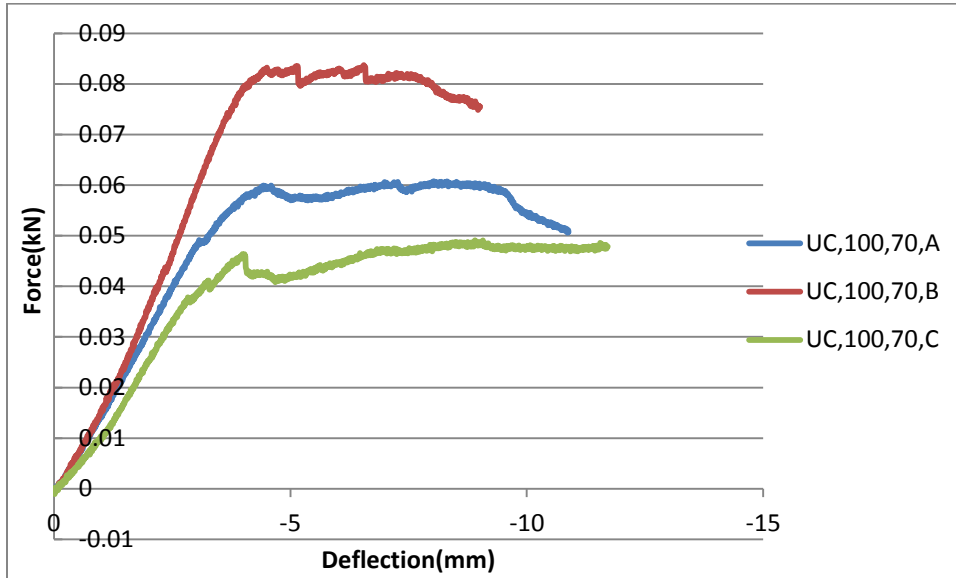
Uncoated	100, 15
Normalized Modulus ($\frac{E}{E_0}$)	0.560218
Model Modulus Ratio ($\frac{E_m}{E_0}$)	1.039935
Overall Stiffness (MPa) (E_m)	13041.87
Resin Stiffness (MPa) (E_{resin})	1248.165
Glass Stiffness (MPa) (E_{glass})	40559.76
Resin Ultimate Strength (MPa) (S_{ut})	19.77216
Glass Yield Strength (MPa) ($S_{y,glass}$)	460.2531
Rupture Strain (ϵ_{ut})	0.015841

Appendix C.16: Uncoated, $\phi=100$, $t_{exp}=40$



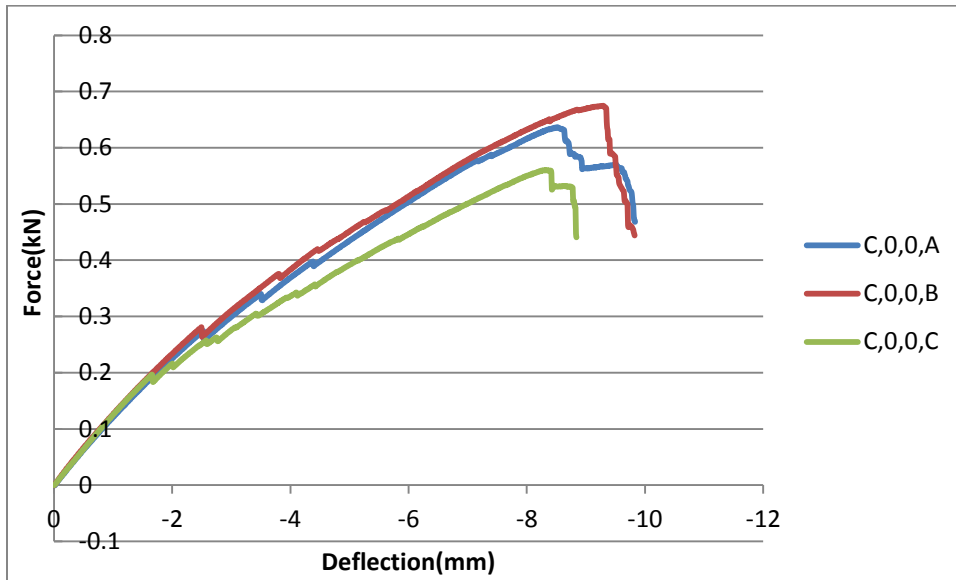
Uncoated	100, 40
Normalized Modulus ($\frac{E}{E_0}$)	0.315088
Model Modulus Ratio ($\frac{E_m}{E_0}$)	0.580934
Overall Stiffness (MPa) (E_m)	7335.24
Resin Stiffness (MPa) (E_{resin})	702.0153
Glass Stiffness (MPa) (E_{glass})	22812.35
Resin Ultimate Strength (MPa) (S_{ut})	6.254654
Glass Yield Strength (MPa) ($S_{y,glass}$)	258.8638
Rupture Strain (ϵ_{ut})	0.00891

Appendix C.17: Uncoated, $\phi=100$, $t_{exp}=70$



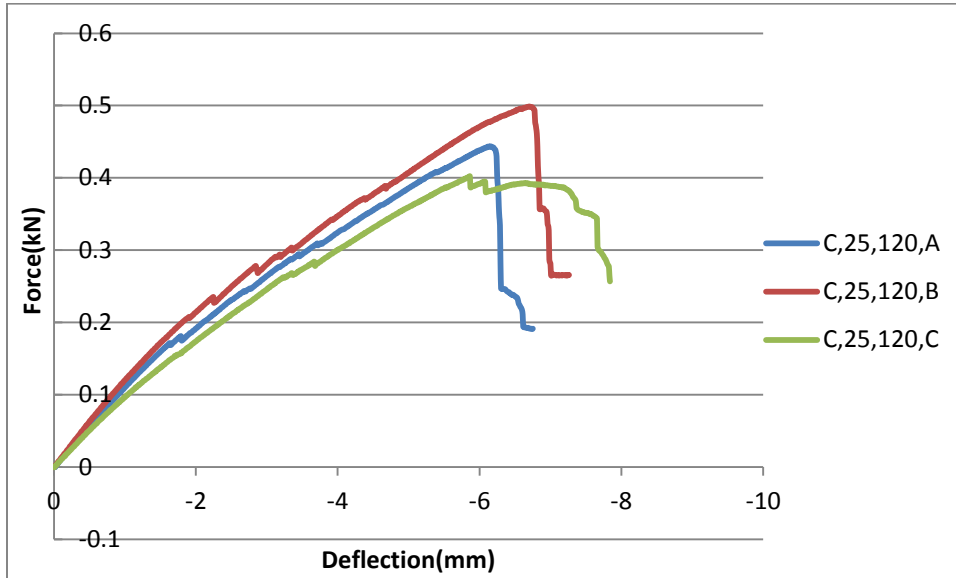
Uncoated	100, 70
Normalized Modulus ($\frac{E}{E_0}$)	0.058487
Model Modulus Ratio ($\frac{E_m}{E_0}$)	0.098121
Overall Stiffness (MPa) (E_m)	1361.572
Resin Stiffness (MPa) (E_{resin})	130.3086
Glass Stiffness (MPa) (E_{glass})	4234.443
Resin Ultimate Strength (MPa) (S_{ut})	0.215504
Glass Yield Strength (MPa) ($S_{y,glass}$)	48.05047
Rupture Strain (ϵ_{ut})	0.001654

Appendix C.18: Coated, $\phi=0$, $t_{exp}=0$



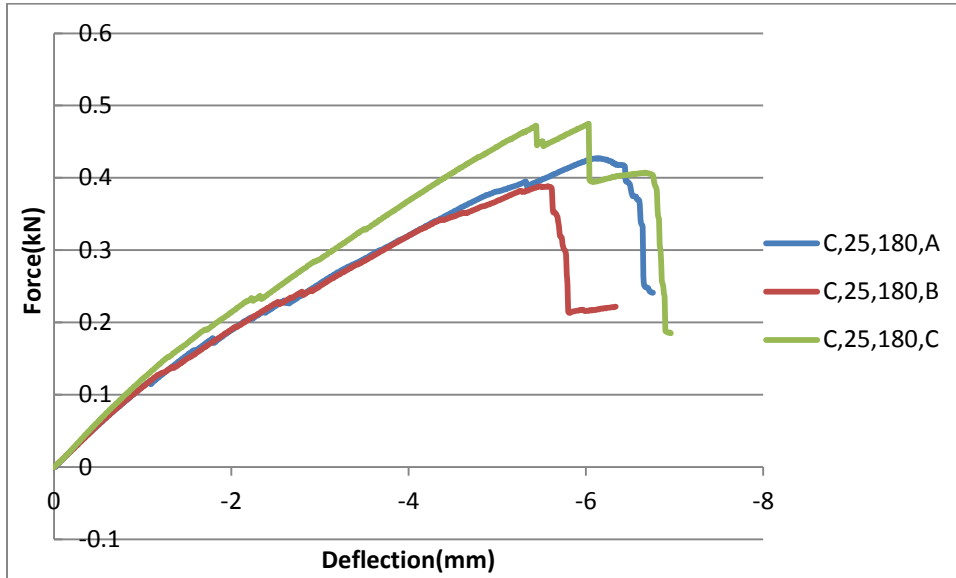
Coated	0, 0
Normalized Modulus ($\frac{E}{E_0}$)	1
Model Modulus Ratio ($\frac{E_m}{E_0}$)	1.038345
Overall Stiffness (MPa) (E_m)	19500
Resin Stiffness (MPa) (E_{resin})	2313
Glass Stiffness (MPa) (E_{glass})	68342
Resin Ultimate Strength (MPa) (S_{ut})	51.36
Glass Yield Strength (MPa) ($S_{y,glass}$)	775.5129
Rupture Strain (ϵ_{ut})	0.022205

Appendix C.19: Coated, $\phi=25$, $t_{exp}=120$



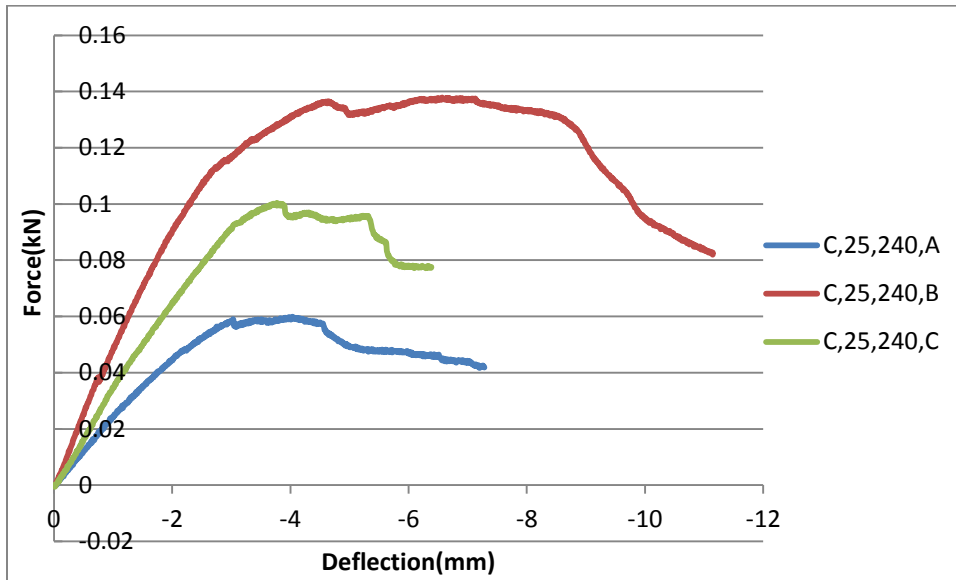
Coated	25, 120
Normalized Modulus ($\frac{E}{E_0}$)	0.948277004
Model Modulus Ratio ($\frac{E_m}{E_0}$)	0.846976072
Overall Stiffness (MPa) (E_m)	19717.60295
Resin Stiffness (MPa) (E_{resin})	2193.364711
Glass Stiffness (MPa) (E_{glass})	64807.14239
Resin Ultimate Strength (MPa) (S_{ut})	46.18441564
Glass Yield Strength (MPa) ($S_{y,glass}$)	735.4010107
Rupture Strain (ϵ_{ut})	0.021056423

Appendix C.20: Coated, $\phi=25$, $t_{exp}=180$



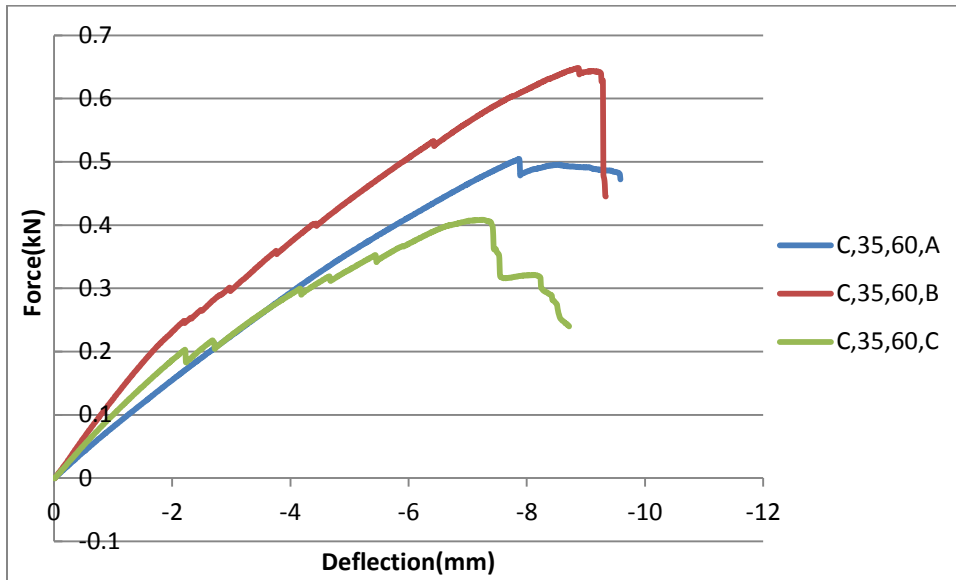
Coated	25, 180
Normalized Modulus ($\frac{E}{E_0}$)	0.820539
Model Modulus Ratio ($\frac{E_m}{E_0}$)	0.894582
Overall Stiffness (MPa) (E_m)	20825.88
Resin Stiffness (MPa) (E_{resin})	1897.907
Glass Stiffness (MPa) (E_{glass})	56077.3
Resin Ultimate Strength (MPa) (S_{ut})	34.57991
Glass Yield Strength (MPa) ($S_{y,glass}$)	636.3388
Rupture Strain (ϵ_{ut})	0.01822

Appendix C.21: Coated, $\phi=25$, $t_{exp}=240$



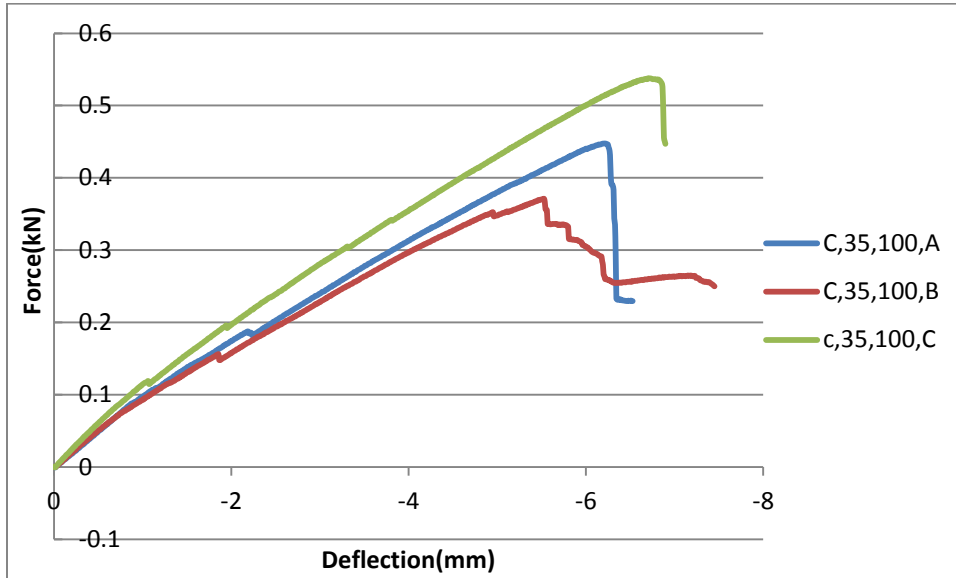
Coated	25, 240
Normalized Modulus ($\frac{E}{E_0}$)	0.294688
Model Modulus Ratio ($\frac{E_m}{E_0}$)	0.204336
Overall Stiffness (MPa) (E_m)	4756.948
Resin Stiffness (MPa) (E_{resin})	681.6141
Glass Stiffness (MPa) (E_{glass})	20139.59
Resin Ultimate Strength (MPa) (S_{ut})	4.460164
Glass Yield Strength (MPa) ($S_{y,glass}$)	228.5346
Rupture Strain (ϵ_{ut})	0.006544

Appendix C.22: Coated, $\phi=35$, $t_{exp}=60$



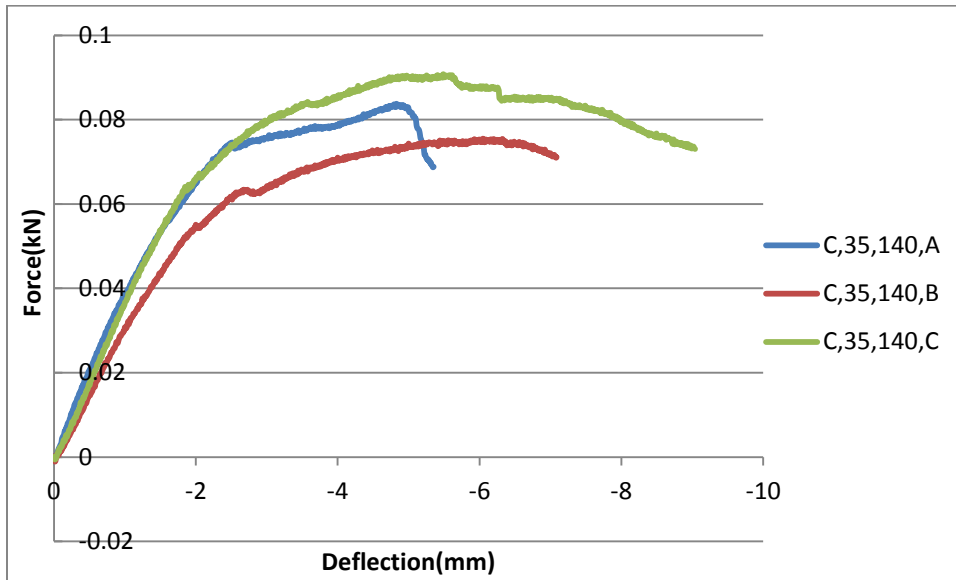
Coated	35, 60
Normalized Modulus ($\frac{E}{E_0}$)	0.459021
Model Modulus Ratio ($\frac{E_m}{E_0}$)	0.880941
Overall Stiffness (MPa) (E_m)	20508.31
Resin Stiffness (MPa) (E_{resin})	1061.715
Glass Stiffness (MPa) (E_{glass})	31370.38
Resin Ultimate Strength (MPa) (S_{ut})	10.82154
Glass Yield Strength (MPa) ($S_{y,glass}$)	355.9763
Rupture Strain (ϵ_{ut})	0.010193

Appendix C.23: Coated, $\phi=35$, $t_{exp}=100$



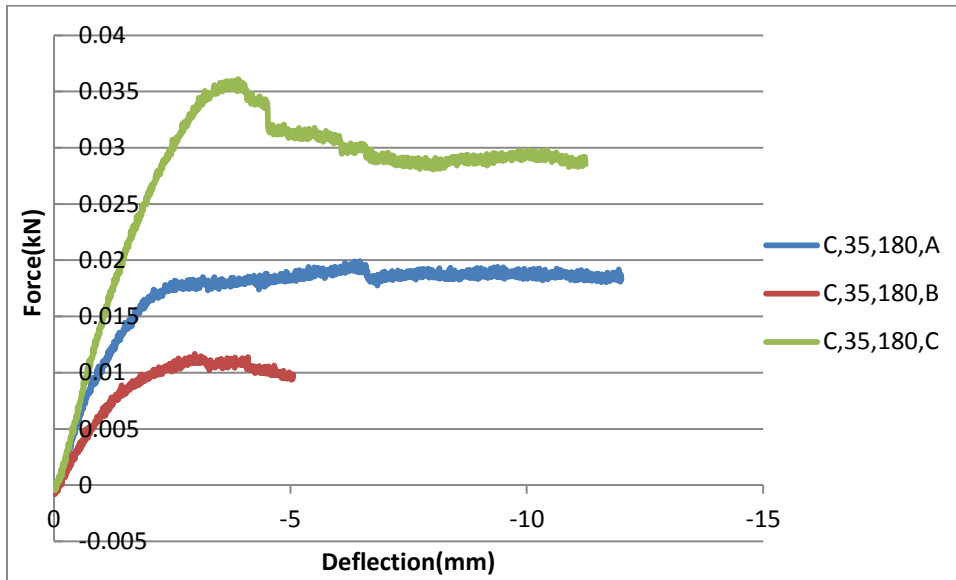
Coated	35, 100
Normalized Modulus ($\frac{E}{E_0}$)	0.463059
Model Modulus Ratio ($\frac{E_m}{E_0}$)	0.890469
Overall Stiffness (MPa) (E_m)	20730.11
Resin Stiffness (MPa) (E_{resin})	2313
Glass Stiffness (MPa) (E_{glass})	68342
Resin Ultimate Strength (MPa) (S_{ut})	23.78272
Glass Yield Strength (MPa) ($S_{y,glass}$)	775.5129
Rupture Strain (ϵ_{ut})	0.010282

Appendix C.24: Coated, $\phi=35$, $t_{exp}=140$



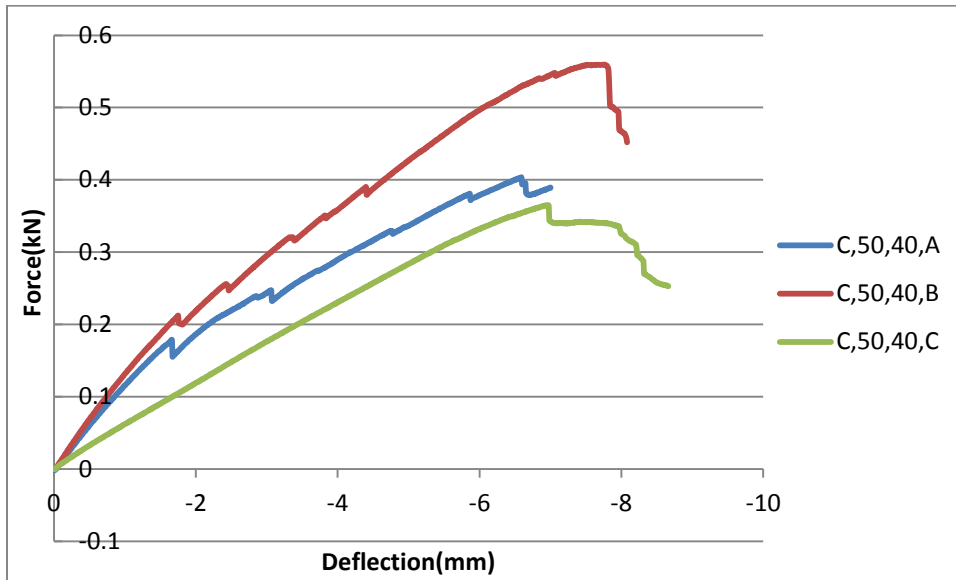
Coated	35, 140
Normalized Modulus ($\frac{E}{E_0}$)	0.311912
Model Modulus Ratio ($\frac{E_m}{E_0}$)	0.285428
Overall Stiffness (MPa) (E_m)	6644.767
Resin Stiffness (MPa) (E_{resin})	2313
Glass Stiffness (MPa) (E_{glass})	68342
Resin Ultimate Strength (MPa) (S_{ut})	16.0198
Glass Yield Strength (MPa) ($S_{y,glass}$)	775.5129
Rupture Strain (ϵ_{ut})	0.006926

Appendix C.25: Coated, $\phi=35$, $t_{exp}=180$



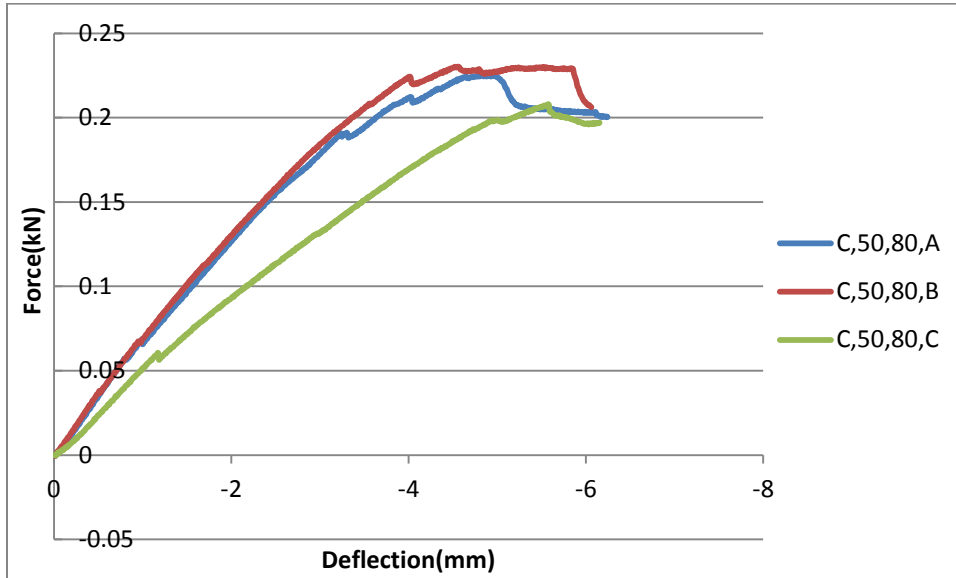
Coated	35, 180
Normalized Modulus ($\frac{E}{E_0}$)	0.089173
Model Modulus Ratio ($\frac{E_m}{E_0}$)	0.085114
Overall Stiffness (MPa) (E_m)	1981.454
Resin Stiffness (MPa) (E_{resin})	2313
Glass Stiffness (MPa) (E_{glass})	68342
Resin Ultimate Strength (MPa) (S_{ut})	4.579921
Glass Yield Strength (MPa) ($S_{y,glass}$)	775.5129
Rupture Strain (ϵ_{ut})	0.00198

Appendix C.26: Coated, $\phi=50$, $t_{exp}=40$



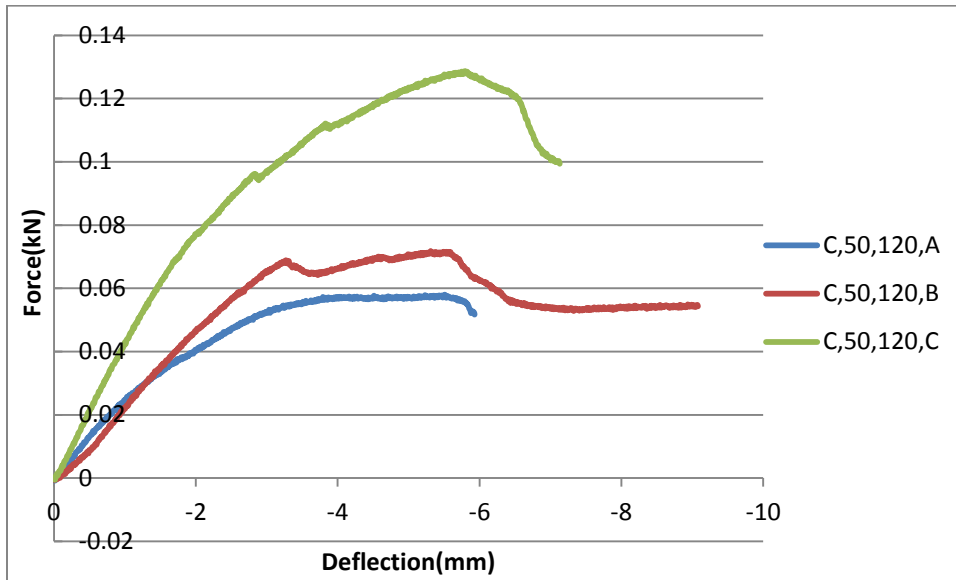
Coated	50, 40
Normalized Modulus ($\frac{E}{E_0}$)	0.484325
Model Modulus Ratio ($\frac{E_m}{E_0}$)	0.72007
Overall Stiffness (MPa) (E_m)	16763.22
Resin Stiffness (MPa) (E_{resin})	2313
Glass Stiffness (MPa) (E_{glass})	68342
Resin Ultimate Strength (MPa) (S_{ut})	24.87491
Glass Yield Strength (MPa) ($S_{y,glass}$)	775.5129
Rupture Strain (ϵ_{ut})	0.010754

Appendix C.27: Coated, $\phi=50$, $t_{exp}=80$



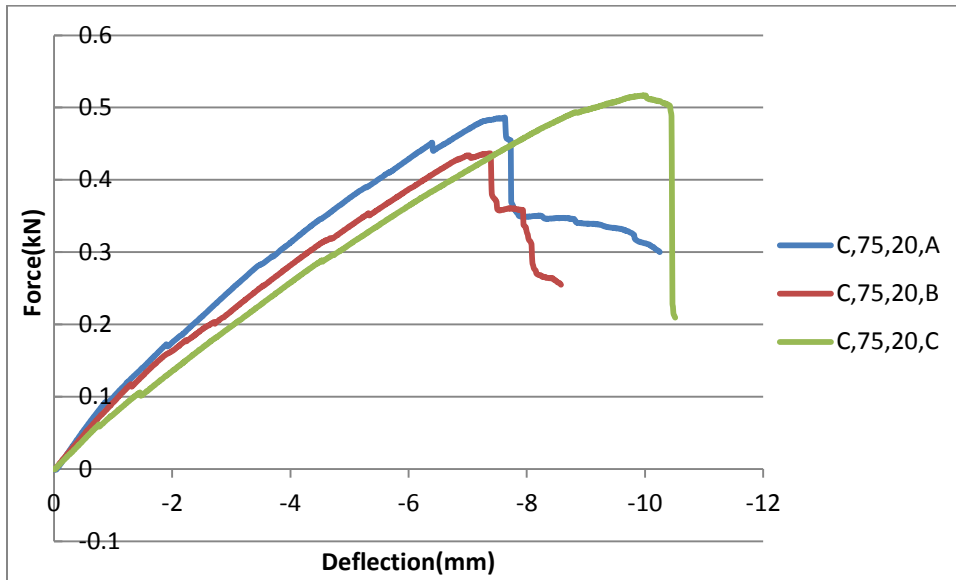
Coated	50, 80
Normalized Modulus ($\frac{E}{E_0}$)	0.270196
Model Modulus Ratio ($\frac{E_m}{E_0}$)	0.520005
Overall Stiffness (MPa) (E_m)	12105.72
Resin Stiffness (MPa) (E_{resin})	2313
Glass Stiffness (MPa) (E_{glass})	68342
Resin Ultimate Strength (MPa) (S_{ut})	13.87727
Glass Yield Strength (MPa) ($S_{y,glass}$)	775.5129
Rupture Strain (ϵ_{ut})	0.006

Appendix C.28: Coated, $\phi=50$, $t_{exp}=120$



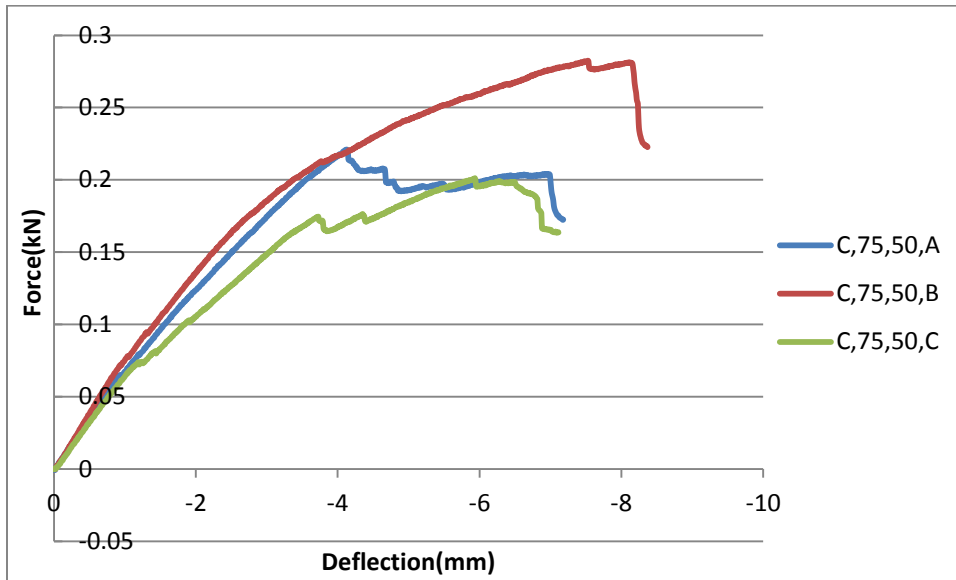
Coated	50, 120
Normalized Modulus ($\frac{E}{E_0}$)	0.23627
Model Modulus Ratio ($\frac{E_m}{E_0}$)	0.245883
Overall Stiffness (MPa) (E_m)	5724.153
Resin Stiffness (MPa) (E_{resin})	2313
Glass Stiffness (MPa) (E_{glass})	68342
Resin Ultimate Strength (MPa) (S_{ut})	12.13484
Glass Yield Strength (MPa) ($S_{y,glass}$)	775.5129
Rupture Strain (ϵ_{ut})	0.005246

Appendix C.29: Coated, $\phi=75$, $t_{exp}=20$



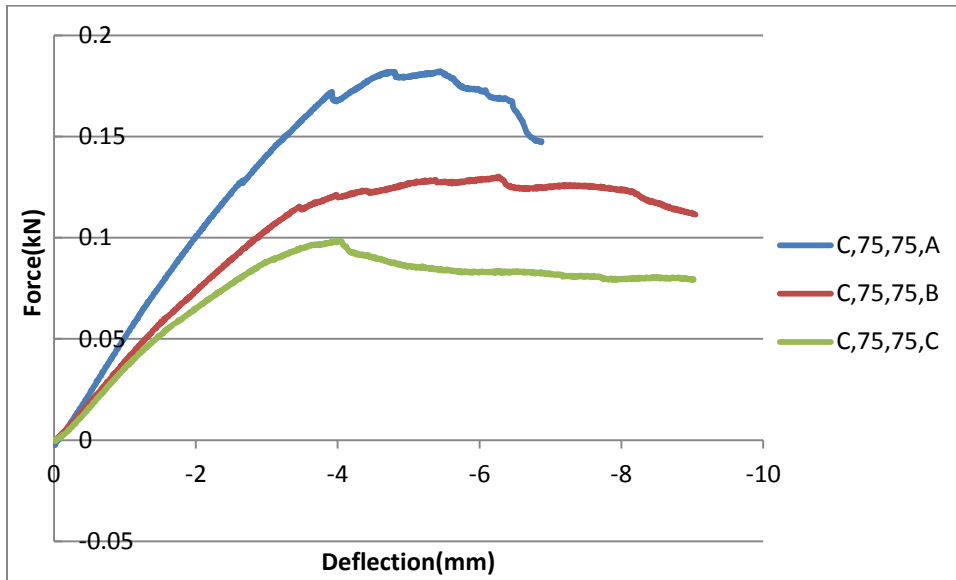
Coated	75, 20
Normalized Modulus ($\frac{E}{E_0}$)	0.489286
Model Modulus Ratio ($\frac{E_m}{E_0}$)	0.792652
Overall Stiffness (MPa) (E_m)	18452.94
Resin Stiffness (MPa) (E_{resin})	2313
Glass Stiffness (MPa) (E_{glass})	68342
Resin Ultimate Strength (MPa) (S_{ut})	25.12973
Glass Yield Strength (MPa) ($S_{y,glass}$)	775.5129
Rupture Strain (ϵ_{ut})	0.010865

Appendix C.30: Coated, $\phi=75$, $t_{exp}=50$



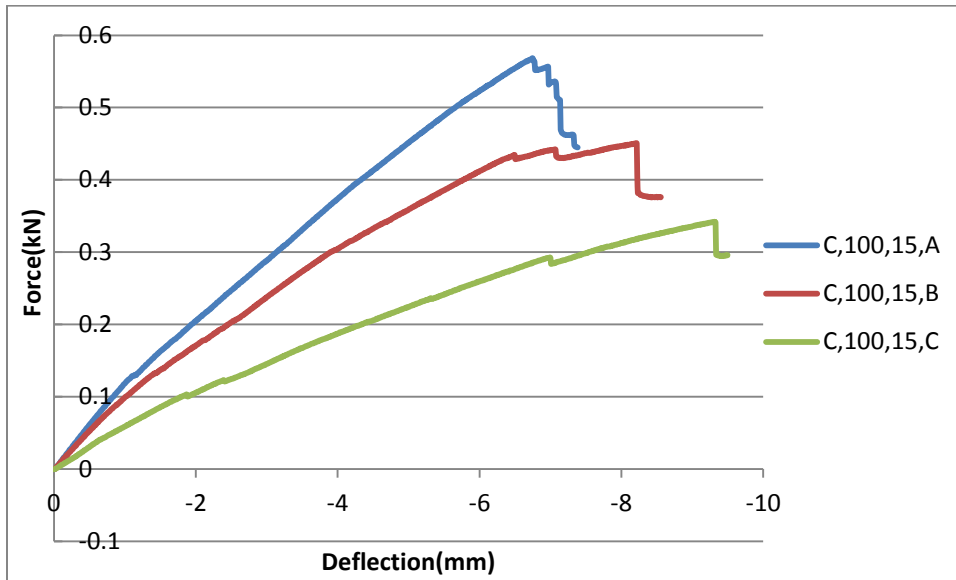
Coated	75, 50
Normalized Modulus ($\frac{E}{E_0}$)	0.287287
Model Modulus Ratio ($\frac{E_m}{E_0}$)	0.474981
Overall Stiffness (MPa) (E_m)	11057.57
Resin Stiffness (MPa) (E_{resin})	2313
Glass Stiffness (MPa) (E_{glass})	68342
Resin Ultimate Strength (MPa) (S_{ut})	14.75504
Glass Yield Strength (MPa) ($S_{y,glass}$)	775.5129
Rupture Strain (ϵ_{ut})	0.006379

Appendix C.31: Coated, $\phi=75$, $t_{exp}=75$



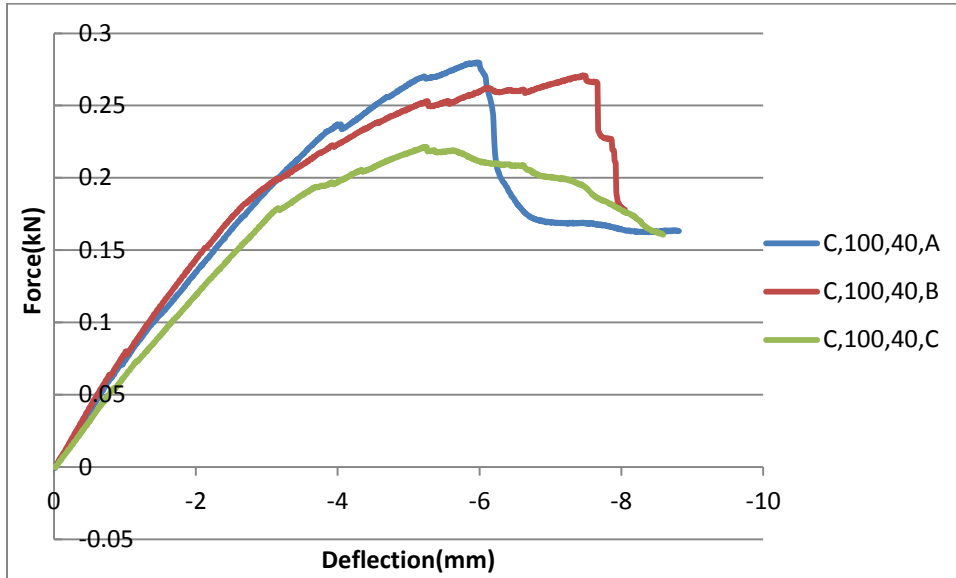
Coated	75, 75
Normalized Modulus ($\frac{E}{E_0}$)	0.321177
Model Modulus Ratio ($\frac{E_m}{E_0}$)	0.30903
Overall Stiffness (MPa) (E_m)	7194.23
Resin Stiffness (MPa) (E_{resin})	2313
Glass Stiffness (MPa) (E_{glass})	68342
Resin Ultimate Strength (MPa) (S_{ut})	16.49567
Glass Yield Strength (MPa) ($S_{y,glass}$)	775.5129
Rupture Strain (ϵ_{ut})	0.007132

Appendix C.32: Coated, $\phi=100$, $t_{exp}=15$



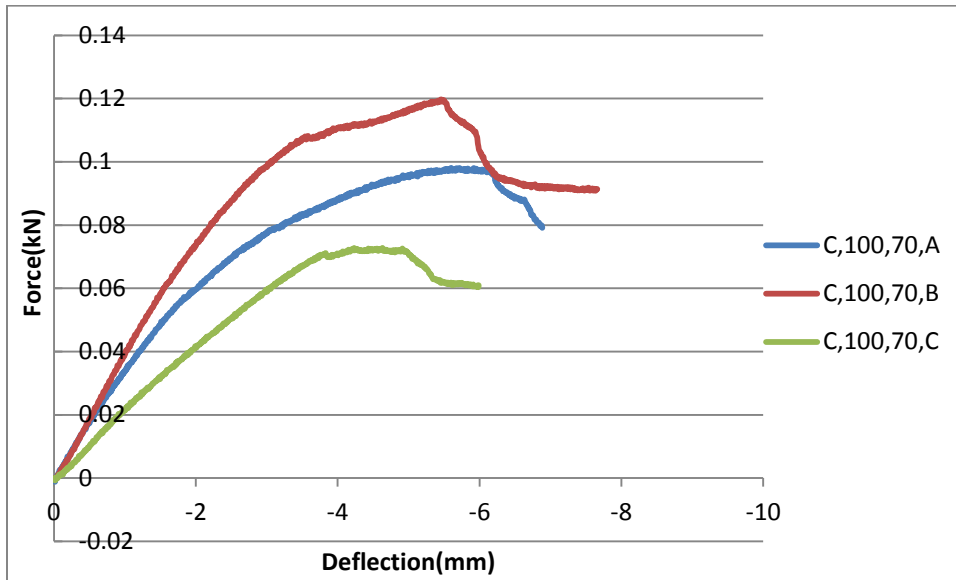
Coated	100, 15
Normalized Modulus ($\frac{E}{E_0}$)	0.369802
Model Modulus Ratio ($\frac{E_m}{E_0}$)	0.693466
Overall Stiffness (MPa) (E_m)	16143.88
Resin Stiffness (MPa) (E_{resin})	2313
Glass Stiffness (MPa) (E_{glass})	68342
Resin Ultimate Strength (MPa) (S_{ut})	18.99302
Glass Yield Strength (MPa) ($S_{y,glass}$)	775.5129
Rupture Strain (ϵ_{ut})	0.008211

Appendix C.33: Coated, $\phi=100$, $t_{exp}=40$



Coated	100, 40
Normalized Modulus ($\frac{E}{E_0}$)	0.294468
Model Modulus Ratio ($\frac{E_m}{E_0}$)	0.542444
Overall Stiffness (MPa) (E_m)	12628.09
Resin Stiffness (MPa) (E_{resin})	2313
Glass Stiffness (MPa) (E_{glass})	68342
Resin Ultimate Strength (MPa) (S_{ut})	15.12385
Glass Yield Strength (MPa) ($S_{y,glass}$)	775.5129
Rupture Strain (ϵ_{ut})	0.006539

Appendix C.34: Coated, $\phi=100$, $t_{exp}=70$



Coated	100, 70
Normalized Modulus ($\frac{E}{E_0}$)	0.247129
Model Modulus Ratio ($\frac{E_m}{E_0}$)	0.250295
Overall Stiffness (MPa) (E_m)	5826.867
Resin Stiffness (MPa) (E_{resin})	2313
Glass Stiffness (MPa) (E_{glass})	68342
Resin Ultimate Strength (MPa) (S_{ut})	12.69254
Glass Yield Strength (MPa) ($S_{y,glass}$)	775.5129
Rupture Strain (ϵ_{ut})	0.005487

References

- ASTM Standard D790, "Standard Test Methods for Flexural Properties of Unreinforced and Reinforced Plastics and Electrical Insulating Materials," *ASTM International*, West Conshohocken, PA, 2010.
- Bai, Y., Keller, T., Vallee, T., "Modeling of stiffness of FRP composites under elevated and high temperatures." *Composites Science and Technology*. Vol. 68, pp. 3099-3106, 2008.
- Cavallero, P. V., Sadegh, A. M., and Quigley, C. J., 2007, "Decrimping Behavior of Uncoated Plain-Woven Fabrics Subjected to Combined Biaxial Tension and Shear Stress," *Textile Research Journal*, **77**(6) pp. 403-416.
- Davallo, M., Pasdar, H., Mohseni, M., "Mechanical Properties of Unsaturated Polyester Resin", *International Journal of ChemTech Research*, **2**(4), pp.2113-2117
- Ferreira J. M. , Errajhi O. A. Z. , Richardson M. O. W. . "Thermogravimetric analysis of aluminized E-glass fiber reinforced unsaturated polyester composites. *Polymer Testing*. 2006; 25(8):1091-1094.
- Guan, H., and Gibson, R. F., 1997, "Micromechanical Models for Damping in Woven Fabric-Reinforced Polymer Matrix Composites," *Journal of Composite Materials*, **35**(16) pp. 1417-1434.
- Hale, J., 2006, "Boeing 787 from the Ground Up," *AERO*, **Q4** pp. 17-24 < http://www.boeing.com/commercial/aeromagazine/articles/qtr_4_06/article_04_2.html>
- Kandare, E., Kandola, B.K., Myler, P., Horrocks, A.R., Edwards, G., "Thermo-mechanical responses of fibre-reinforced epoxy composites exposed to high temperature environment: I." *Journal of Composite Structures*. Vol. 26, pp. 3093-3114, 2010.

- Kollegal, M. G., and Sridharan, S., 2000, "A Simplified Model for Plain Woven Fabrics," *Journal of Composite Materials*, **34**(20) pp. 1756-1786.
- Liu, H. L., Lin, C. L., and Sun, M. T., 2010, "3D Micro-Crack Propagation Simulation at Enamel/Adhesive Interface using FE Submodeling and Element Death Techniques," *Annals of Biomedical Engineering*, **38**(6) pp. 2004-2012.
- Looyeh, M. R. E., Bettess, P., and Gibson, A. G., 1996, "A One Dimensional Finite Element Simulation for the Fire Performance of GRP Panels for Offshore Structures," *International Journal of Numerical Methods for Heat & Fluid Flow*, **7**(6) pp. 609-625.
- Luo, C., and DesJardin, P. E., 2006, "Thermo-Mechanical Damage Modeling of a glass–phenolic Composite Material," *Composites Science and Technology*, **67**(1) pp. 1475-1488.
- Masmoudi, R., Metiche, S., and Mohamed, H., 2008, "Finite Element Modeling for Deflection and Bending Responses of GFRP Poles," *Journal of Reinforced Plastics and Composites*, **27**(6) pp. 639-658.
- Page, B. H., Guild, F. J., and Ogin, S. L., 2004, "Finite Element Simulation of Woven Fabric Composites," *Composites: Part A*, **35**(1) pp. 861-872.
- Shahkarami, A., and Vaziri, R., 2007, "A Continuum Shell Finite Element Model for Impact Simulation of Woven Fabrics," *International Journal of Impact Engineering*, **34**(1) pp. 104-119.
- Skovron, J., Zhuge, J., Gou, J., and Gordon, A.P. 2013, "Effect of Nano-Paper Coating on Flexural Properties of a Fire-Treated Glass-Fiber Reinforced Polyester Composite," *Journal of Engineering Materials and Technology*
- Takeda, T., Shindo, Y., and Narita, F., 2002, "Thermoelastic Analysis of Cracked Woven GFRP Laminates at Cryogenic Temperatures," *Cryogenics*, **42**(1) pp. 451-462.
- Tarfaoui, M., Drean, J. Y., and Akesbi, S., 2001, "Predicting the Stress-Strain Behavior of Woven Fabrics using the Finite Element Method," *Textile Research Journal*, **71**(9) pp. 790-795.

Xu, D., Ganesan, R., and Hoa, S. V., 2005, "Buckling Analysis of Tri-Axial Woven Fabric Composite Structures. Part I: Non-Linear Finite Element Formulation," *Composite Structures*, **67**(1) pp. 37-55.

Yong Tang, Jinfeng Zhuge, Jeremy Lawrence, James Mckee, Jihua Gou, Christopher Ibeh and Yuan Hu. "Flame retardancy of carbon nanofiber/intumescent hybrid paper based fiber reinforced polymer composites." *Polymer Degradation and Stability*. 2011. 5. 760-770.

Zhuge, J., 2012, "Fire retardant evaluation of carbon nanofiber/graphite nanoplatelets nanopaper-based coating under different heat fluxes." *Composites: Part B*, 43: 3293-3305